DISSERTATIONES
CHIMICAE
UNIVERSITATIS
TARTUENSIS
188

RONALD VÄLI

Glucose-derived hard carbon electrode materials for sodium-ion batteries

DISSERTATIONES CHIMICAE UNIVERSITATIS TARTUENSIS
188

DISSERTATIONES CHIMICAE UNIVERSITATIS TARTUENSIS

188

RONALD VÄLI

Glucose-derived hard carbon electrode materials for sodium-ion batteries

UNIVERSITY OF TARTU
Press

Institute of Chemistry, Faculty of Science and Technology, University of Tartu, Estonia

Dissertation is accepted for the commencement of the degree of Doctor of Philosophy in Chemistry on June 20th, 2019 by the Council of the Institute of Chemistry, University of Tartu.

Supervisors: Prof. Enn Lust, University of Tartu, Estonia
Ph.D. Alar Jänes, University of Tartu, Estonia

Opponent: Prof. Patrik Johansson, Chalmers University of Technology, Sweden

Commencement: August 29th, 2019 at 14:15
14a Ravila Street (Chemicum), auditorium 1020

European Union
European Regional
Development Fund

Investing
in your future

ISSN 1406-0299
ISBN 978-9949-03-110-8 (print)
ISBN 978-9949-03-111-5 (pdf)

University of Tartu Press
www.tyk.ee

TABLE OF CONTENTS

1. LIST OF ORIGINAL PUBLICATIONS

This thesis consists of five original articles listed below. The articles are referred in the text using Roman numerals I−V.

I **R. Väli**, A. Jänes, T. Thomberg, E. Lust, D-Glucose Derived Nanospheric Hard Carbon Electrodes for Room-Temperature Sodium-Ion Batteries, J. Electrochem. Soc. 163 (2016) A1619–A1626.

II **R. Väli**, A. Jänes, E. Lust, Alkali-Metal Insertion Processes on Nanospheric Hard Carbon Electrodes: An Electrochemical Impedance Spectroscopy Study, J. Electrochem. Soc. 164 (2017) E3429–E3437.

III **R. Väli**, A. Jänes, T. Thomberg, E. Lust, Synthesis and characterization of D-glucose derived nanospheric hard carbon negative electrodes for lithium- and sodium-ion batteries, Electrochim. Acta 253 (2017) 536–544.

IV J. K. Mathiesen, **R. Väli**, M. Härmas, E. Lust, J. F. von Bülow, K. M. Ø. Jensen, P. Norby, Following the In-plane Disorder of Sodiated Hard Carbon through Operando Total Scattering, J. Mater. Chem. A 7 (2019) 11709–11717.

V **R. Väli**, J. Aruväli, M. Härmas, A. Jänes, E. Lust, Glycine-nitrate process for synthesis of Na3V2(PO4)3 cathode material and optimization of glucose-derived hard carbon anode material for characterization in full cells, Batteries (2019) under review.

Author's contribution

Paper I: Performed all electrochemical measurements and analysis of data. Mainly responsible for the preparation of the manuscript.

Paper II: Performed all electrochemical measurements and analysis of data. Mainly responsible for the preparation of the manuscript. Proposed the research topic.

Paper III: Performed all electrochemical measurements and analysis of data. Mainly responsible for the preparation of the manuscript.

Paper IV: Provided physical characterization data. Collaborated in experimental data interpretation and manuscript preparation.

Paper: V: Performed synthesis of electrode materials. Performed all electrochemical measurements and analysis of data. Main person responsible for manuscript preparation.

2. ABBREVIATIONS AND SYMBOLS

A	constant phase element coefficient
a	in-plane cell parameter (x-axis)
ac	alternating current
ADP	atomic displacement parameter
av	alternating voltage
b	in-plane cell parameter (y-axis)
BET	Brunauer-Emmett-Teller
c	lattice constant
C	capacitance
CA	citric acid
C_{dl}	double layer capacitance
CE	coulombic efficiency
CPE	constant phase element
C_{SEI}	solid electrolyte interphase capacitance
CV	cyclic voltammetry
D	diffusion coefficient
DEC	diethyl carbonate
DFT	density functional theory
DMC	dimethyl carbonate
E	working electrode potential
EC	ethylene carbonate
EDLC	electrical double layer capacitor
E_{g}	specific energy
EIS	electrochemical impedance spectroscopy
ESI	electronic supplementary information
EQC	equivalent circuit
f	ac frequency in Hz
FEC	fluoroethylene carbonate
FWHM	full width at half maximum
G	glycine
$G(r)$	pair distribution function for r
GCD	galvanostatic charge-discharge
GDHC	glucose-derived hard carbon
GIC	graphite intercalation compound
HC	hard carbon
HRTEM	high-resolution transmission electron microscopy
HT	heat treatment
HTC	hydrothermal carbonization
I	current
I_{D}	intensity of D-peak in a Raman spectrum
I_{G}	intensity of G-peak in a Raman spectrum
I_{g}	specific current

j	imaginary unit ($\sqrt{-1}$)
KIB	potassium-ion battery
L	effective diffusion length
LA-ICP-MS	laser ablation inductively coupled plasma mass spectrometry
LIB	lithium-ion battery
Me	alkali metal (Li, Na or K)
m_{active}	active material mass in the electrode
n	number of datapoints
NASICON	NAtrium Super Ionic CONductor
NIB	sodium-ion battery
Ni-MH	nickel-metal hydride battery
NLDFT	non-linear density functional theory
NMP	N-Methyl-2-pyrrolidone
NMR	nuclear magnetic resonance
NVP	$Na_3V_2(PO_4)_3$
NVPF	$Na_3V_2(PO_4)_2F_3$
OCP	open-circuit potential
PC	propylene carbonate
PDF	pair distribution function
PVDF	polyvinylidene difluoride
PXRD	powder X-ray diffraction
r	distance between two atoms in the PDF
R_{ct}	charge transfer resistance
R_{D}	diffusion resistance
R_{s}	series resistance
R_{SEI}	solid electrolyte interphase resistance
S	geometric surface area of the electrode
SAXS	small-angle X-ray scattering
S_{BET}	specific surface area calculated using BET theory
S_{DFT}	specific surface area calculated using density functional theory
SEI	solid electrolyte interphase
SEM	scanning electron microscope
SHE	standard hydrogen electrode
SOC	state-of-charge
Q	specific capacity
Q_{D}	specific discharge capacity
Q_{N}	negative electrode capacity
Q_{P}	positive electrode capacity
T	temperature
T_{b}	boiling point
T_{m}	melting point
t	time
TOF-SIMS	time-of-flight secondary ion mass spectrometry
V	cell potential
V_{DFT}	total pore volume calculated using DFT

V_{tot}	total pore volume
wt%	weight percent
XRD	X-ray diffraction
Z	complex impedance
Z'	real part of impedance
Z''	imaginary part of impedance
ZEBRA	Zero-Emission Battery Research Activities or ZEolite Battery Research Africa
Z_{Ws}	finite-length Warburg impedance
α_{CPE}	CPE fractional exponent
α_{W}	Warburg fractional exponent
Δ^2	weighted sum of the squares
ε	dielectric permittivity
η	viscosity
v	potential scan rate
μ	dipole moment
τ_{Ws}	Warburg diffusion time constant
χ^2	chi-square function
ω	angular frequency

3. INTRODUCTION

Batteries are one of the key technologies of the 21st century. The growth of portable electronics market (smartphones, smartwatches, tablets, laptops etc.) and electromobility such as electric vehicles and drones increases the demand for cheaper and more energy dense batteries. All the mentioned technologies rely on the application of the most advanced batteries currently available – lithium-ion batteries (LIBs). However, with the concerns of adequate supply of fossil fuel resources and the impact their use has on the environment, renewable energy sources such as solar and wind energy have made a massive increase in their adaptation in the last decades [1,2]. Unfortunately, these power sources are intermittent and therefore require storage solutions to smooth out fluctuations in both supply and demand [3]. Such applications require huge batteries, but the use of high-energy density LIBs would be impractical in such stationary devices, where the size and weight are not as crucial as in portable and automotive applications. Furthermore, the increased lithium and cobalt demand and their potential supply risks [4] limit the attractiveness of LIBs for stationary storage devices. Even if the battery recycling industry rapidly develops in the coming decades, it is still possible that recycling could not prevent the depletion of these key resources in time [5]. Therefore, cheaper alternatives have to be developed to meet the demand for stationary batteries.

Sodium-ion batteries (NIBs) have become the potential candidates for such applications. Na is very similar to lithium, which makes it easier to adopt the collective experience accumulated in the last 4 decades of LIB research.

Hard carbon is one of the most promising negative electrode materials for commercial NIBs, but despite increasing interest in that material, its Na storage mechanism and structure−electrochemistry relationships are still debated [6]. The protective solid electrolyte interphase that forms on the negative electrode surface upon reductive decomposition of the electrolyte is not as stable as in commercial LIBs, which hinders the cycle life of NIBs [7,8]. Glucose was chosen as the precursor material in this work since glucose is an environmentally friendly material and unlike other biomass, is very pure, i.e. no mineral content. Therefore, glucose-derived carbon serves as an excellent material to study Na insertion processes.

The main aims of this thesis are to:

a) Compare the nature of electrode processes on the hard carbon surface using different alkali metal ions by employing electrochemical impedance spectroscopy (EIS) and other electrochemical methods [II,III];
b) Study decomposition products on the electrode surface using *ex situ* methods [I,III];
c) Understand, which structural changes to the carbon material take place during electrochemical cycling [IV];
d) Establish how the electrolyte affects cell performance [II,III].

e) Synthesize a positive electrode material (NVP) using an industrially scalable method, optimize the negative electrode material and test a full cell assembled from GDHC and NVP [V].

In this thesis, the synthesis of glucose-derived hard carbon (GDHC) via hydrothermal carbonization (HTC) is described. Na storage mechanism into/onto hard carbon is studied using *ex situ* LA-ICP-MS [I] and TOF-SIMS [III] combined with galvanostatic charge-discharge (GCD) method. Differences in electrochemical behavior of Li, Na and K are evaluated using electrochemical impedance spectroscopy (EIS) and equivalent circuit fitting of spectra recorded in a wide potential range for both charge and discharge processes [II]. Changes to the hard carbon structure during electrochemical cycling are evaluated using *operando* total X-ray scattering [IV]. Finally, the synthesis of $Na_3V_2(PO_4)_3$ positive electrode material via glycine-nitrate process (GNP) is described and analyzed and the performance of a GDHC||NVP full cell is demonstrated [V].

4. LITERATURE OVERVIEW

4.1 Batteries

Batteries are electrochemical energy storage devices in which electrical energy is stored in chemical bonds of electroactive compounds. They generally fall into two categories – primary batteries which can only release energy once, i.e. the redox reactions in the battery are irreversible, and secondary or rechargeable batteries, which can be charged hundreds or thousands of times, i.e. the redox reactions are reversible.

The history of batteries dates back to 1745, when the first capacitor – the Leyden jar was invented. The Leyden jar could store static electricity, but its capacity was very limited [9]. In 1749 Benjamin Franklin coined the term battery to describe set of connected Leyden jars to increase capacity. The term originated from the military, where a unit of artillery pieces was called a battery [10]. The first electrochemical battery was invented in 1799 by Alessandro Volta, called the Voltaic pile [11]. It consisted of alternating copper and zinc plates connected in series with salt-soaked blotting paper in between. The Voltaic pile made it possible for other scientists to experiment with electric currents under reasonably controlled conditions, which laid the foundation for the development of numerous fields of science such as electricity, magnetism and electrochemistry. Humphry Davy was able to isolate several elements such as sodium (the topic of this dissertation), magnesium and calcium via electrolysis [12], Nicholson and Carlisle were able to liberate oxygen and hydrogen from water using electrolysis [13].

The first rechargeable battery, the lead acid battery, was invented in 1859 by Gaston Planté [14] and its core technology is still used to this date and likely in the coming decades as well. It is very simple and robust, it consists of a lead plate and a lead plate covered with lead oxide and sulfuric acid as the electrolyte. Advances in cell design and increases in the variety of materials followed. In 1866, Leclanché designed the first zinc-carbon primary cell that used a zinc anode and a MnO_2 (a common battery electrode material today) cathode mixed with carbon [15]. The Leclanché cell was further improved by Karl Gassner (1886), who invented the first dry cell, in which a folded paper sack served as the separator and was soaked with a $ZnCl_2$ solution, hence the name [16]. This technical improvement made batteries much more mobile as the risk of electrolyte spill was reduced.

Looking for an alternative rechargeable battery solution in which the electrolyte concentration does not chemically change during battery operation, as it does in lead-acid batteries, Waldemar Jungner invented both Ni-Fe and Ni-Cd batteries in 1899 that used KOH as the electrolyte [16]. Ni-Cd batteries had better high-rate and low-temperature performance than lead-acid batteries [3] and is still used today. The main problem with cadmium is its toxicity and memory effects that occur during partial discharging. Those problems were solved by Stanford Ovshinsky in 1984 with the invention of nickel metal hydride (Ni-MH) battery [17] in which the metal hydride served as a reversible storage medium for hydrogen [3]. The Ni-MH specific energy is 1.5 to 2.0 times higher than that of Ni-Cd and it was the dominant battery technology in portable devices until the commercialization of a radically different technology that utilized the lightest and smallest metal available – lithium, which eventually led to the introduction of the Li-ion battery (LIB) in 1991 by Sony [18].

4.1.1 Lithium batteries

Researchers at Exxon Laboratories showed in the early 1970s that Li-ions can be reversibly inserted (intercalated) into and extracted (de-intercalated) from layered inorganic compounds such as TiS_2. This mechanism caused no significant change to the crystal lattice which enabled high current rates and spawned research into materials like V_6O_{13}, MoS_2, MoS_3 and $NbSe_3$. The first rechargeable lithium battery was commercialized by Moli Energy Corporation in Canada. It used Li metal foil as the negatively charged electrode and a lithium salt dissolved in a polar organic liquid. The cell's nominal voltage was 1.8 V, higher than in any other previous aqueous battery cell. Ultimately, the battery had to be withdrawn from the market as safety issues became a major concern [3]. Lithium batteries with Li metal electrode are thermodynamically unstable because the lithium plating and stripping reactions on the negative electrode occur at potentials (0 V vs Li/Li^+) far below the electrochemical stability window (>1 V vs Li/Li^+) of the electrolytes [19]. In addition, Li plating on the metal surface is not uniform – dendrites form and can short the cell [3]. That is why there are no rechargeable lithium batteries with Li metal electrode available on the market today. The origin of lithium-ion batteries dates back to 1970s when a group at Oxford University led by John Goodenough discovered that lithium ions can be reversibly intercalated into the crystal lattice of trivalent cobalt or nickel oxides to yield $LiCoO_2$ and $LiNiO_2$. Coupled with Li metal negative electrode the cells reached 4 V [3]. However, Li metal negative electrode still posed a major problem.

4.1.1.1 Lithium-ion batteries

The negative electrode problem was solved after 1982, when Yazami and Touzain published their work in which Li was intercalated into graphite using a solid electrolyte of polyethylene oxide and $LiClO_4$ [20]. Basu and Somerset from the Bell Labs soon filed for a patent that described the operation of a battery that operated at ambient temperatures and consisted of two intercalation electrodes one of which was graphite and an organic electrolyte [21]. Other carbons such as cokes and hard carbons were studied in the following years, but the best results were achieved using graphite, which could take up one Li^+ per 6 carbon atoms. Graphite intercalation potential is slightly higher (about 100 mV) than Li plating potential, which reduces the cell's energy density, but also increases its safety. Still, reductive decomposition of the electrolyte takes place on graphite surface. Fortunately, these decomposition products form an electrically insulating, but Li-ion conducting film on the surface, which stabilizes the battery and enables long cycle life [22].

There are various reasons for using carbons as battery electrode materials: carbon is abundant, non-toxic, a good conductor, can form a wide variety of structures and is electrochemically stable in a wide potential range [23].

4.1.2 Sodium-ion batteries (NIBs)

Sodium battery research dates back to 1967 when discoveries of a high-temperature solid-state sodium ion conductor – sodium β″-alumina ($NaAl_{11}O_{17}$) were reported [24,25]. That spawned research into the field of high temperature (300 ºC) batteries in which the electrodes are in a molten state. Two commercially available batteries were developed: the sodium sulfur (Na-S) battery, which used molten sodium and molten sulfur as electrodes; and the ZEBRA (Zero-Emission Battery Research Activities or ZEolite Battery Research Africa [26]), which used molten sodium and molten $NiCl_2$ as electrodes [5]. Ambient temperature sodium batteries were studied alongside lithium batteries in the 1970s and 1980s, but the benefits that lithium provided – higher energy density thanks to higher potential and lower mass (see **Table I**), shifted the research efforts of the battery community to lithium based systems [5]. Sodium-ion battery research took off after 2010 and has been growing since [27].

Table I. Comparison of properties of Li and Na [28–30].

	Li	**Na**
Ionic radius	68 pm	97 pm
Atomic mass	6.9 g mol^{-1}	23 g mol^{-1}
E^0 vs SHE	−3.04 V	−2.7 V
Melting point	180.5 °C	97.7 °C
Abundance in Earth's crust	20 mg kg^{-1}	23 600 mg kg^{-1}
Geographic distribution	70% in South-America	Uniform
Raw material price (carbonate)	4000 $/ton	120 $/ton
Theoretical capacity (metal-air electrode)	3861 mAh g^{-1} 2062 mAh cm^{-3}	1166 mAh g^{-1} 1131 mAh cm^{-3}

While a wide variety of positive electrode materials for NIBs already exist, some of which are being commercially manufactured, like $Na_aNi_{(1-x-y-z)}Mn_x Mg_yTi_zO_2$ by Faradion [31], many of the best candidates (the high voltage ones) still contain Co [27]. One type of polyanionic positive electrode materials that stand out are vanadium phosphates ($Na_3V_2(PO_4)_3$ and $Na_3V_2(PO_4)_2F_3$) that have a high potential vs Na/Na^+ and in which Na diffusion is fast enabling the construction of high-power battery cells. Such materials are called NASICONs (NAtrium Super Ionic CONductor) [32].

Unfortunately, sodium cannot reversibly intercalate into graphite [33,34], because Na intercalation stretches the C−C bond in graphite more than Li or even K intercalation. Therefore, the formed Na−graphite intercalation compound (Na-GIC) is unstable [35]. It has been shown that Na intercalation into graphite can be increased if utilizing solvent co-intercalation phenomenon using ether based solvents such as glymes [36,37]. Nevertheless, co-intercalation of solvent molecules causes graphene layer expansion and will ultimately lead to exfoliation as the solvent decomposes in graphite [23]. Alloying compounds such as Ge, Sb, Sn allow for high capacities (~700 mAh g^{-1}), which is almost twice as higher than graphite in LIBs (372 mAh g^{-1}) [38], but due to high volumetric expansion the active material is pulverized in the process and rapid capacity fade will follow [39]. Currently, the material with the highest commercialization potential for NIBs is hard carbon [6].

4.2 Hard carbon

Hard carbons are a type of carbons that are non-graphitizable by heat treatment (at 3000 ºC) and are mechanically hard, hence the name. Soft carbons on the other hand are mechanically soft and can be graphitized. Hard carbons are obtained by pyrolysis of resins, furfuryl alcohol, charcoal and various biomasses [40]. These carbons are usually formed by solid-state transformation during the carbonization steps and contain less hydrogen than soft carbons [41]. The difference in structure shown in **Figure 1** and processes during heat treatment shown in **Figure 2**. One explanation for the inability of hard carbons to form a graphitic structure by heat treatment is the presence of strong sp^3 crosslinking bonds, which impede movement and reorientation of the carbon atoms to form the ordered layer structure of graphite [40].

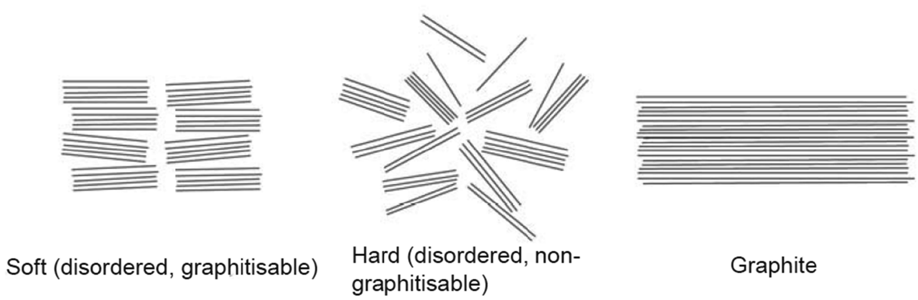

Figure 1. Graphic depictions of the structures of soft carbon, hard carbon and graphite [42].

Although hard carbon has been thoroughly researched and even used in 2nd generation LIBs by Sony [6], the fundamental understanding of the sodium storage mechanism, the ion transfer process, SEI formation and stability are still debated [29,43]. The search for a uniform storage model is complicated by the fact the hard carbons are disordered materials, which means that it is difficult to link physical characterization data (structural and morphological properties) to electrochemical behavior [6]. The intrinsic disorderedness of the material causes broad signals, which are difficult to interpret.

The carbonization process is complex and involves simultaneous reactions such as dehydrogenation, condensation, hydrogen transfer and isomerization (**Figure 2**). The macromolecular structure of the precursor persists and does not convert into a fluid phase upon heat treatment as in the case of graphitizable carbons [44]. Randomly positioned pseudographitic domains that are formed during the carbonization process create spaces and form bulk of the porosity in the material [45].

Gas sorption measurements using nitrogen (N_2) are usually employed to establish material surface area and porosity, but the models used for interpreting the data assume certain porous structure, which for hard carbons is relatively unknown [6]. Furthermore, different gas molecules show different adsorption behavior and some pores may be inaccessible to N_2, but “open” to helium (He) at room temperature or CO_2 at 0 ºC. Ionic species like Li^+ and Na^+ ions can diffuse through the solid phase of hard carbons and accumulate in such “closed” pores, as recently reported by Panasonic, where they showed a strong correlation between closed porosity and electrochemical performance of NIBs [46].

Numerous carbon sources have been used to produce hard carbons for NIBs: glucose [48], sucrose [49], cellulose [50], banana peels [51], peat moss [52], argan shells [53], polyethylene bags [54], phenolic resins [55] etc. The best results so far have been demonstrated by Kubota et al. who produced a hard carbon by heat treatment of activated carbon at 2100 ºC and achieved 420 mAh g^{-1} of which 390 mAh g^{-1} was at E < 0.1 V vs Na/Na^+ [56]. As this result exceeds the theoretical capacity of graphite [38], the charge storage mechanism cannot be explained by intercalation alone.

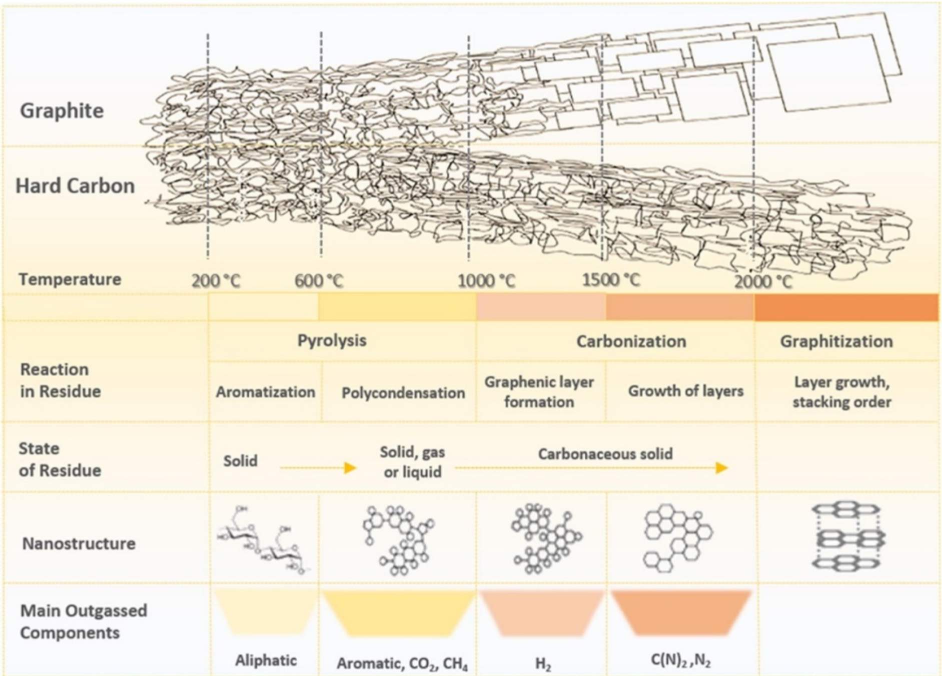

Figure 2. Graphite and hard carbon formation as a function of temperature [6,47].

4.2.1 Na storage mechanism in hard carbon

The first sodium storage mechanism into hard carbon proposed by Stevens and Dahn (**Figure 3a**) can be called intercalation−adsorption mechanism [57], in which Na ions first intercalate into pseudographitic layers producing a sloping galvanostatic profile (discussed in 4.5.2) and in the second step insert into the micropores formed by the pseudographitic domains and reduce to an oxidation state close to that of Na metal, resulting in a plateau at low potentials [48,57, 58]. Recent work by Stratford et al. showed that Na cluster formation into micropores is different from Na plating, as the Na^+ NMR peak in their *operando* experiment did shift considerably towards Na^0, but never reached it in the plateau region [59].

However, some experimental findings cast doubt to the beforementioned model. It has been observed that hard carbons obtained at T < 1000 ºC with a large micropore content do not display any low potential plateau capacity [51,52,60]. Pyrolysis temperature is inversely correlated with micropore volume and proportional to the degree of graphitization, so based on these observations [52,61], plateau capacity should decrease with increasing temperature, but it does not. Moreover, from electrochemical point of view, a monotonic slope represents a homogeneous electrochemical reaction with potential dependence, such as surface adsorption (like in supercapacitors) or a homogeneous insertion mechanism; while a potential plateau indicates a heterogeneous electrochemical reaction, corresponding to a two-phase transformation, such as lithium ion insertion into graphite or metal plating [62]. These observations support the adsorption−intercalation mechanism in **Figure 3b**.

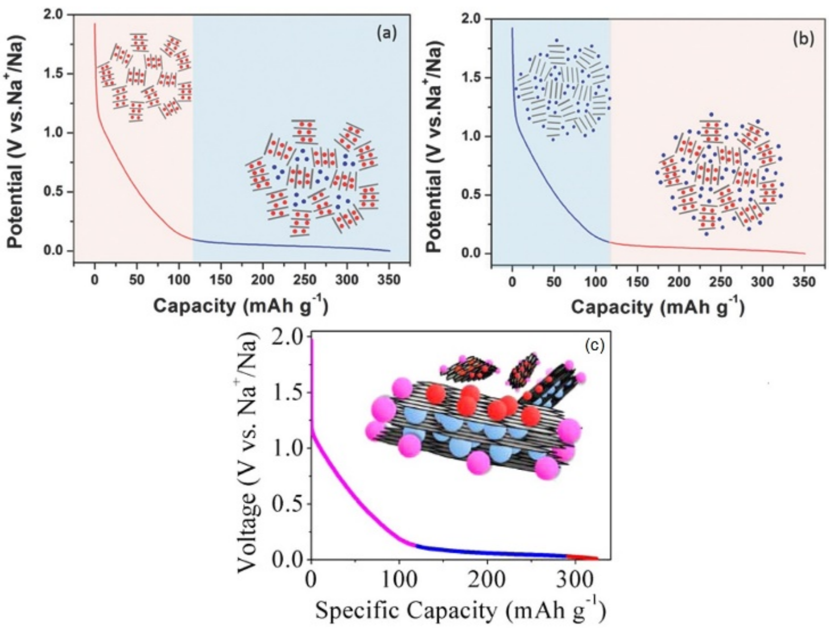

Figure 3. Schematic illustration of the mechanisms for Na^+ storage in hard carbon: a) "intercalation–adsorption" mechanism; b) "adsorption–intercalation" mechanism [62]; c) Three-stage mechanism proposed by Bommier et al. [61].

In defense of the intercalation-adsorption mechanism, Simone et al. proposed (**Figure 4**) that the increase in plateau capacity and decrease of sloping capacity at higher temperatures with increasing microporosity (determined from SAXS data) and decreasing interlayer spacing can be explained by contraction of the pseudographitic domains. This in turn makes room for Na cluster formation in the voids between the graphitic domains (increased plateau capacity) and reduces the amount of available intercalation sites (decreased slope) [50].

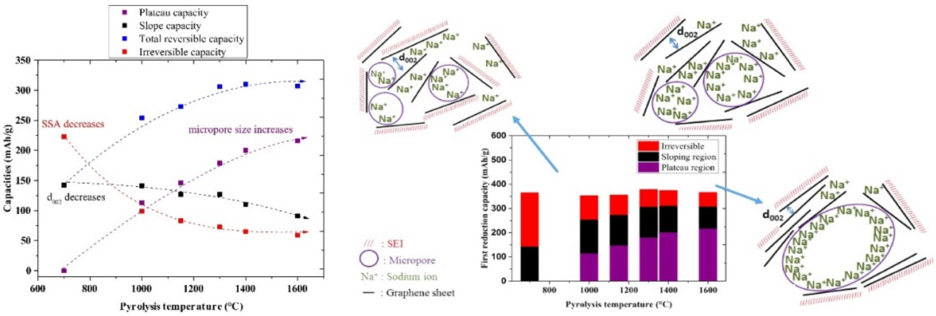

Figure 4. Left: correlations between different capacity values and pyrolysis temperature. Temperature trends of physical characteristics that are associated with different types of capacity trends noted in figure. Right: Depiction of strucutral changes and Na-storage mechanisms [50].

Bommier et al. postulated that Na storage could be further divided into three steps (**Figure 3c**). First, adsorption on defect sites as these have low energy unfilled molecular orbitals that effectively store extra electrons, which increases the binding energy with Na and allows sodiation to happen at higher potentials vs Na/Na^+, i.e. in the sloping region. Then, as the surface sites of pseudo-graphitic domains become progressively sodiated, intercalation into the inter-layer space should commence. They explain the third step of sodium deposition on pore surfaces or the basal planes of pseudographitic domains with the increase of diffusivity at low potentials, obtained by using galvanostatic intermittent titration technique (GITT) [61].

4.2.2 Hydrothermal carbonization (HTC)

The HTC method is very attractive due to its simplicity. It only requires low temperatures (normally below 300 °C) and is cheap and "green" since it does not require organic solvents or expensive catalysts. HTC process involves breaking up the carbohydrate into a furan-like molecules in the first step, followed by the condensation/polymerization and carbonization reactions, after which a solid carbon-rich product is formed [63–65] as shown in **Figure 5** [66]. The microspheres produced by the HTC process are micrometer sized, mainly spherically shaped, and possess a core-shell structure consisting of a hydrophobic nucleus and a hydrophilic shell that contains reactive oxygen functional groups (i.e. hydroxyl, carbonyl, carboxylic, etc.) [63–65]. However, the HTC material requires pyrolysis to further reduce hydrogen and oxygen content in the material, increase conductivity and form graphitic domains necessary for Na insertion into micropores.

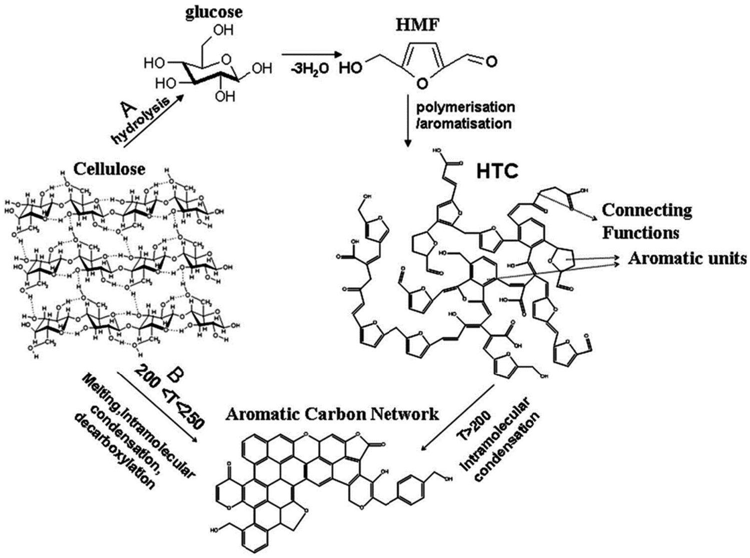

Figure 5. An example of HTC mechanism with cellulose proposed by Titirici et al. [66].

4.3. $Na_3V_2(PO_4)_3$ positive electrode material

Sodium vanadium phosphate ($Na_3V_2(PO_4)_3$ or NVP) is a NASICON–type material [27] with a very flat potential plateau at 3.4 V and theoretical capacity of 118 mAh g^{-1}. The reaction in the NVP positive electrode is based on a two-electron reaction of $Na_3V_2(PO_4)_3 \rightleftarrows NaV_2(PO_4)_3 + 2Na^+ + 2e^-$ [67]. NVP has an open NASICON framework (**Figure 6**) made of VO_6 octahedra and PO_4 tetrahedra between which Na ions can diffuse through interstitial sites and 2 Na^+ can be reversibly extracted [68,69].

Superb high-power performance (71.7 mAh g^{-1} at 99.3C) has been reported in the literature, which has been achieved through careful particle morphology optimization [70]. Excellent electrochemical performance and low manufacturing costs set the material price of performance at 3.7 \$ Wh^{-1} kg [71]. Its fluorinated analogue with higher energy density ranks at 3.5 \$ Wh^{-1} kg.

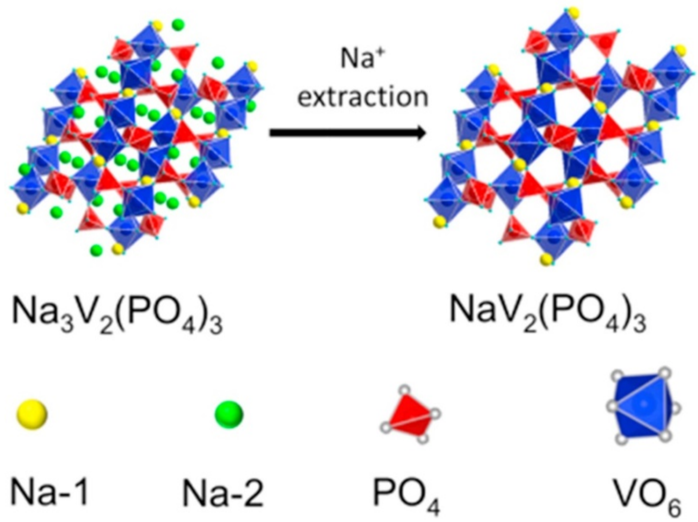

Figure 6. Fully sodiated $Na_3V_2(PO_4)_3$ structure and the de-sodiated $NaV_2(PO_4)_3$ structure [72].

4.3.1 Glycine-nitrate process (GNP)

Glycine-nitrate process (GNP) is a sub-category of solution combustion synthesis (SCS) methods, which are based on fast redox reactions between an oxidant (commonly nitrates) and a fuel (organic substances) in the presence of metal ions [73]. Effectively, SCS is a combination of sol-gel [74] and propellant chemistry [75]. There are many advantages to using GNP. Firstly, all the reactants will be dissolved, which ensures intimate mixing of the ions and is crucial to ensuring formation of pure phases [76]. Secondly, the reaction is very quick, which reduces time for particle agglomeration and enables to produce small particles [77] that are necessary for high power density battery cells. Thirdly, this method can be turned into a flow process, which makes it industrially scalable [73]. GNP and its variations have been used by the solid-oxide fuel cell research community [73,77,78] and to some extent by the battery community to synthesize and study materials like $NaTi_3(PO_4)_3$ [79], $Li(Ni_{1/3}Mn_{1/3}Co_{1/3-x}Na_x)O_2$ [80], $LiNi_{1/3}Co_{1/3}Mn_{1/3}O_2$ (urea as fuel) [81], $Li_4Ti_5O_{12}$ (lactic acid as fuel) [82], $ZnFe_2O_4$ [83], $Na_{0.44}MnO_2$ [84] and substituted $Na_{0.44}MnO_2$ bronzes [85–88].

4.4 Role of electrolytes

Electrolytes play a vital role in both LIBs and NIBs. The electrolyte acts as an ionic conductor to transport Na ions back and forth between the positive and the negative electrode as cells are charged and discharged. Nowadays, most research is directed to the study of electrolytes containing non-aqueous aprotic solvents as these enable higher cell potentials than water-based electrolytes [18]. Due to the inherent thermodynamic instability of high voltage LIBs and NIBs, the electrolyte is also critical to stabilizing the negative electrode surface. Commonly used carbonates decompose at E < 1.0 V vs Na/Na^+, but in the process form an electrically insulating, but ion conducting film on the electrode surface called the Solid Electrolyte Interphase (SEI). SEI formation reactions cause lower coulombic efficiency on the first cycle due to the irreversible nature of the decomposition reactions. It has been found that the SEI in LIBs composes of LiF (if $LiPF_6$ is used as the salt), $LiCO_3$, Li_2O, semicarbonates and polyolefines [22]. If the SEI did not form during the first charge cycle then the solvents would either continue decomposing on the surface of the electrode or the solvent would co-intercalate with the cation into the interlayer space of the carbon if the solvation energy was high enough. SEI formation in LIBs has been extensively studied and it is known to function effectively, which gives LIBs a long cycle life. Usually a mixture of cyclic and linear carbonates is used. Ethylene carbonate (EC) is a common component due to its high dipole moment, dielectric permittivity and boiling point. However, EC is solid below 39 ºC and has a high viscosity. Therefore, a linear carbonate like dimethyl carbonate (DMC) or diethyl carbonate (DEC) with low viscosity and high boiling point is added to the mixture to compensate for EC's disadvantages. Also, EC decomposes at a higher potential which means it will form the SEI faster than other solvents [89].

Table II. Physical properties of solvents used in this work [90–94].

Solvent	μ (D)	ε (25 °C)	T_m (ºC)	T_b (ºC)	η (mPa s)
H_2O	1.85	78,4	0	100	1
PC	4.94	64.92	−54	242	2.53
EC	4.9	90 (40 °C)	39	248	1.86 (40 °C)
DMC	0.88	3.12	3	90	0.59
DEC	1.1	2.805	−74.3	126	0.7534

μ – dipole moment, ε – dielectric permittivity, T_m – melting point, T_b – boiling point, η – viscosity. Green – advantages, red – disadvantages.

In NIBs, propylene carbonate (PC) has many advantages, but the downside is its high viscosity. It also can co-intercalate between graphene layers and into the microporosity with the cation. However, mixtures of EC:PC have shown good cycling performance [95]. Advantages and disadvantages of different solvents are shown in **Table II**.

The most common salts used in NIBs are $NaPF_6$ and $NaClO_4$. Unfortunately both have some disadvantages – pure $NaPF_6$ is difficult to find and $NaClO_4$ is explosive [96].

Furthermore, SEI stability in NIB cells is much lower than in LIBs due to higher solubility of Na-based electrolyte decomposition products [7,8], which is why it is necessary to learn more about the mechanism of reductive decomposition of Na-based electrolytes on carbon electrode surfaces.

4.5 Methods for electrochemical characterization

4.5.1 Cyclic voltammetry (CV)

Cyclic voltammetry (CV) is a powerful electrochemical method for determining the redox activity and charge storage properties of an electrode material. Continuous scanning enables the user to determine the potentials at which reactions take place in the studied electrochemical cell and assess their reversibility. The working electrode potential is swept linearly between two potential limits and the current response is recorded. If the cell potential reaches a value at which electron transfer takes place, the potentiostat has to apply a higher current to maintain the desired potential scan rate and so a peak is recorded on the cyclic voltammogram, i.e. potential versus current response. Since reactions in batteries are rather slow, low potential scan rates $v = \pm dE/dt$ between 0.01 mV s^{-1} and 1 mV s^{-1} are applied [97].

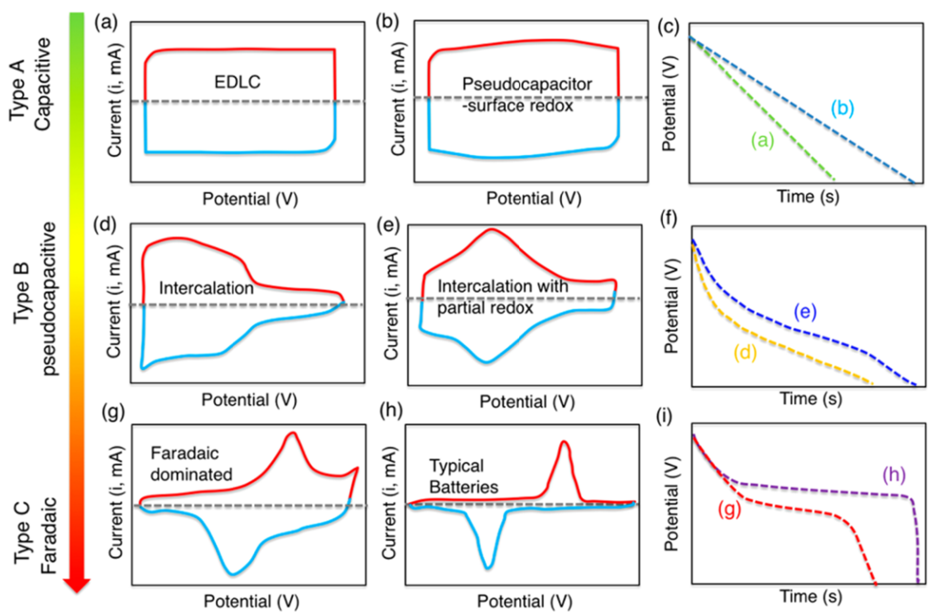

Figure 7. Cyclic voltammograms (a, b, d, e, g, h) and galvanostatic discharge profiles (c, f, i) for electrode materials with different charge storage mechanisms [97]. EDLC – electric double layer capacitor.

Common features found in CV plots of hard carbon electrodes are intercalation with partial redox (**Figure 7e**) during the first cycle when intercalation is accompanied by SEI formation reactions and intercalation (**Figure 7d**) after the first cycle when the SEI has stabilized.

4.5.2 Galvanostatic charge-discharge (GCD) method

GCD is probably the most popular method for battery materials characterization. In GCD, the current is held at constant value while the potential is measured as a function of time [98]. Cycling usually takes place in a fixed potential region (upper and lower cut-off potential) and can extend from a single charge to thousands of cycles. The results are usually plotted as *E* vs capacity (*Q*) graph. Active material capacity is calculated using the following equation:

$$Q = \frac{It}{3600 \cdot m_{\text{active}}}, \tag{1}$$

where Q is specific capacity (mAh g^{-1}), I applied current (mA), m_{active} is the weight of active material (mg) in the electrode, and t time at a given point.

This method provides valuable information such as, how much charge can the electrode store and release in a given potential region; how many reactions occur at which potentials and how much charge they consume; the reversibility of the reactions; coulombic efficiency of the battery cell and the stored specific energy, when integrating the $E - Q$ profile. The latter can be calculated using the trapezoid method:

$$E_g = \sum_{n=0}^{N-1} \frac{1}{2} (V_n + V_{n+1})(Q_{n+1} - Q_n), \tag{2}$$

where E_g is specific energy (Wh kg^{-1}), V is cell cell potential (V), n the number of datapoints, Q specific capacity at a given datapoint, derived from Equation (1).

In battery research, applied currents are usually expressed as C-rates, which is a measure of the rate at which a battery is charged or discharged relative to its maximum capacity. For example, if an electrode active material has a specific capacity of 100 mAh g^{-1}, then 1C would correspond to 100 mA g^{-1}, 5C to 500 mA g^{-1}, C/10 to 10 mA g^{-1} etc. The main advantage of this approach is that it enables to normalize currents by battery capacity, which makes comparison of different batteries easier.

Typical GCD profile features for hard carbons are shown in plots (f) and (i) in **Figure 7**. Intercalation with partial redox (curve (e) in plot (f)) occurs during the first cycle when Na intercalation into the interlayer space is accompanied by SEI formation reactions after which the surface is stabilized and only features of intercalation are visible in the sloping region (curve (d) in plot (f)). Redox reactions and curve (h) in plot (i) are common for the plateau region.

4.5.3 Electrochemical impedance spectroscopy (EIS)

Electrochemical impedance spectroscopy (EIS) is an advanced and detailed characterization method for investigating a wide variety of electrochemical systems [99,100]. EIS enables the user to separate and quantify simultaneously occurring processes on a complex interface that would otherwise be indistinguishable from one another with other methods such as CV or GCD. In EIS, a sinusoidal alternating voltage (av) perturbation is applied (usually in from 5 mV to 50 mV) and the alternating current (ac) response of the system is recorded. The av frequencies (*f*) range from 300 kHz to 1 mHz. Also, a bias voltage is applied to characterize the system at a certain SOC and/or potential region.

The input signal of EIS is a modulation function:

$$E(t) = E_0 \sin\omega t, \tag{3}$$

where E_0 is the maximum amplitude of the av signal, $\omega = 2\pi f$ is the angular frequency and f is the av frequency in Hz. According to Ohm's law ($I = E/R$), the current response $I(t)$ of an ideal resistor is:

$$I(t) = I_0 \sin\omega t, \tag{4}$$

where I_0 is the maximum amplitude of current. This means that $I(t)$ is in phase with $E(t)$, related as in the case of direct current (dc). In case of a capacitor, the current response $I(t)$ will be a sinusoid at the same frequency, but shifted in phase in case of capacitive or inductive processes:

$$I(t) = I_0 \sin(\omega t + \varphi), \tag{5}$$

where $I(t)$ is the current at time t, I_0 is the current amplitude and φ is the phase angle shift by which the voltage follows the current [99]. An ideal capacitor will cause a −90º phase angle shift in the current response, i.e. the ac signal will be a $\cos\omega t$ function. According to Ohm's law, the impedance is defined as the ratio of voltage and current:

$$Z = \frac{E(t)}{I(t)}. \tag{6}$$

The instantaneous quantity of charge q in the case of a purely capacitive circuit element on the capacitor electrodes during an applied av signal is:

$$q = CE(t) = CE_0 \sin\omega t, \tag{7}$$

where C is capacitance (F) and from which the corresponding current response $I(t)$ can be retrieved:

$$I(t) = \frac{\mathrm{d}q}{\mathrm{d}t} = C\frac{\mathrm{d}E(t)}{\mathrm{d}t} = \omega C E_0 \cos \omega t. \tag{8}$$

According to Equation (8) and Ohm's law, $1/\omega C$ has the dimension of resistance, but unlike R, its magnitude decreases with increasing frequency. So, the impedance of a capacitive element Z'', known as the imaginary part of impedance, is expressed as:

$$Z'' = -\frac{1}{\omega C}. \tag{9}$$

According to Equation (6), the response signal of a resistive element, known as the real part of impedance is expressed as $Z' = R$.

Both capacitive and resistive components exist in a real battery and the total system response to an applied av is a complex frequency-dependent signal due to the phase angle between $E(t)$ and $I(t)$. Complex number notation (imaginary unit $\mathrm{j} = \sqrt{-1}$) is used to simplify the representation of EIS signal by assigning capacitance part of the signal to the imaginary plane and resistance to the real plane of impedance. The current $I(t)$ is equal for elements connected in series, therefore the combination of Equations (3) to (9) gives:

$$E(t) = I(t)\left(R + \frac{1}{\mathrm{j}\omega C}\right) = I(t)Z, \tag{10}$$

where Z is the complex impedance:

$$Z = Z' + \mathrm{j}Z'' = R - \frac{\mathrm{j}}{\omega C}\ , \tag{11}$$

$$|Z|^2 = (Z')^2 + (Z'')^2. \tag{12}$$

By applying signals of differing frequencies, processes with different time constants can be probed. In general, for electrochemical systems, three main non-distributed fundamental processes that can be ascribed are: resistive (such as faradic charge transfer) corresponding to a 0º phase shift between potential and current signals; diffusion (such as semi-finite length diffusion of reactants) corresponding to a −45º phase shift, and capacitive (such as electrostatic, adsorption rate limited electrical double layer formation with capacitance) processes that show a −90º shift between the ac voltage and current signals. The dependence of the interfacial resistance on applied signal frequency can be calculated from the measurement and plotted in a complex plane, called the Nyquist plot (**Figure 8a**) whereby the real part of the resistance Z' shows the resistive and the imaginary part Z'' shows the capacitive part of the interfacial resistance.

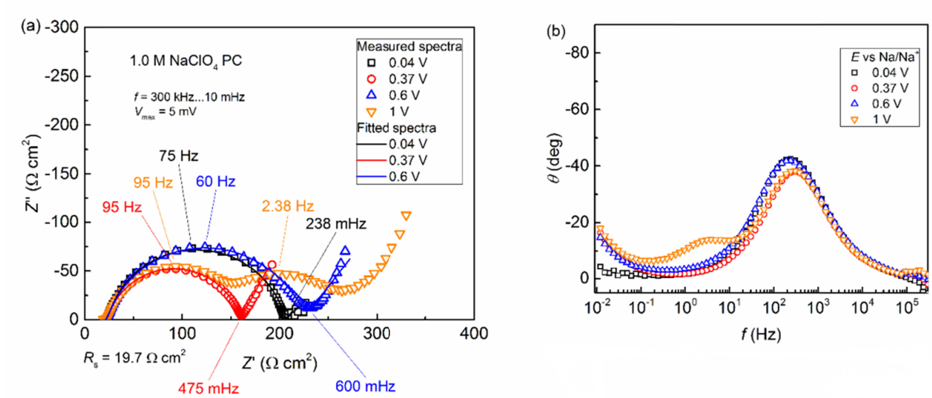

Figure 8. EIS data representations on complex plane, known as the Nyquist plot (a) and phase angle vs frequency plot, known as the Bode plot (b) [II].

4.5.3.1 Equivalent circuit fitting

Equivalent circuits (EQCs) of discrete electrical components can be used to connect electrochemical behavior of a real system to an idealized model, which enables to quantify simultaneously occurring processes in the system. Typically, the investigator calculates theoretical spectra based on an equivalent circuit, which is representative of the physical processes taking place in the system under investigation and then fits the calculated data to the experimental data to see how accurately the proposed model describes the system under study [99]. However, care must be taken when including too many EQC components in the model as these might lose their physical meaning [101] and produce mutually degenerate networks, i.e. different EQCs that produce identical impedances over the entire real axis of frequencies [102].

Aside from common EQC elements like resistors and capacitors, complex interfaces and heterogeneous surfaces require the use of elements such as the Warburg impedance and the constant phase element (CPE) to model ion diffusion in solids or characterize processes with distributed time constants, respectively [100].

Diffusion impedance Z_W is given as:

$$Z_W = R_D \frac{\tanh((j\omega\tau_W)^{\alpha_W})}{(j\omega\tau_W)^{\alpha_W}}, \tag{13}$$

where R_D is diffusion resistance, α_W the fractional exponent and τ_W Warburg diffusion time constant. τ_W is defined via effective diffusion length L in mm and effective diffusion coefficient D in mm^2 s^{-1} by the following expression [103]:

$$\tau_{\mathrm{W}} = \frac{L^2}{D}. \tag{14}$$

The constant phase element was developed in detail by Orazem et al. to describe behavior that has been attributed to surface heterogeneity, oxide films or to continuously distributed time constants for charge-transfer reactions [100, 104]. Low frequency constant phase element impedance is expressed as:

$$Z_{\mathrm{CPE}} = A^{-1}(\mathrm{j}\omega)^{-\alpha_{\mathrm{CPE}}}, \tag{15}$$

where A is the CPE coefficient, ω is radial frequency and α_{CPE} is the fractional exponent. CPE is a universal approximation and can model other circuit elements as well. For example, if $\alpha_{\mathrm{CPE}} = 1$, then A has the dimension of capacitance, if $\alpha_{\mathrm{CPE}} = 0$, then A becomes a resistor.

The quality of the modelling function is evaluated using chi-square function (χ^2) and weighted sum of the squares (Δ^2) to get a general idea of the fit accuracy and relative parameter error estimates [105].

4.5.4 *Operando* total X-ray scattering method

The conventional X-ray diffraction (XRD) methods probe for the presence of long-range order towards a solution of the average crystal structure. Experimentally, structural information about long-range, periodic atomic ordering is reflected in the Bragg scattering, while local atomic structural deviations from the average structure mainly affect the diffuse scattering intensities. In order to obtain structural information about both average and local atomic structures, a technique that takes into account both Bragg and diffuse scattering needs to be employed, such as the total scattering atomic pair distribution function (PDF) technique [106].

Operando X-ray total scattering with PDF analysis enables the investigator to follow the structural changes that take place during charge and discharge of the hard carbon electrode in real time. The PDF, denoted as $G(r)$, is the Fourier transform of the normalized reduced total scattering structure function, $F(Q)$, which utilizes the total scattering data obtained to high Q-values. This real-space function contains peaks at distances, r, representing pairs of atoms in the structure, where sharp peaks indicate a well-defined structure of the hard carbon material, resulting in a histogram of interatomic distances. Additionally, the intensities of the peaks are related to the relative abundance of each atom–atom distance. Consequently, the PDF analysis provides an intuitive tool to study the local atomic structure of a material. To overcome these problems related to the low scattering power of carbon and sodium, a custom-built low-background operando setup must be used for achieving useful data for PDF analysis rather than conventional pouch or coin cell-like cells for synchrotron *operando* experiments. A custom-made capillary-based battery cell allows selective scattering from only the electrode material of interest [107,108]. In this cell configuration, the X-ray beam only interacts with the capillary, electrolyte and the active material, the capillary and the electrolyte produce a baseline signal, which is subtracted from the total scattering intensity for subsequent PDF analysis (**Figure 10**). With this setup the signal from weakly scattering active material can be more effectively isolated as the X-rays do not need to penetrate multiple materials like X-ray windows, current collectors and separators.

5. EXPERIMENTAL

5.1 Electrode materials and electrolytes

5.1.1 Glucose-derived hard carbon (GDHC)

5.1.1.1 GDHC synthesized at 1100 °C (I-IV)

Glucose derived hard carbon used in papers [I–IV] was synthesized using the following procedure: D-glucose (≥99.5% purity, Sigma) was dissolved in ultrapure water (Milli-Q$^+$, 18.2 MΩ cm, Millipore) to obtain a 2 M solution, then hydrothermal carbonization (HTC) of 2 M D-(+)-glucose solution in H_2O (200 ml, Milli-Q$^+$) was carried out in a high-pressure reactor (Büchi limbo, vessel volume 285 ml) at 200 °C for 24 hours. Thereafter, the carbonaceous material was collected and washed several times with Milli-Q$^+$ water, and dried overnight in a vacuum oven (Vaciotem-TV) at 120 °C and 50 mbar [109]. The dried carbonaceous material was then pyrolysed in a quartz stationary bed reactor at 1100 °C under Ar flow for 2 h using heating ramp rate of 10 °C min^{-1}. Final treatment of the carbon material was the reduction of surface functional groups with H_2 (purity 99.9999%) at 800 °C for 2 hours. The reduced carbon materials have demonstrated very wide (3.2 V) and stable potential region of ideal polarizability in surface inactive non-aqueous electrolyte solutions [110].

The hard carbon powder was mixed with Super P (Alfa Aesar) and polyvinylidene difluoride (PVDF, Sigma-Aldrich) in a 75:15:10 weight ratio and stirred overnight using N-methyl-2-pyrrolidone (NMP, Sigma-Aldrich, 99.5%) as the solvent. The resulting mixture was cast onto copper foil using the tape casting technique. The cast electrodes were dried under vacuum at 120 °C for 24 h.

5.1.1.2 GDHCs synthesized at 1400–1600 °C (V)

The HTC precursor was prepared using the same procedure described in 5.1.1.1, but the dried carbonaceous material was then pyrolysed in an alumina tube reactor at temperatures from 1400 °C to 1600 ºC under Ar flow (200 mL min^{-1}) for 2 h, using heating ramp rate of 4 °C min^{-1} [V]. No hydrogen treatment followed, because comparisons of H_2 treated GDHCs and untreated GDHCs indicated that hydrogen treatment increases capacity, but only in the sloping region, which is not instrumental to hard carbon performance as a negative electrode in a NIB. In fact, increase of capacity in the sloping region indicates an increase in surface area which in turn means higher irreversible capacity [111–113].

The obtained hard carbon powder was mixed with Super P and PVDF in a 75:15:10 or 85:4:11 (denoted as 'b') weight ratio and stirred overnight using NMP as the solvent. The resulting mixture was cast onto aluminum foil (MTI, thickness 15 μm) using tape casting technique. The cast electrodes were dried under vacuum at 120 °C for 24 h and then moved to the glovebox [V].

5.1.2 $Na_3V_2(PO_4)_3$ (NVP)

In step 1 (**Figure 9**), stoichiometric amounts of $NaNO_3$ (≥99%, Honeywell), $NH_4H_2PO_4$ (99.9%, Acros) and NH_4VO_3 (>99.0%, Honeywell) were dissolved in deionized water along with varying amounts of citric acid (CA, >99.5%, Sigma-Aldrich) and glycine (G, ≥99%, Sigma). Exact amounts used are summarized in **Table III**, and the overall schema depicted in **Figure 9**. Citric acid acts as both fuel for combustion and as a complexing agent that helps dissolve NH_4VO_3. Glycine is a common fuel used in nitrate combustion reactions [78,114,115], which can also serve as a precursor to carbon shell formation around NVP particles. In step 2, the resulting mixture was stirred and heated at 90 °C to remove excess water and produce a viscous gel.

In step 3, three different approaches to form a precursor were employed from this point onward (**Figure 9**). Option 3a – the viscous solution was heated in the beaker until a foam was formed, denoted as NVP-Stir. According to Wang et al. [116] a spontaneous combustion of the gel should have happened, but such an effect was not observed. Option 3b – the viscous solution was either dropped onto a hot Pt-crucible (400 °C, heated with a natural gas flame), denoted as NVP-Drop or sprayed onto the Pt-crucible using a bottle spray, denoted as NVP-Spray. The precursor materials were thereafter ball-milled for 2 hours at 300 rpm after which, in step 4, the mixture was heat treated in a quartz tube furnace at 900 °C (ramp rate 10 °C min^{-1}) under Argon (grade 5.0, AGA AS) flow (900 mL min^{-1}) for 4 hours. Efforts were made to scale up the synthesis and produce bigger batches of the material using the Spray method. The first experiment was a scale-up of the NVP-Spray method, denoted as Spray-2 and the second was a slight modification of Spray-2 in which no glucose was added to the precursor, denoted as Spray-3 [V].

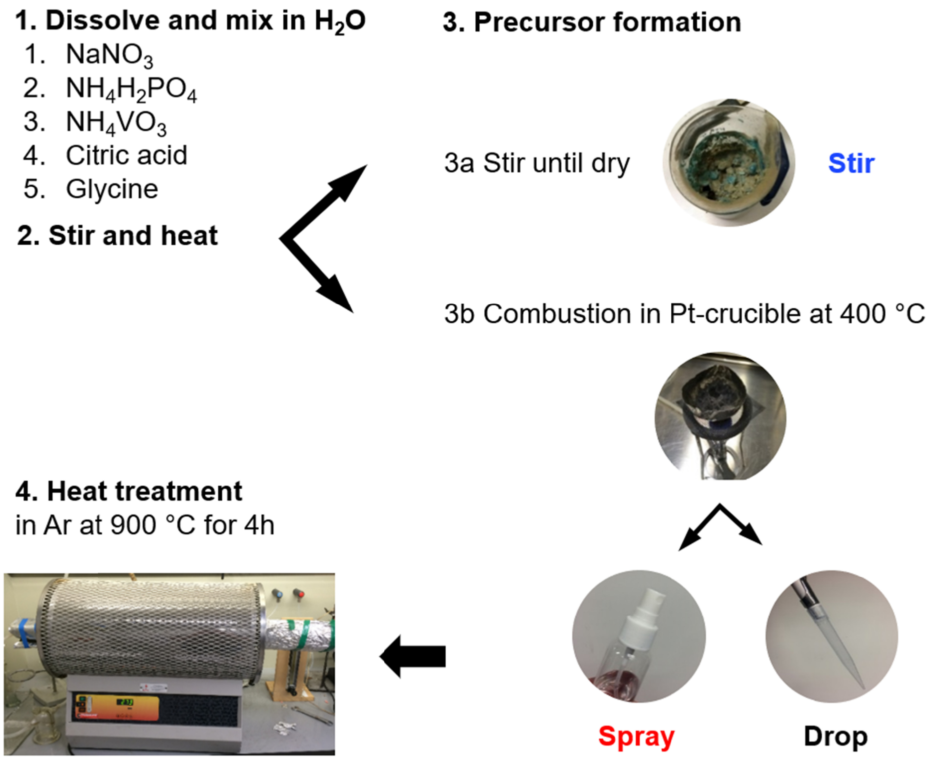

Figure 9. Synthesis stages of NVP.

Table III. Molar ratios of elements (in relation to V), added glucose to the precursor and heat treatment (HT) yields of the synthesized materials. Explanations of abbreviations given in text.

Sample	$m_{NH_4VO_3}$ (g)	Na:V	P:V	CA:V	G:V	Fuels:V	Glucose (wt %)	HT yield (%)
NVP-Stir	0.513	1.5	1.5	3.73	0	3.73	0	92
NVP-Drop	0.514	1.5	1.5	3.75	0	3.75	0	36
NVP-Spray	0.513	1.5	1.5	1.15	1.05	2.20	25	70
NVP-Spray-2	6.442	1.5	1.5	1.15	1.05	2.19	25	71
NVP-Spray-3	6.669	1.5	1.5	1.15	1.05	2.20	0	88

5.1.3 Electrolytes

The salts and solvents used in this work are summarized in **Table IV** and electrolytes in **Table V**. All salts and solvents were stored in the glovebox and all electrolyte solutions were also prepared in the glovebox.

Table IV. Salts and solvents used in this work.

Abbreviation/chemical formula	Name	Purity	Manufacturer
Salts			
$NaClO_4$	Sodium perchlorate	98%	Sigma-Aldrich
$NaPF_6$	Sodium hexafluorophosphate	99%	Alfa Aesar
KPF_6	Potassium hexafluorophosphate	99%	Abcr GmbH
$LiPF_6$	Lithium hexafluorophosphate	≥99.99%	Aldrich
$LiClO_4$	Lithium perchlorate	≥99.99%	Aldrich
Solvents			
EC	Ethylene carbonate	99%	Sigma-Aldrich
PC	Propylene carbonate	99.7%	Sigma-Aldrich
DMC	Dimethyl carbonate	99%	Sigma-Aldrich
DEC	Diethyl carbonate	99%	Aldrich
FEC	Fluoroethylene carbonate	99%	Sigma-Aldrich

Table V. Electrolyte solutions used in the study.

Molarity	Salt	Solvent(s)	Ratio by volume	Used in paper
1.0 M	$NaClO_4$	PC		I, II, III
1.0 M	$NaPF_6$	PC		III
1.0 M	$NaPF_6$	EC:DMC	1:1	II
0.8 M	KPF_6	EC:DMC	1:1	II
0.8 M	KPF_6	EC:DEC	1:1	II
1.0 M	$LiPF_6$*	EC:DMC	1:1	II
1.0 M	$NaPF_6$	EC:PC	1:1	III, V
1.0 M	$NaClO_4$	EC:PC	1:1	III
1.0 M	$LiPF_6$	EC:PC	1:1	III
1.0 M	$LiClO_4$	EC:PC	1:1	III
0.5 M	$NaClO_4$	PC:FEC	98:2	IV

* – Commercially prepared solution (battery grade, Aldrich)

5.2 Electrochemical measurements

Electrochemical performance of half cells was evaluated at 23 ± 0.5 ºC in 2-electrode setups using EL-Cell Combi (EL-CELL GmbH) stainless steel cells or 2032 coin cells (Hohsen) using GDHC or NVP working electrode (S = 2 cm^2) as the working electrode and a counter electrode of the same metal as the salt cation i.e. Li foil (99.9%, Goodfellow), Na metal (dry stick, 99.8%, Acros) or K ingot (Reachim) for Li, Na and K salts, respectively. Glass fiber separators (EL-Cell GmbH) with thicknesses 1.55 mm and 0.26 mm were used in half and full cell measurements, respectively. All test cells were assembled inside an Ar-filled glove box (MBraun) were O_2 and H_2O content was less than 0.1 ppm. All electrochemical experiments were carried out using PMC-1000 potentiostat/ galvanostat/frequency response analyzer (Princeton Applied Research). The half cells were evaluated using galvanostatic charging/discharging (GCD), cyclic voltammetry (CV) and electrochemical impedance spectroscopy (EIS) methods. Measurements were set up and controlled using VersaStudio 2.49 software platform. All data analysis and scripting was performed using OriginPRO 2016 software. ZView 3.5b was used for equivalent circuit fitting. Applied and measured currents and calculated capacities are expressed per weight of active material in the electrode i.e. mA g^{-1} and mAh g^{-1}, respectively. EIS data are expressed per geometric area of the electrodes, Ω cm^2 for resistance and μF cm^{-2} for capacitance.

5.3 *Ex situ* physical characterization of electrochemically cycled electrodes

Various physical characterization methods were employed to determine whether charging the GDHC 1100 electrode (adsorption/desorption of sodium) affects carbon material's crystallinity and chemical composition on the surface. A half cell was assembled (described in 5.1.1.1) to charge the electrode with Na after which the cell was dissembled in an Ar- filled glove box and washed carefully with PC solvent to remove free salt from the electrode surface. Meanwhile, another electrode was wetted in the same electrolyte for equal period of time and washed with PC afterwards to compare whether salt precipitates affect the spectra. Additional spectra were acquired for a dry (pristine) electrode as well.

5.4 Physical characterization of active material powders and *ex situ* electrodes

The particle morphology and size of GDHC 1100 and electrode surface morphology of NVP-Drop were studied using HeliosTM Nanolab 600 system at 10 kV electron beam and using a secondary electron detector. GDHC 1400 –

1600 were investigated using ZEISS EVO 15MA microscope at 20 kV electron beam and secondary electron detector.

For detailed morphology studies of GDHC 1100, HRTEM on a Tecnai 12 instrument operated at 120 kV accelerating voltage was employed. The TEM specimens were prepared from ultrasonic dispersions of the corresponding samples in ethanol. One drop of each suspension was deposited onto a copper grid covered with a holey carbon film.

Structural and crystallographic parameters were obtained from powder diffraction data using Bruker D8 Advanced diffractometer with Ni filtered CuK_α radiation (λ = 1.5406 Å, 0.3° divergence slit, 0.6 mm wide parallel beam, two 2.5° Soller slits and LynxEye line detector). Scanning step of 0.01° for 2θ was applied from 3° to 95°. Diffrac plus BASIC Evaluation Package (Bruker AXS GmbH) and ICDD PDF4+ Release 2018 database were used for interpretation of XRD patterns.

N_2 sorption isotherms of the synthesized GDHC 1100 material were measured using ASAP 2020 system (Micromeritics, USA) at 77 K. The specific surface area (S_{BET}) and the total volume of pores (V_{tot}) of GDHC powder was calculated from N_2 adsorption isotherms. S_{BET} was calculated according to the Brunauer-Emmett-Teller (BET) method and V_{tot} was calculated from the adsorbed amount near the saturation pressure of nitrogen (p/p_0 = 0.95). GDHC 1400 – 1600 surface area measurements were carried out using CO_2 at T = 273.15 K and analyzed using 2D NLDFT heterogeneous surface model.

Raman spectra were acquired with Renishaw inVia Raman Microscope using 514 nm laser wavelength. All Raman measurements of electrodes were carried out in an argon-filled box with a glass window to avoid reactions with moisture in the air.

Agilent 8800 triple Q ICP-MS with CETAC LSX–213 G2+ Laser Ablation System was used to carry out laser ablation inductively coupled plasma mass spectrometry (LA-ICP-MS) measurements of pristine, wetted and sodiated electrodes.

Time of flight secondary ion mass spectra (TOF-SIMS) were measured using PHI TRIFT V nanoTOF surface analysis instrument (Physical Electronics, Inc., USA) using a 30 keV liquid Ga^+ ion gun. PHI nanoTOF II was used to obtain Ga^+ DC beam induced secondary electron images of the studied electrode surface.

5.5 *Operando* X-ray total scattering setup

5.5.1 Experimental setup

The capillary-based half cell in **Figure 10** consisted of aluminum and copper flat current collectors (width 700 μm, thickness 300 μm) coated with hard carbon (layer thickness 100–200 μm) and sodium metal, respectively. First, a hard carbon slurry was prepared in a fume hood by mixing 80 wt% hard carbon, 15 wt% polyvinylidene fluoride (PVDF) and 5 w% Super P in N-methyl-2-pyrrolidone (NMP), which was stirred for 72 hours. The aluminum wire was coated 2–3 times with the slurry using a spatula with subsequent drying for 30 min at 100 ºC after each application. After drying, the coated hard carbon was cut into 2 mm long electrodes. The electrodes were transferred to an Ar-filled glovebox and dried in a vacuum oven overnight at 80 ºC to remove residual water.

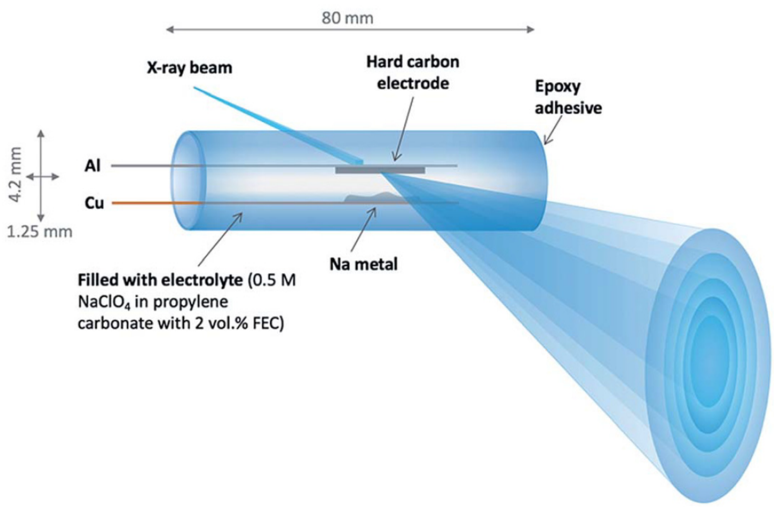

Figure 10. Schematic depiction of the *operando* capillary half cell [IV].

The electrodes were fixed with a UV-glue on a plastic spacer to obtain a constant distance and prevent a short. The separated electrode wires were placed in a rectangular boron silicate capillary (Hilgenberg) with an outer diameter of 4.2 × 1.25 mm and wall thickness of 125 μm, in which they were fixed with epoxy glue (Loctite 9492) and dried overnight at room temperature. The capillary was filled with 0.5 M $NaClO_4$ electrolyte (in PC with 2 vol% FEC). Finally, it was sealed by firstly applying a small amount of silicone grease at the capillary opening followed by a two-component epoxy glue.

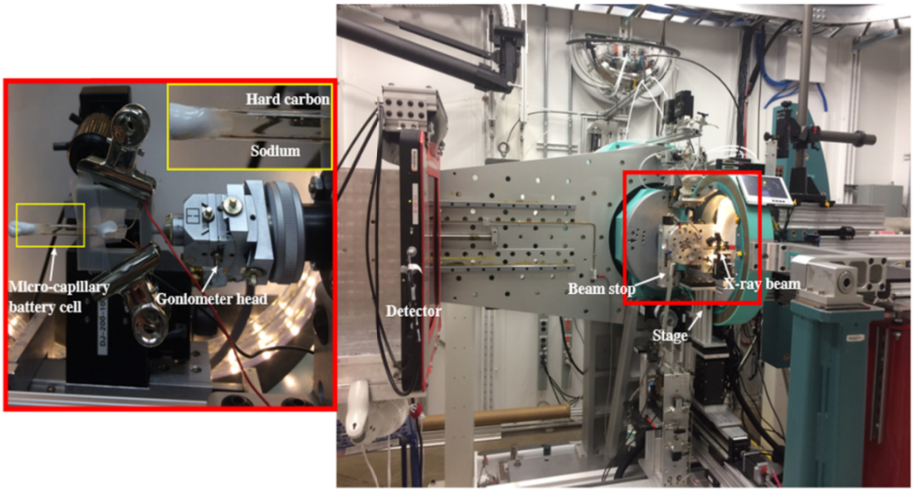

Figure 11. Experimental setup at beamline 11-ID-B, APS, for operando total scattering and PXRD measurements on the micro-capillary battery cell.

The mounting of the capillary half cell is illustrated in **Figure 11**. The half cell was placed in an insulating frame and mounted horizontally on a goniometer head. The cell leads were connected to a potentiostat (8-channel MACCOR® battery cycler) to charge and discharge the half cell at C/10 in *E* range from 0.01 to 2.1 V vs Na/Na^+ with 5 minutes of open-circuit potential (OCP) between the modes. Total scattering data were collected in transmission geometry using a PerkinElmer flat panel detector with a pixel size of 200 × 200 µm. A wavelength of 0.2114 Å was used and the X-ray beam was defined by slits: vertically 150 µm and horizontally 500 µm. A CeO_2 standard was used to calibrate the sample-to-detector distance. Total scattering data were collected by first measuring 4.5 minutes at a position on the hard carbon, where the best scattering signal from the electrode was found (Position 1, **Table VI**) with a detector distance of 18 cm. Afterwards, the capillary was moved in the vertical plane, so that data were collected at a point closer to the electrolyte, where a new frame was measured for 4.5 minutes (Position 2). The sample was then moved vertically 300 µm to collect data from the electrolyte for background correction (Position 3). The sequence of measurements, which made it possible to continuously subtract a representative electrolyte state, is tabulated in **Table VI**. The data collection sequence took 30 minutes, which was then continuously executed during the half cell operation. The data were integrated using Fit2D13 and the PDFs were obtained from the initial *operando* total scattering data by utilizing PDFGetX3 [117] with subsequent background subtraction of the background data measured in Position 3 [117,118].

Table VI. Tabulated sequence of measurements conducted during *operando* conditions.

Measurement	Position	Exposure time (minutes)
PDF	1	4.5
PDF	2	4.5
PDF (background)	3	4.5
PDF	1	4.5
PDF	2	4.5

5.5.2 Model structure used for fitting scattering data

In order to be able to quantify the structural changes of the hard carbon, a model was developed describing the atomic arrangement. The model is characterized as an altered, extended graphite structure, which can be assigned as an intermediate between the periodic 2H graphite structure and a single graphene layer model shown in the inset of **Figure 12** [59,119]. An increase of *c*-parameter from 6.7 Å (pristine 2H graphite [120]) to 7.0 Å was necessary to better describe the lower density of the hard carbon compared to graphite (1.52 g cm^{-3} vs 2.26 g cm^{-3}, respectively) [59,121] and the presence of turbostratic disorder in the structure suggested by Bommier et al. [61]. Real-space least-squares refinement of the pristine hard carbon was performed against experimental PDF data in the *r*-range from 1–15 Å. As seen in **Figure 12**, the presented model agrees well with previous studies, in which the PDF of the hard carbon is primarily dominated by in-plane carbon–carbon interaction and not significantly by the sheet–sheet correlation [119]. Specifically, as observed in **Figure 12**, the model resembles the experimental PDF very well above 4 Å. However, at lower *r*, especially at 3.2 Å, the model has difficulties fitting the features of the experimental PDF. The observed peak is consistent with previous *ex situ* PDF studies on the presence of seven-membered carbon rings with non-hexagonally bonded carbon rings [122].

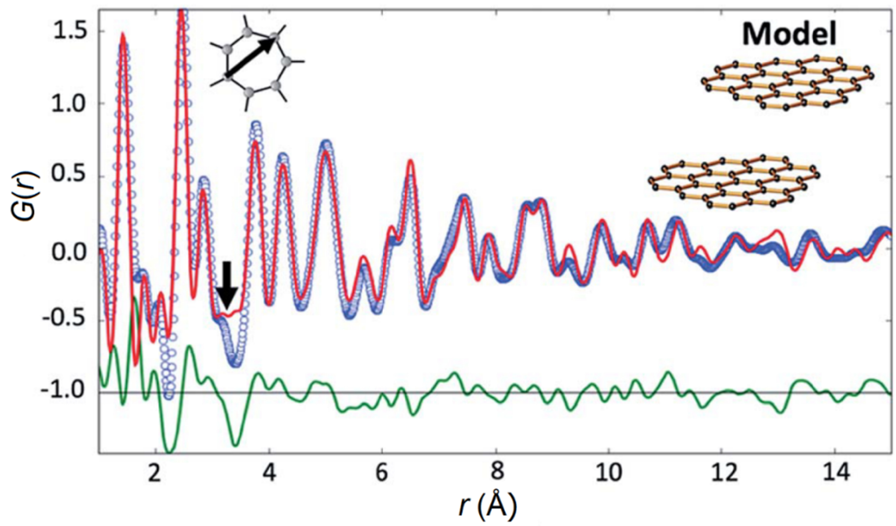

Figure 12. Refinement of first scan of hard carbon sodiation in the *r*-range from 1–15 Å. Inset shows the extended graphite model used for the refinement and the seven-membered ring related to the peak at 3.2 Å.

6 RESULTS AND DISCUSSION

6.1 Physical characterization

6.1.1 SEM data

The images in **Figure 13** reveal a similarity between GDHCs synthesized at various temperatures. Primary particle diameters are in the order of 400–500 nm and interconnected, with relatively smooth surface structure (GDHC 1100 and 1400). However, increasing HTT seems to cause particle deformation, because GDHC 1500 and 1600 are slightly larger and contain sharper features. However, sharper edges could provide a multitude of sorption centers for Na-ions.

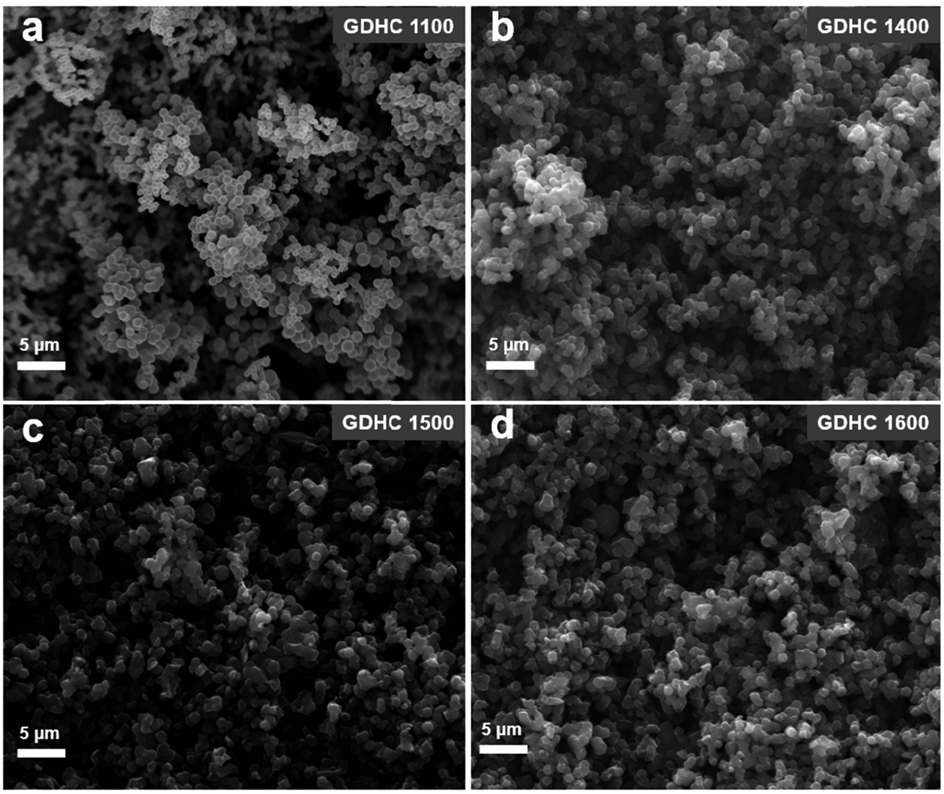

Figure 13. SEM images of the studied GDHC materials, number indicates pyrolysis temperature in °C.

The SEM image of GDHC 1100 electrode in **Figure 14** reveals that the composite electrode is quite homogeneous with clusters of nanospheric GDHC particles mixed with Super P. Fibers from glass fiber separator can be seen on the surface of the electrode.

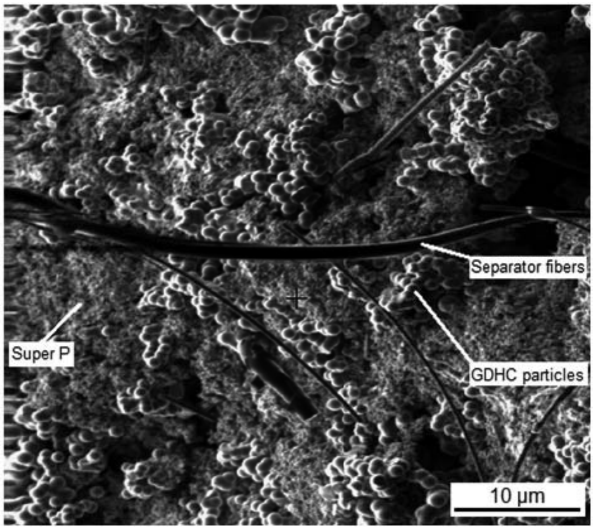

Figure 14. SEM image of GDHC 1100 electrode electrochemically charged with Na.

SEM image of the NVP-Spray precursor (**Figure 15a**) reveals a holey morphology. Particles are in varying sizes and shapes, but some plate-like structures with rough edges can be seen. The heat treated NVP-Spray consists of much smaller particles (**Figure 15b**) with a varying size distribution. Particle size distribution can be narrowed by combining an ultrasonic spray method that ensures a constant flow of droplets with a similar size and an electrostatic or cyclone collector to separate different fractions.

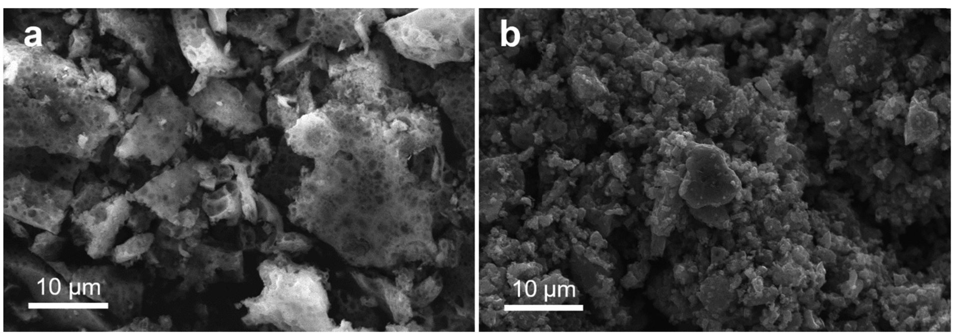

Figure 15. SEM images of NVP-Spray precursor (a) and NVP-Spray after heat treatment (b).

6.1.2 HRTEM data

HRTEM study of GDHC 1100 material revealed the microstructure at the atomic scale, demonstrating the formation of some graphitic layers onto a mainly amorphous nanospheric hard carbon material [I, II, IV]. Graphitic structures are clearly visible from **Figure 16**. The spherical particles appear to be hollow inside, which could serve as closed pores that enable reversible sodium storage [46,123]. Also, curved 5–7 layer graphitic domains can be observed.

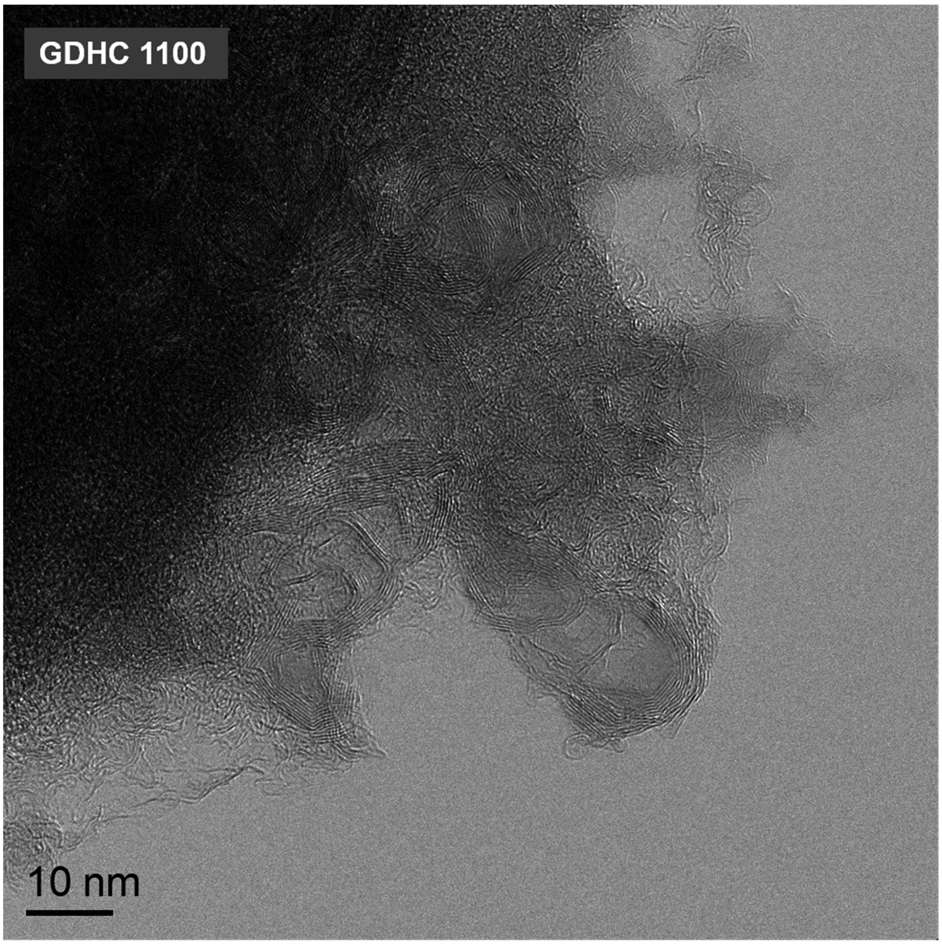

Figure 16. HRTEM image of GDHC material pyrolyzed at 1100 °C.

6.1.3 Gas sorption measurements

Based on the analysis of Brunauer-Emmett-Teller (BET) gas sorption measurement results, the calculated specific surface area (S_{BET}) and total micropore volume (V_{tot}) of the synthesized GDHC 1100 were ~238 $m^2\ g^{-1}$ and 0.11 $cm^3\ g^{-1}$, respectively.

CO_2 adsorption measurements were carried out to study the porosity of GDHC 1400–1600. N_2 sorption measurements were also conducted, but did not produce consistent results. The surface areas of GDHC 1400–1600 are likely much smaller than GDHC 1100, which is why CO_2 was used instead. **Table VII** shows specific surface area and total pore volume calculated from CO_2 sorption data using 2D NLDFT HS (2-dimensional non-local density functional theory heterogeneous surface) model. While both S_{DFT} and V_{DFT} decrease as T increases from 1400 °C to 1500 °C, an increase in both parameters at 1600 °C is observed. This can be explained by further breakdown or pore-opening of the hard carbon structure at elevated temperatures.

Table VII. Specific surface areas and total pore volumes calculated from CO_2 gas sorption data.

	S_{DFT} ($m^2\ g^{-1}$)	V_{DFT} ($cm^3\ g^{-1}$)
GDHC 1400	147	0.12
GDHC 1500	69	0.08
GDHC 1600	94	0.09

6.1.4 X-ray diffraction (XRD)

The GDHC 1100 has typical characteristics of an amorphous carbon – broad peaks at 24° and 43°, representing (002) and (100) planes, respectively.

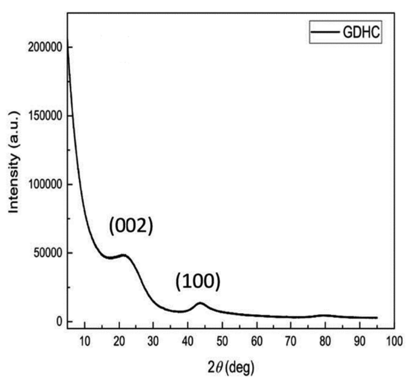

Figure 17. XRD pattern of the GDHC 1100 powder.

Calculated crystallite size is ~0.97 nm and cell parameters for 2H graphite model (space group P63/mmc) were a = 2.469 ± 0.019 and c = 7.657 ± 0.053 Å. As for the synthesized NVP, the X-ray diffraction (XRD) data in **Figure 18a** indicate that the formed precursors are amorphous by nature because no sharp peaks can be observed. However, after heat treatment all samples contain $Na_3V_2(PO_4)_3$ phase (**Figure 18b**). The NVP-Drop and NVP-Spray do not contain impurities and the intensities of XRD peaks match the diffractogram from the database. NVP-Stir has many unidentified peaks in the pattern that are the likely cause for stepwise GCD profiles [V].

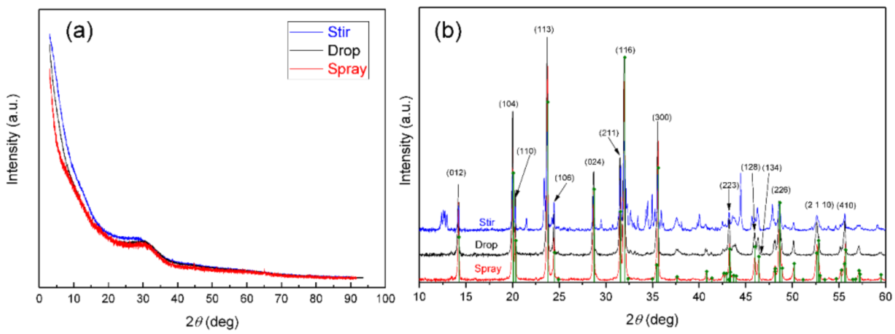

Figure 18. XRD patterns of NVP precursors (a) and NVP materials after heat treatment (b).

Impurities are probably caused by the inhomogeneity of the viscous Stir precursor during the last stages of heating. As water is evaporated from the mixture, the citric acid in the mixture turns the solution into an amorphous and sticky mass, which creates a temperature gradient in the mixture. This can result in heterogeneous distribution of elements in the mixture, which in turn leads to the formation of impurities during heat treatment. The droplets are much smaller and water evaporation is instantaneous with Drop and Spray method preventing temperature and concentration gradients from developing within the particles.

6.2 Cyclic voltammetry results

CVs were measured for GDHC1100||Na half cells at scan rates ranging from 0.1 mV s^{-1} to 1 mV s^{-1} [I]. The CVs in **Figure 19** have a characteristic shape [52] for hard carbon – a sharp reduction peak at $E < 0.1$ V vs Na/Na^+, a well-defined oxidation peak at $E = 0.2$ V vs Na/Na^+ and a flat but higher current plateau in $0.3 > E > 1.0$ V vs Na/Na^+ region, a characteristic of capacitive and pseudocapacitive behavior [97,124,125]. The reduction peak is associated with sodium adsorption and nanocluster deposition in the micropores and “closed pores” and the oxidation peak is associated with desorption and Na dissolution. The flat plateau with current at higher potentials is associated with Na intercalation between expanded graphene layers [48,58] and adsorption on the edges of graphitic domains [61]. The asymmetry in 1.0 > E > 1.5 V vs Na/Na^+ region at higher scan rates in **Figure 19a** implies that intercalation of Na^+ or partially solvated Na^+-PC species is hindered. That feature is absent from **Figure 19b**, where relatively slow scan rate of 0.5 mV s^{-1} is not exceeding the rate of the intercalation process.

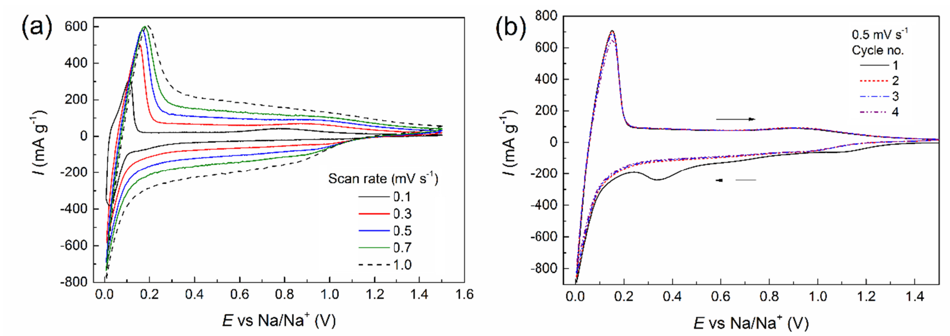

Figure 19. Cyclic voltammograms of GDHC 1100||Na half cells in 1 M $NaClO_4$ PC electrolyte at various scan rates (noted in figure) (a) and the first 5 cycles at 0.5 mV s^{-1} (b) [I].

Figure 19b shows the first four cycles of a newly assembled half cell. It follows that the system is reversible after the first cathodic scan since the CVs are practically identical. However, the reduction peak at 1.1 V vs Na/Na^+ is believed to be caused by the reduction reaction of residual water [8] in the electrolyte and the peak at 0.3 V vs Na/Na^+ is usually associated with electrolyte decomposition reactions on the electrode surface [18,126], in this case PC and ClO_4^-. However, taking into account the reproducibility of the current maximum at 0.1 V vs Na/Na^+, the formation of a stable SEI is questionable as PC is known for not forming a stable film upon decomposition and due to strong coordination to Na-ions [127] can co-intercalate between graphene layers, as observed in LIBs [128].

Li and K were used to learn more about the charge storage mechanism in GDHC 1100 and explore the differences between LIBs, NIBs and KIBs. The CVs in **Figure 20** reveal the vast differences in electrochemical performance of different alkali metal based systems. 1 M $LiPF_6$ EC:DMC (**Figure 20a**) reaches similar current densities in the peak regions as Na-based electrolytes in **Figure 20b** and **d**, but has less defined peaks. This implies that more layer-space is available for Li-ions, but adsorption and metallic cluster formation in the micropores is happening to a lesser extent. In the case of KPF_6, the linear carbonate (DMC or DEC) has a strong influence on the electrochemical processes on the electrode surface. Low current density throughout the CV cycle implies that DMC hinders K^+ electrochemical activity. A small reduction peak has formed at 0.05 V vs K/K^+, but no oxidation peak can be observed on the cathodic scan. On the other hand, the DEC containing electrolyte causes much higher current densities, showing a narrow reduction peaks and a broader oxidation peak. However, the potential hysteresis is bigger than that with Li- or Na-based half cells and current density is much lower. The potential hysteresis suggests that K^+ extraction from the electrode surface is hindered. The noted difference between the performances of DMC and DEC containing electrolytes could be caused by a stronger coordination between K^+ and DMC than between K^+ and DEC.

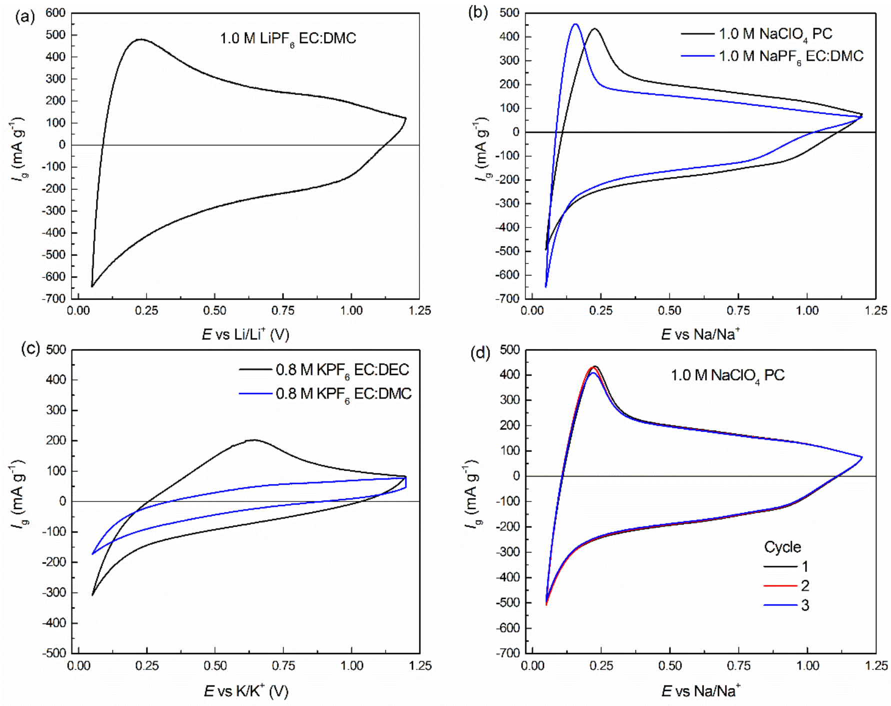

Figure 20. Cyclic voltammograms of Li^+ (a), Na^+ (b), K^+ (c) based half cells with GDHC 1100, electrolytes noted in figure. The reversibility of 1.0 M $NaClO_4$ PC demonstrated in (d) [II]. All CVs were recorded at 0.5 mV s^{-1} scan rate.

6.3 Galvanostatic charge-discharge data

Galvanostatic charge-discharge (GCD) results in **Figure 21** reveal considerable differences in the electrochemical behavior of Li^+-, Na^+- and K^+-based half cells. $LiPF_6$ EC:DMC leads to no plateaus formed in the GCD plot, which is in good agreement with CV data in **Figure 20a**, as notable peaks were missing from the CVs too. Such behavior has been previously observed in soft carbon||Li half cells [129–131]. The galvanostatic profile only contains a sloping part, which is similar to a capacitor-like linear $E - Q$ response. This suggests that the charge storage mechanism is almost purely based on intercalation (**Figure 7f**). As discussed in Section 4.5.1, one of the proposed mechanisms attributed to the plateau region capacity is metal cluster formation in the voids of the pseudographitic domains [50]. These voids can be the "closed nanopores" that are inaccessible to Li-ions [112] and therefore no plateaus are observed with $LiPF_6$ EC:DMC (1:1) electrolyte. A moderate capacity of 180 mAh g^{-1} at 1.0 V vs Li/Li^+ is obtained. From a full cell perspective, such performance is disadvantageous, as the sloping potential would dramatically reduce the cell's energy density. Furthermore, the 1st cycle coulombic efficiency (CE) is only 65%, implying high irreversible capacity, often attributed to high electrolyte consumption by SEI layer formation on carbons with a high specific surface area (SSA), in this case 238 m^2 g^{-1}, and high surface functional group content [132]. On the other hand, both Na-based electrolyte containing half cells exhibit plateaus at $E < 0.2$ V vs Na/Na^+ and a sloping region at $0.2 < E < 1.0$ V vs Na/Na^+. Compared to $NaPF_6$ EC:DMC, $NaClO_4$ PC electrolyte produces superior cell performance in all aspects – higher cumulative discharge capacity (204 vs 139 mAh g^{-1}), higher plateau capacity at $E < 200$ mV vs Na/Na^+ (109 vs 63 mAh g^{-1}) and higher CE (90% vs 85%).

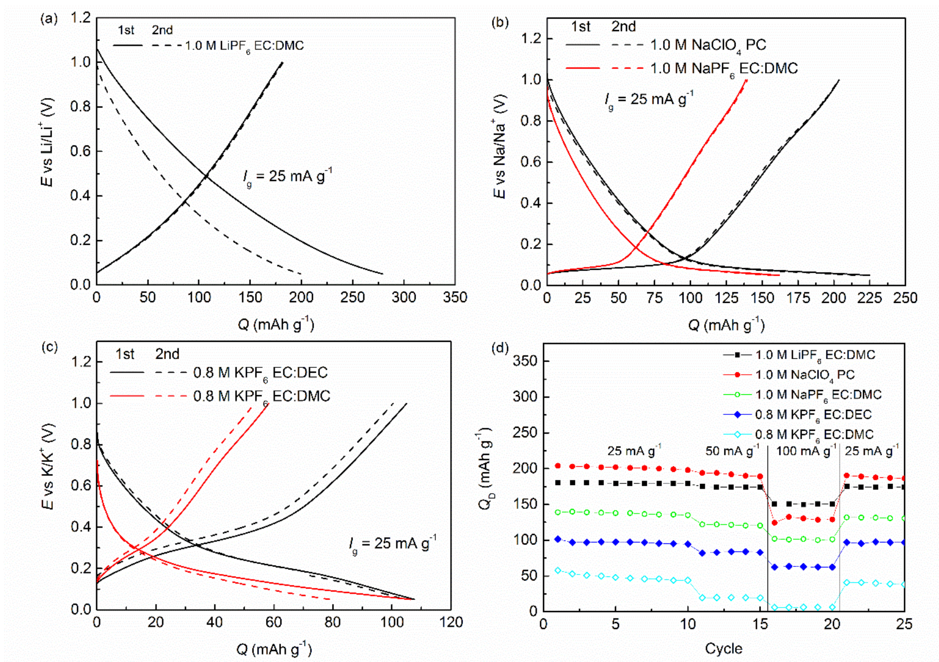

Figure 21. GCD profiles of Li^+ (a), Na^+ (b), K^+ (c) based half cells and a comparison of discharge capacities at different current densities (d).

As indicated by CVs, K^+-based half cells show very different electrochemical performance compared to Li^+ and Na^+ cells (**Figure 21c**). Charge/discharge curves have a sloping profile, high potential hysteresis between charge and discharge plateaus can be observed and the resulting discharge capacity values are much lower, 105 and 58 mAh g^{-1}, for DEC and DMC based electrolyte, respectively. When comparing the charge profiles of both K-based half cells, DMC requires lower potentials for the intercalation process to happen than does DMC. The high irreversibility of DMC-based electrolyte implies K trapping into the electrode structure. A 77 mV ohmic-drop can be observed between charging to discharging mode, unlike with Li^+- and Na^+-cells, where such potential drops are barely noticeable. Half cell cycling and rate performance was evaluated at current densities from 25 mA g^{-1} to 100 mA g^{-1} (**Figure 21d**). The specific capacity values from the first 25 discharge cycles (**Figure 21d**) were highest for GDHC 1100|1.0 M $NaClO_4$ PC|Na half cell with an exception of 100 mA g^{-1}, where $LiPF_6$ EC:DMC showed the best rate performance.

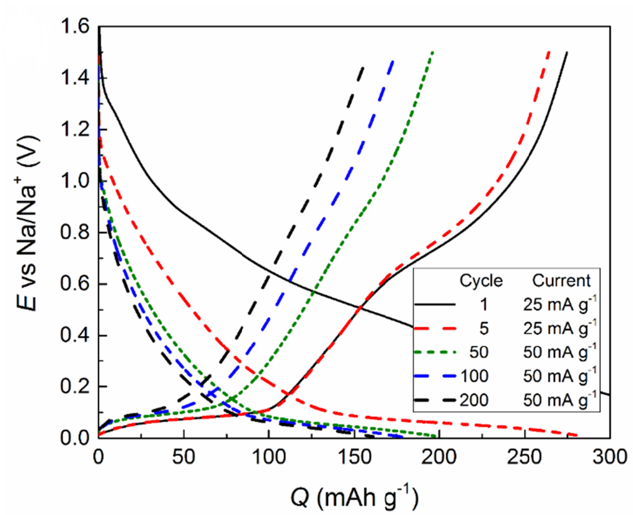

Figure 22. Galvanostatic charge-discharge profiles at different cycles [I].

Longer cycling tests were carried out with 1 M $NaClO_4$ PC containing cells as it had showed the best results in previous experiments. **Figure 22** shows GCD profiles at different cycles and highlights a major problem with GDHC 1100 – the massive irreversible capacity during the first cycle. In a full cell that would consume too many Na-ions from the electrolyte and the remaining reversible capacity would be very low. Capacity fade is apparent as the cycle number increases and is mostly caused by losses in the plateau region. A slight decrease in slope at $0.6 < E < 1.0$ V on discharge curves, which are not visible during charge can be observed at lower currents (25 mA g^{-1}). This could be due to a 2-

stage de-intercalation reaction from the exfoliated graphene sheets and basal planes of graphitic domains. The extent of capacity fade is apparent in **Figure 23** (left), where capacity drops from 300 mAh g^{-1} to 160 mAh g^{-1} by the 200th cycle. A probable reason is that co-intercalation of PC causes exfoliation [22] and an increase in electrical series resistance due to formation of electrically insulated active material particles. Moreover, extensive electrolyte decomposition can proceed, as PC does not form a stable SEI [8]. However, cycle life is massively improved (255 mAh g^{-1} at 200th cycle) by adding 10 vol% of EC to the electrolyte solution (**Figure 23b**).

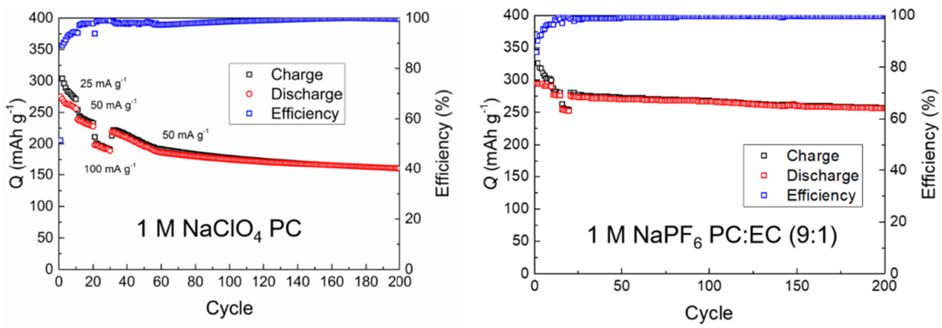

Figure 23. GCD cycling data from GDHC 1100||Na half cells in different electrolytes.

Apparently, the electrolyte plays a crucial role in active material performance, which is why different PC-based electrolytes were studied in LIB and NIB half cells [III]. It is clear from **Figure 24** that $NaPF_6$ and $NaClO_4$ show similar behavior in PC, but more pronounced differences can be observed with EC:PC (1:1) mixture. However, the choice of salt anion becomes even more critical in Li-based cells, where $LiClO_4$ is clearly underperforming – high *IR*-drop and no plateaus. Again, the difference between $LiPF_6$ and $NaPF_6$ can be witnessed when comparing EC:PC (1:1) electrolytes. The profiles of $LiPF_6$ have a longer and smoother sloping region, while $NaPF_6$ has well defined sloping and plateau regions. Although $LiPF_6$ achieves higher capacity values at 1.5 V vs Li/Li^+, the plateau capacity is 75 mAh g^{-1} higher with $NaPF_6$. It can be inferred that PC is crucial to micropore filling as the plateau regions were either short or absent in **Figure 21**, where EC:DMC (1:1) solvent mixture was used.

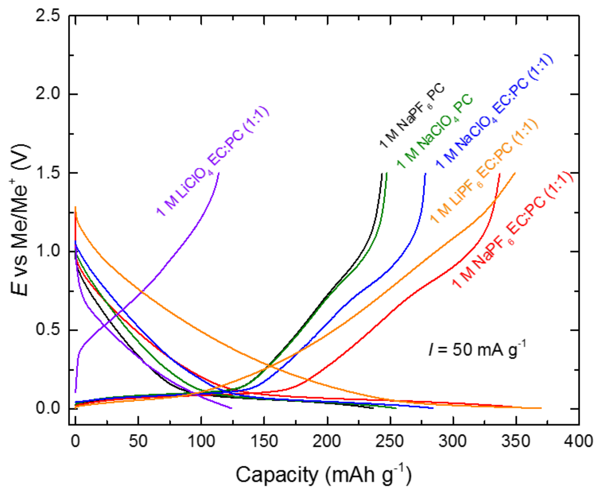

Figure 24. GCD profiles of half cells with various PC-based electrolytes.

GCD profiles recorded at different current densities for $LiPF_6$ EC:PC (1:1) in **Figure 25** show the half cell has high power characteristics (175 mAh g^{-1} at 2000 mA g^{-1}), but not as much capacity for high energy as the plateau region is fairly short and absent at $I > 200$ mA g^{-1}. The half cell has a high irreversible capacity on the first cycle indicating that a lot of Li that is inserted in the material can not be extracted reversibly.

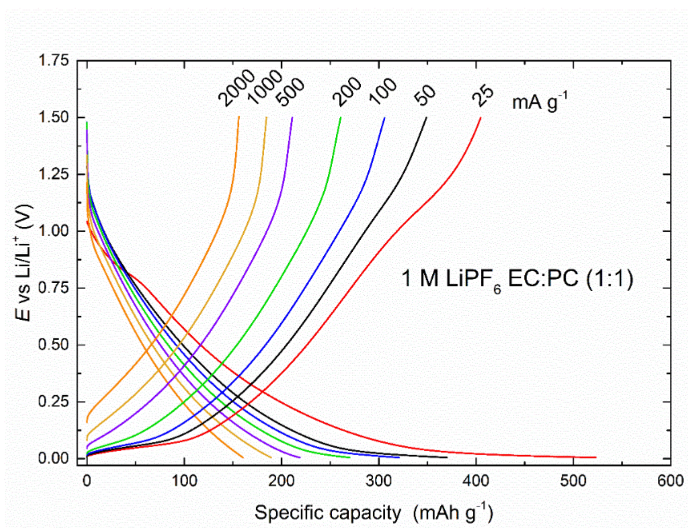

Figure 25. GCD profiles of GDHC 1100||Li half cells with $LiPF_6$ EC:PC (1:1) electrolyte.

GCD profiles of Na-based half cells recorded at different current densities in **Figure 26** have well developed plateaus reaching 175 mAh g^{-1} with $NaPF_6$ EC:PC (1:1) electrolyte. Adsorption in the micropores and subsequent metallic cluster formation attributed to the plateau region is a much slower process than insertion between layers since the plateau region becomes virtually nonexistent in all cells at $I > 300$ mA g^{-1}.

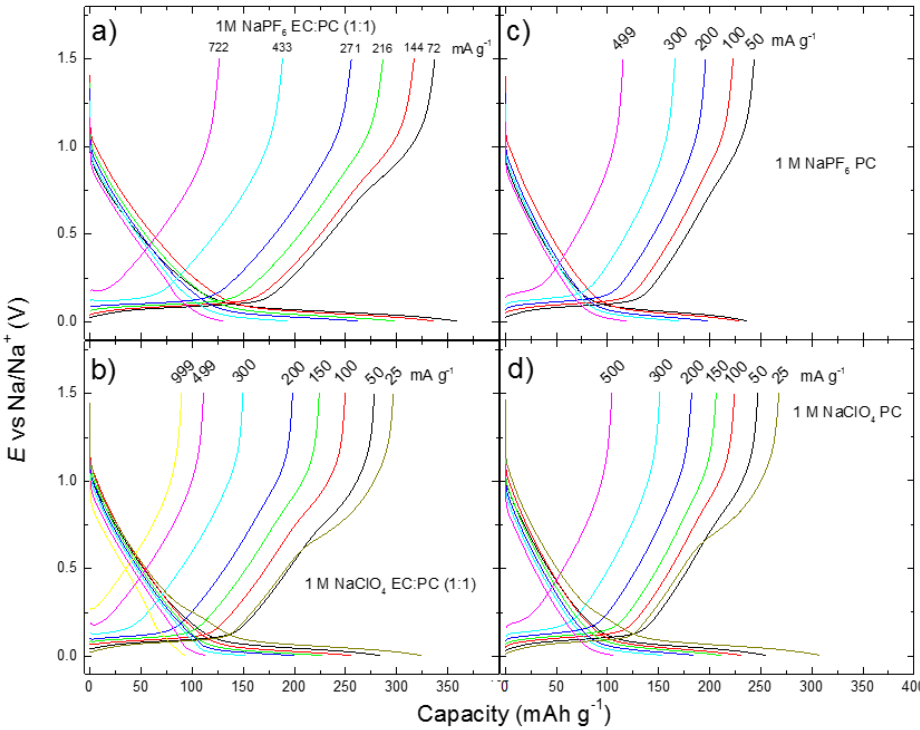

Figure 26. GCD profiles of different Na^+-based electrolytes at various current densities.

6.3.1 GDHC 1400–1600

The literature on hard carbons indicated that higher HTTs produce materials with better Na-storage properties and secondly our first GDHC1100|| NVP full cells showed massive losses on the first charge cycle, which is why higher temperatures were used to treat the HTC precursor.

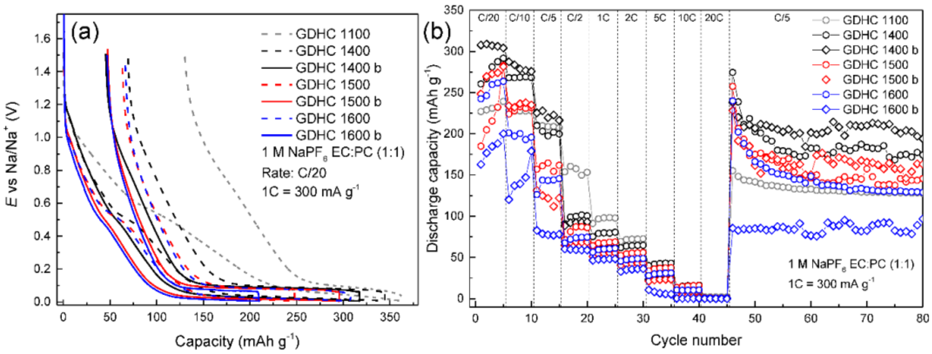

Figure 27. GCD half cell data for GDHCs heat treated at higher temperatures. Galvanostatic profiles of the first cycle for GDHCs noted in figure (a) and cycling data of GDHCs at various C-rates.

It is evident from **Figure 27a** why GDHC 1100 is impractical in a full cell – the first charge consumes 200 mAh g^{-1} before reaching the plateau region. The charge/discharge profiles in **Figure 27a** follow a logical order – with increasing temperature, both irreversible capacity and sloping area are reduced. However, plateau capacities also reduce which lowers 1st cycle coulombic efficiency (CE). By limiting the Super P in all electrodes, irreversible capacity is reduced from 66 mAh g^{-1} to 47 mAh g^{-1} and sloping region reduced by 30 mAh g^{-1}. Unfortunately, the plateau capacity is also reduced when Super P content is decreased from 15 wt% to 4 wt%, which could have been caused by reduced conduction paths in the composite electrode [133]. As shown in **Figure 27b**, the best overall performance is achieved with GDHC 1400 b (reduced Super P content). Higher plateau capacity, but similar irreversible capacity compared to higher temperatures yields a 1st cycle CE of 85%. Therefore, this carbon was chosen as the best candidate for further full cell measurements.

6.3.2 $Na_3V_2(PO_4)_3$ positive electrode

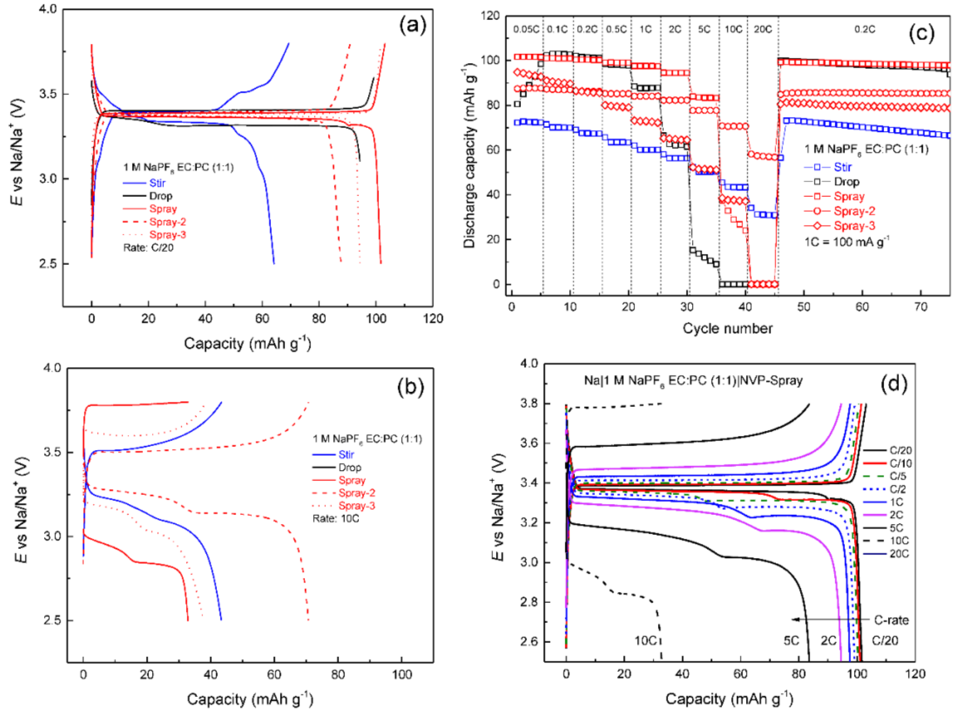

Figure 28. GCD half cell data for the studied NVP materials. Comparison of galvanostatic profiles of the tested active materials at C/20 (a), at 10C (b), cycling data at various C-rates (c) and galvanostatic profiles at different currents for NVP-Spray half cell (d).

Data in **Figure 28a** indicate that NVP-stir has staging charge profile and a lower capacity (64 mAh g^{-1}), which is in good agreement with XRD data. Multiple impurities that could not be identified are present and will therefore lower the gravimetric capacity of the material. All the other materials display very flat plateaus, some staging during discharge can be observed, explained by parasitic oxidation reactions on the surface of the sodium counter electrode [134]. NVP-Spray displays the highest capacity – 102 mAh g^{-1} at C/20, followed by NVP-drop and NVP-Spray-3 (scaled up version of NVP-Spray, but without added glucose) at 94 mAh g^{-1} and NVP-Spray-2 at 88 mAh g^{-1}. However, the order reverses at 10C (**Figure 28b**), where NVP-Spray-2 exhibits the best performance (70 mAh g^{-1}) and NVP-Drop the worst reaching the cut-off voltage too early due to high *IR*-drop. The fact that NVP-Spray-3 and NVP-Spray-2 show high capacities at 10C rates can be attributed to increased carbon content in the electrode material. Firstly, 25 wt% of glucose was added to NVP-Spray-2 precursor, which helps to form a carbon shell around the particles and therefore increases conductivity of the material [116,135]. Secondly, some scaling effects seem to contribute to NVP-Spray-3 having a higher capacity at 10C than NVP-Spray, even though no additional glucose was added to the precursor before the heat treatment step. This means that with larger quantities more organic material is left in the precursor matrix during precursor formation. Unfortunately, an amorphous mixture of Na^+, V^{3+} and PO_4^{3-} ions makes a too aggressive sample for thermogravimetric analysis (TGA) that can contaminate the thermocouple when Na^+ diffuses through alumina, which is why TGA was not performed with NVP samples. Looking at the overall performance of all cells (**Figure 28c**), NVP-Spray and NVP-Drop show superior performance at low rates (even after recovery from high rate cycling (0.2C)). NVP-Spray demonstrates the highest capacities up to 5C. Spray-2 shows the best high-power performance (60 mAh g^{-1}) at 20C. NVP-Drop and NVP-Stir are the only samples, which show a faster fade at 0.2C after high rate cycling.

NVP-drop shows high capacity at low currents, but a rapid decline ensues as currents exceed 2C. This can be explained by bigger crystal size that lengthens path of diffusion for Na ions. NVP-spray is an improvement to NVP-drop by enabling higher C-rates and when scaled up (Spray-2), it shows power characteristics that far exceed even NVP-Stir, which initially seemed like the best candidate for a high-power NIB cell. **Figure 28d** shows charge profiles of NVP-Spray various C-rates. It can be seen, that after 2C a drastic increase in ohmic drop is evident and capacity starts to decline. Interestingly, these stages are visible only in discharge profiles and become more pronounced as the applied current increases. As mentioned before, this can be due to parasitic reactions on the Na counter electrode [134], but has to be examined further as such phenomena have not been observed in other works [32,116] or profiles are not shown [136].

6.3.3 GDHC 1400 b||NVP-Spray full cell measurements

Full NIB cells were assembled using NVP-Spray as the positive electrode and GDHC 1400 b as the negative electrode to evaluate NVP-Spray performance in a full cell. **Figure 29a** shows 1st charge/discharge profile for two cells with different Q_N/Q_P ratios; Q_N – negative electrode capacity; Q_P – positive electrode capacity. Cell 1 has a Q_N/Q_P ratio of 1.1, which means the negative electrode is slightly oversized and therefore prevents Na plating on the hard carbon due to overcharge. This is common practice for commercial cells to increase safety [137,138]. Cell 2 Q_N/Q_P is 0.75, which means NVP is in large excess. Cell 3 with GDHC 1100 with Q_N/Q_P at 0.37 is shown for comparison to illustrate the effect high sloping region capacity has on full cell performance. Data in **Figure 29a** show that although cells 1 and 2 have a similar CE during the first cycle, the slight increase of cell potential at 90 mAh g^{-1} during charge is evidence that Na plating has taken place in Cell 2. **Figure 29b** demonstrates the effect of misbalancing to overall cell performance: Cell 1 and 2 start from similar capacity values, but Cell 2 declines rapidly, as dendritic plating of Na increases surface area and in turn leads to further electrolyte decomposition and loss of

Na^+. Cell 1 is very stable with CE of 99.7% at 80th cycle. Charge/discharge profiles in **Figure 30** are comprised of two distinct regions and the graph shape is mainly determined by the hard carbon profile since NVP has a very flat plateau. As the plateau capacity of the hard carbon is depleted the full cell profile follows the sloping behavior of the hard carbon. Capacities for Cell 1 reach 80 mAh g^{-1} and 60 mAh g^{-1} for the plateau region per NVP active mass. Calculated energy density for the full cell at C/20 was 104 Wh dm^{-3} and specific energy 189 Wh kg^{-1}. Cell 1 rate performance (**Figure 29b**) is similar to NVP-Spray in **Figure 29b** – capacity decline after 2C with increased ohmic drop, which in turn caused specific energy drop from 150 Wh kg^{-1} (at 2C) to 119 Wh kg^{-1} (at 5C) and energy density drop from 82 Wh dm^{-3} (at 2C) to 65 Wh dm^{-3} (at 5C). Interestingly, no stages can be observed in discharge profiles unlike in NVP half cells, which again supports the claim that reactions on Na electrode can distort the signal that is assumed to come from the working electrode [134].

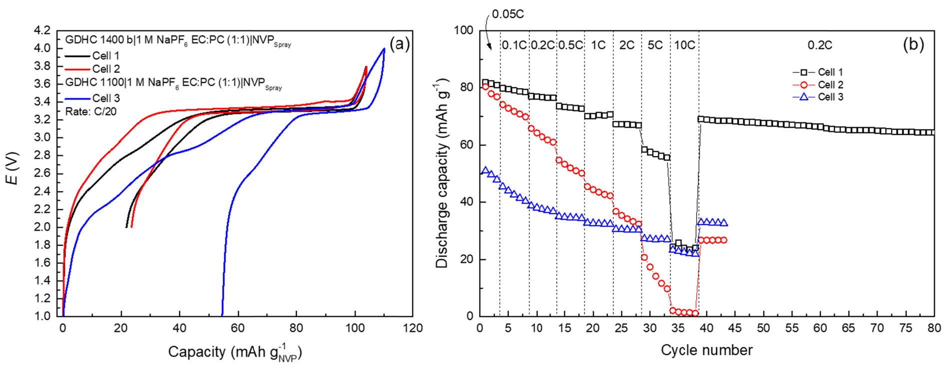

Figure 29. Galvanostatic charge/discharge data for GDHC full cells; (a) profiles of the first charge/discharge cycle for GDHC||NVP full cells and (b) discharge capacities for full cells at various cycling rates (noted in figure).

Full cell results show how important it is to optimize the hard carbon electrode material towards a reduced surface area to reduce Na^+ loss and the need for oversizing positive electrode mass loading to compensate for that loss.

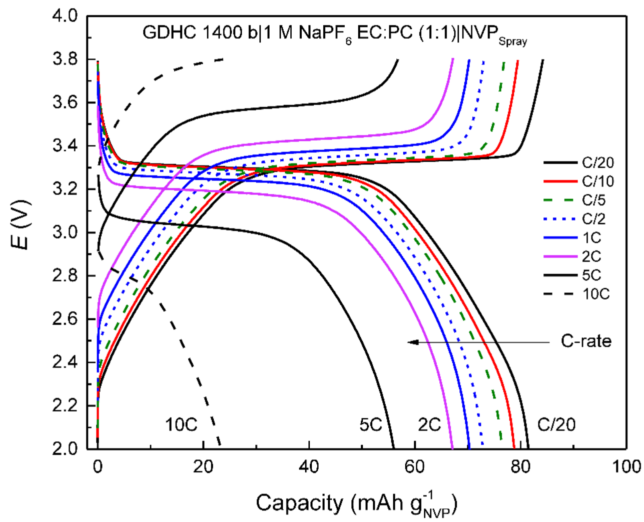

Figure 30. Galvanostatic charge-discharge profiles for Cell 1 at various C-rates (noted in figure).

6.4 Analysis of electrochemical impedance spectroscopy (EIS) data

6.4.1 GDHC 1100 in 1 M $NaClO_4$ PC

EIS was employed to study the nature of hard carbon sodiation processes in more detail. Equivalent circuit fitting was applied to interpret the complex data using a modification of an equivalent circuit (EQC) developed by J. Newman's group [139] in **Figure 31a** and three Nyquist plots are shown to illustrate the difference of recorded impedance signals at various electrode potentials.

The impedance spectra within electrode potential region $0.2 \leq E \leq 1.2$ V vs Na/Na^+ showed two depressed semicircles (in **Figure 31** only some are shown for shortness), followed by a nearly linear slope region, i.e. so-called finite length (capacitive) or mass transfer region (depending on the E applied). However, at some potentials ($E = 0.05$ V vs Na/Na^+) the second semicircle has been screened by Warburg-like finite-length mass-transfer impedance behavior, possibly indicating diffusion of partially solvated Na^+ in the micro-/nanoporous electrode matrix. At $E = 1.45$ V vs Na/Na^+ the second semicircle is screened by finite-length adsorption effects, which indicates that only adsorption processes take place at such potentials. Indeed, as shown by the GCD plot in **Figure 21b**, noticeable charge storage starts at $E < 1.0$ V vs Na/Na^+. At higher ac frequencies, ~600 kHz to 20 Hz, there is a well expressed, but slightly depressed semicircle in the Nyquist plot, a characteristic of the SEI layer formation onto/into the GDHC|electrolyte interface with a resistance (R_{SEI}) and capacitance (C_{SEI}). The second depressed semicircle at middle frequencies (from 20 Hz to 0.1 Hz) can be ascribed to faradaic processes (depending on the potential applied) [140,141] and characterized by faradaic charge transfer resistance (R_{ct}) and charge transfer process capacitance (C_{ct}) values. A nearly linear region in Nyquist plots is normally related to the Warburg-like impedance behavior due to Na^+ ion diffusion in solids or into the microporous carbon electrode structure [142].

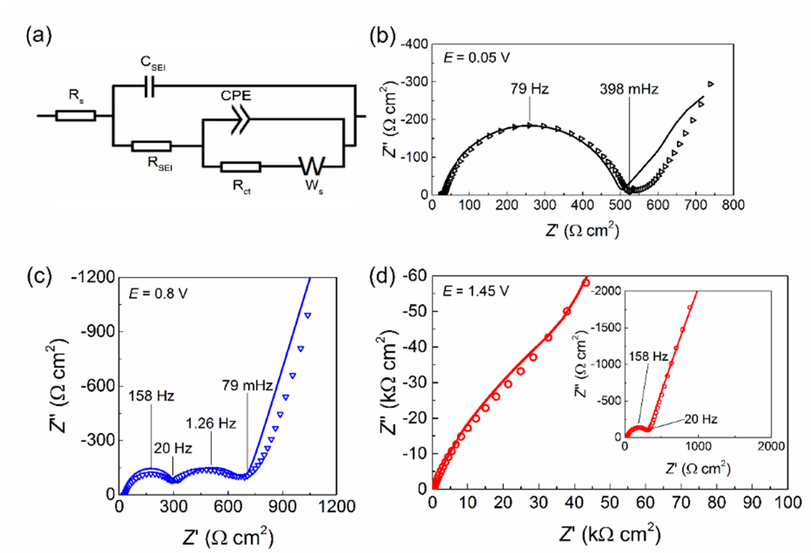

Figure 31. EQC used for fitting EIS data (a), EIS data recorded at 0.05 V (b), 0.8 V (c) and 1.45 V (d) vs Na/Na^+ for GDHC 1100||Na half cells with 1 M $NaClO_4$ PC electrolyte. Knee-frequencies and semi-circle maxima frequencies noted in the figure. EQC fitting results shown as a solid line.

Results of non-linear regression analysis show that experimental Nyquist plots can be simulated with high accuracy and with chi-square values of $\chi^2 \geq 5 \times 10^{-4}$ and $\Delta^2 \geq 0.08$. The measured series resistance (R_s) values (**Figure 32a**) for the GDHC 1100||Na half cell depend on the applied electrode potential. The highest R_s values can be seen at $E = 1.872$ V (open circuit potential vs Na/Na^+) thus, in the so-called electrical double layer charging/discharging region. Therefore, in this electrode potential region, there are no faradaic reactions and only at $E <$ 1.0 V vs Na/Na^+ the SEI layer formation starts. The values of SEI film capacitance (C_{SEI}) and resistance (R_{SEI}) (**Figure 32b**) can be explained by the SEI formation at/into the carbon material or by the pseudometallic characteristics of microporous carbon material, discussed previously in Refs. [143,144]. According to data in **Figure 32a**, the high frequency series resistance R_s values depend weakly on the E applied. However, R_{SEI} values (from 0.2 to 290 Ω cm^2) depend somewhat on the applied electrode potential and are higher at E from

0.6 to 1.872 V (OCP) vs Na/Na^+ (**Figure 32b**). A considerable decrease in R_{SEI} is observed for all systems at $E < 0.8$ V, where Na^+ ion adsorption (accumulation) with partial charge transfer starts. At $E > 0.6$ V, an increase in R_{SEI} is associated with the insulating SEI layer formation on the electrode surface. SEI film capacitance (C_{SEI}) values (**Figure 32b**) are moderate (from 0.1 to 0.3 μF cm^{-2}), but a pronounced decrease in C_{SEI} occurs at $E < 0.8$ V vs Na/Na^+, where partial charge transfer processes, attributed to Na^+ intercalation between expanded graphene layers start. R_{ct} values (**Figure 32c**) are very high at $E >$ 1.45 V vs Na/Na^+, within the so-called electric-double layer region. At $E < 1.45$ V, a substantial decrease in R_{ct} values takes place which, can be explained with the adsorption of Na^+ ions on the electrode surface, SEI formation onto/into GDHC electrode structure and intercalation and accumulation of Na in the material. At $E < 1.0$ V vs Na/Na^+, the diffusion resistance (R_D) values (**Figure 32d**) are noticeably higher than R_{ct} values, and the increase in R_D values at $E <$ 0.2 V (vs Na/Na^+) is mainly caused by SEI formation. At $E \geq 1.5$ V, the R_D values are moderate compared to R_{ct} values, which demonstrates that at $E > 1.5$ V no faradaic or partial charge transfer processes take place at the GDHC electrode surface, as the electrode surface has been depleted of electrochemically active Na.

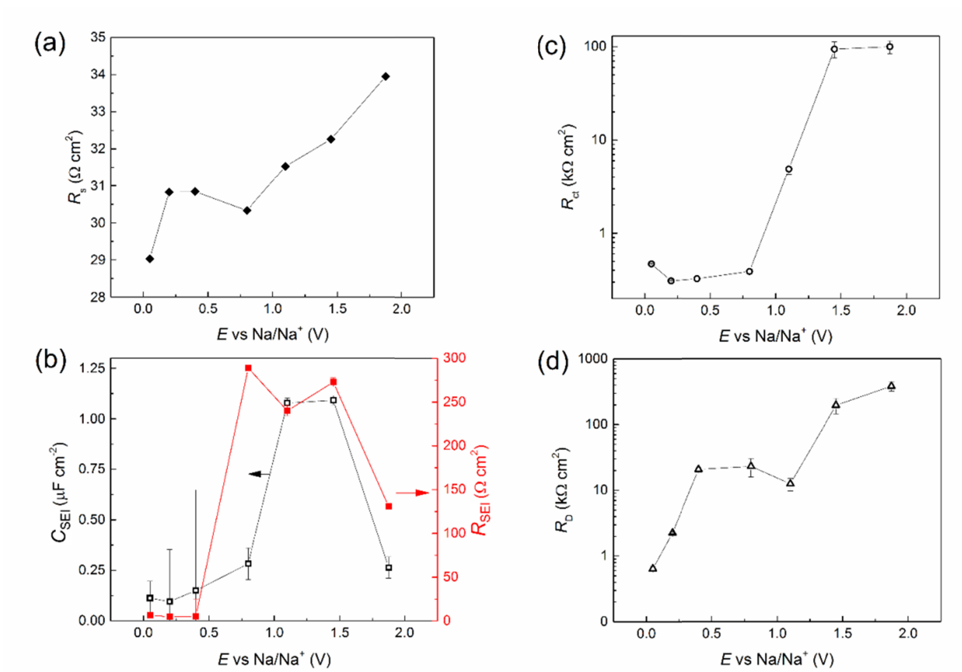

Figure 32. Equivalent circuit element parameters retrieved by fitting the recorded EIS spectra as a function of bias potential.

6.4.2 EIS study of alkali metal insertion processes on hard carbon

The results described above inspired us to study the insertion and accumulation processes with Li and K electrolytes as well to gain better understanding of charge storage mechanisms between the different alkali metals as noted in Section 6.3. The idea was to conduct numerous impedance measurements in a wide potential range and gain insight into the nature of the charge storage processes with the help of statistics and data analysis. Similar concept has been applied previously to study SEI formation on graphite negative electrodes in LIBs [145,146], on $LiNiO_2$ positive electrode surface [147] and for evaluating LIB cell performance at low temperatures [148]. In order to study the small changes in the process characteristics as the electrode is charged and discharged, impedance spectra were recorded in small intervals – every 200 mV in $0.4 < E < 0.8$ V vs Me/Me^+ (Me – Li, Na, K) potential range and every 12.5 mV in $0.04 < E < 0.4$ V vs Me/Me^+ potential range. Four different half cells were tested, 3 charge-discharge cycles were conducted for each cell and each cycle produced 34 EIS spectra, i.e. the total number of spectra produced was 408. Only the first cycle of each half cell was analyzed in detail for practical reasons. However, before embarking on a massive batch fitting operation, different EQCs had to be considered.

6.4.2.1 Choice of equivalent circuits

Multiple equivalent circuits (EQCs) were tested for fitting the impedance data of the half cells, but the three best ones (**Figure 33**) were selected for comparison (**Figure 34** and **Table VIII**) to determine the one most applicable for the measured EIS data. An EQC by Zhang et al. [145,148] (**Figure 33c**), which has been used to evaluate bulk or series resistance (R_s), solid electrolyte interface resistance (R_{SEI}) and charge-transfer resistance (R_{ct}) values in LIB cells was also considered. Also, an EQC developed by Newman and Meyers et al. [139] (**Figure 33b**), proved to model the real physical processes in model porous intercalation electrodes was evaluated. Since the Meyers et al. model fits impedance data at frequencies only above 0.05 Hz, it has been slightly modified (hereafter named modified Newman circuit) by replacing the double-layer capacitance with a constant phase element (CPE) [143,144]. The CPE is better suited for analysis of double layer formation/relaxation at porous energetically heterogeneous carbon surface consisting of graphitic sp^2 and amorphous sp^3 areas. In the modified Newman EQC (**Figure 33a**), R_s is the high-frequency resistance of the half cell, which corresponds to the total resistance of the electrolyte, separator and electrodes; R_{SEI} and C_{SEI} are the resistance and capacitance of the SEI, which correspond to the semicircle at high frequencies. R_{ct} and CPE are charge transfer resistance and distributed double layer capacitance/resistance expressed as a constant phase element, which corresponds to the semicircle at medium frequencies. Finite-length Warburg impedance (Z_{Ws}) is related to an effect of the diffusion of Li^+, Na^+ or K^+ ions in/on the porous electrode electrolyte interfaces.

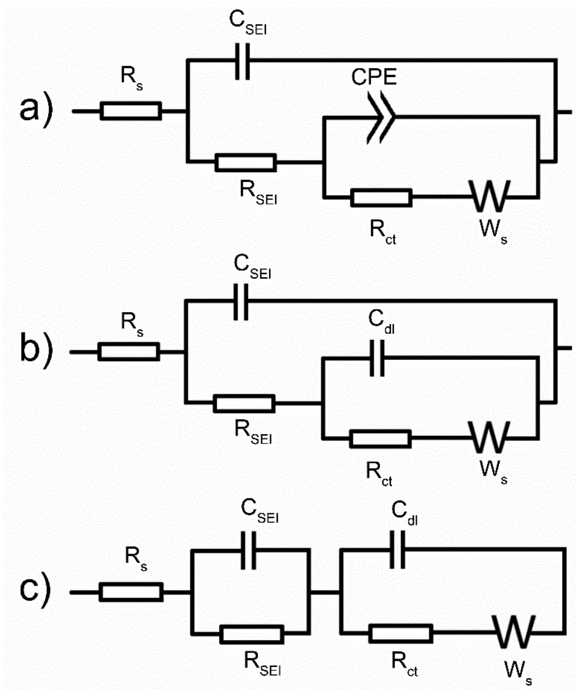

Figure 33. EQCs used for fitting impedance data in this work: modified Newman circuit (a), where C_{dl} has been replaced with a constant phase element (CPE), original Meyers and Newman (b) circuit from Ref. [139] and circuit used by Zhang et al. (c) for fitting impedance data in Refs. [145,148].

6.4.2.2 Batch fitting of spectra

EQCs shown in **Figure 33** were considered for batch fitting EIS data in [II]. A comparison of fits is shown in **Figure 34** and fitting parameters with errors are shown in **Table VI**.

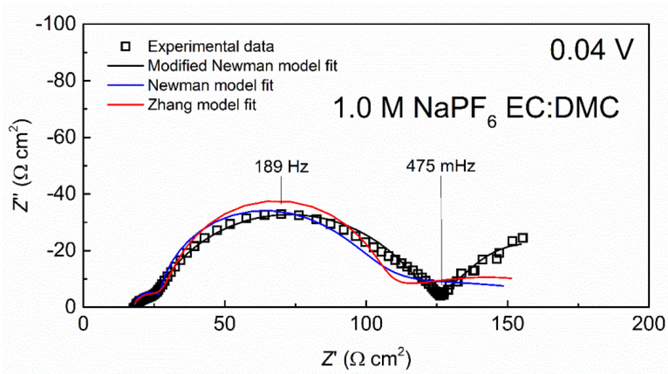

Figure 34. Comparison of equivalent circuit fits of EIS spectrum recorded at 0.04 V vs Na/Na^+ in 1.0 M $NaPF_6$ EC:DMC (1:1).

The fitting best fitting results (smaller χ^2 and error % in **Table VIII**) for 1.0 M $NaPF_6$ EC:DMC (1:1) system were achieved using the CPE modified Newman EQC. Therefore, only modified Newman circuit was used for fitting the rest of the impedance data in this study. Also, using the EQC given in **Figure 33a** enables better comparison with our previous data on Li^+, Na^+, Cs^+ cation based electrolyte and carbide-derived carbon (CDC) interface [144,149,150]. For more detailed analysis of the measured impedance spectra used for fitting, consult Paper [II].

Table VIII. Comparison of fitting parameters of three equivalent circuits for 1.0 M $NaPF_6$ EC:DMC (1:1) half cell at 0.04 V vs Na/Na^+ [II].

Circuit	Parameter	Value	Error	Unit	Error %
Modified Newman	χ^2	0.0012			
	Δ^2	0.171			
	R_s	18		Ω cm^2	
	C_{SEI}	0.31	0.01	μF cm^{-2}	3.72
	R_{SEI}	6.36	0.16	Ω cm^2	2.48
	A	59.0	2.3	μF $s^{\alpha-1}$ cm^{-2}	3.96
	α_{CPE}	0.740	0.005		0.69
	R_D	63.3	6.8	Ω cm^2	10.70
	τ_{Ws}	45.27	11.23		24.80
	α_{Ws}	0.45	0.02		4.21
	R_{ct}	97.21	0.70	Ω cm^2	0.72
Newman	χ^2	0.0117			
	Δ^2	1.674			
	R_s	18		Ω cm^2	
	C_{SEI}	0.49	0.03	μF cm^{-2}	6.37
	R_{SEI}	10.27	0.37	Ω cm^2	3.62
	C_{dl}	6.83	0.22	μF cm^{-2}	3.32
	R_D	163.4	22.47	Ω cm^2	13.75
	τ_{Ws}	36.07	104.04		288.44
	α_{Ws}	0.08	0.01		15.50
	R_{ct}	8.80×10^{-6}	7.51	Ω cm^2	8.54×10^7
Zhang	χ^2	0.0101			
	Δ^2	1.458			
	R_s	18		Ω cm^2	
	C_{SEI}	10.80	0.32	μF cm^{-2}	3.039
	R_{SEI}	66.87	1.47	Ω cm^2	2.19
	C_{dl}	0.39	0.03	μF cm^{-2}	8.74
	R_D	102.3	13.86	Ω cm^2	13.55
	τ_{Ws}	99.15	133.44		134.58
	α_W	0.152	0.006		4.060
	R_{ct}	1.72×10^{-7}	0.22388	Ω cm^2	1.30×10^8

The fitting results of the recorded impedance spectra are shown in **Figure 35−Figure 40**. Each point on the graph corresponds to an EIS spectrum measured at a fixed potential. Charging corresponds to lithiation/sodiation/potassiation and discharging to the opposite process.

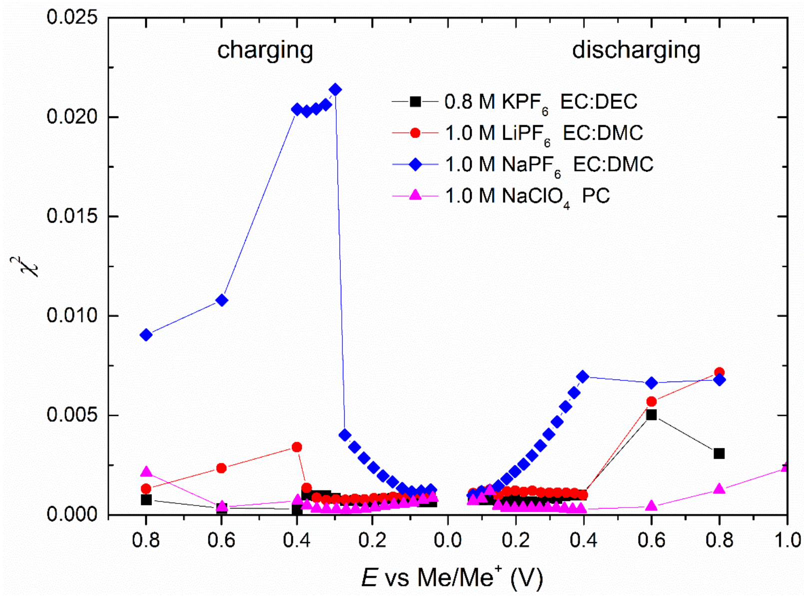

Figure 35. Chi-square values of modified Newman EQC fitting.

The results of non-linear regression analysis show that experimental Nyquist plots for all systems can be simulated with the modified Newman model with high accuracy, chi-square functions $\chi^2 \leq 5 \times 10^{-3}$ (**Figure 35**). The only exception being $NaPF_6$ based system, which shows χ^2 values above 0.01 at $E > 0.3$ V vs Na/Na^+.

It is clear from **Figure 36**, that $LiPF_6$ EC:DMC (1:1) electrolyte produces highest R_{SEI} values. It can be explained by the fact that smaller Li-ions with a higher charge density form stronger bonds with Li oxides (O_2 decomposition), hydroxides (H_2O decomposition) and carbonates, and therefore makes those species insoluble in polar aprotic media [8]. Also, the surface of hard carbon contains more organic species in LIB half cell than in a NIB one [III], which leads to higher surface film resistance. KPF_6 EC:DEC (1:1) shows very little change during cycling, which means that there is no effective SEI build- up. All other electrolytes besides $LiPF_6$ converge at a similar value between 5 and 10 Ω cm^2. As for SEI layer capacitance in **Figure 37**, $LiPF_6$ is has the highest values which is in good agreement with R_{SEI} values – SEI formation consumes charge. However, $NaClO_4$ PC has relatively higher C_{SEI} values than R_{SEI} values, compared to $NaPF_6$ and KPF_6. This can be explained by PC co-intercalation or the formation of soluble decomposition products that do not thicken the SEI.

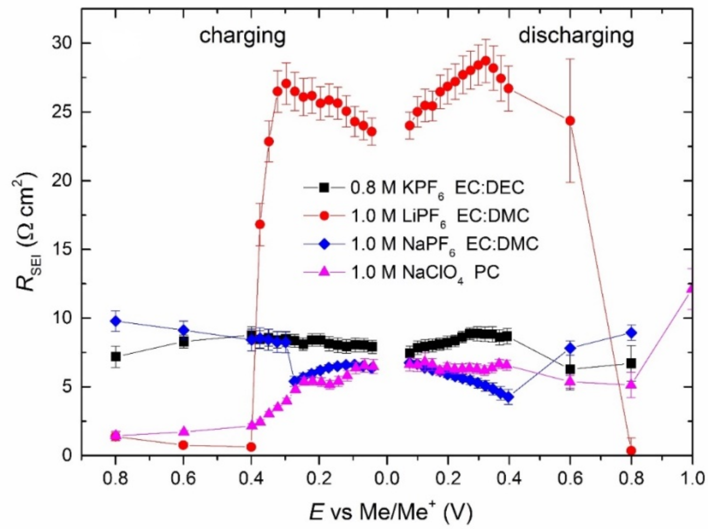

Figure 36. SEI layer resistance (R_{SEI}) values obtained through EQC fitting of spectra for the studied half cells.

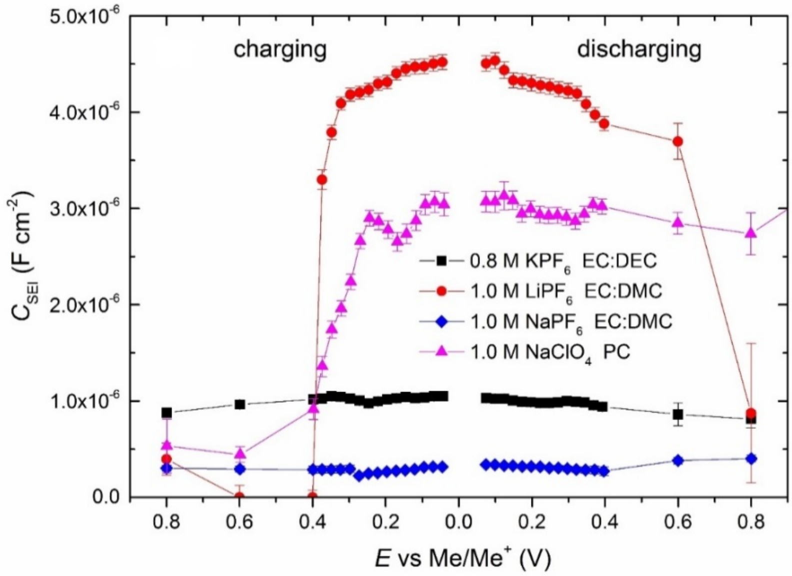

Figure 37. SEI layer capacitance (C_{SEI}) values obtained through EQC fitting of spectra for the studied half cells.

The constant phase element fractional exponent α_{CPE} values (**Figure 38**) for all systems, except $NaPF_6$ EC:DMC, are in the range of $0.70 < \alpha_{CPE} < 0.83$ indicating that a mixed adsorption step and mass-transfer step limited kinetics take place in the $0.4 < E < 0.04$ V vs Na/Na^+ region. At $E > 0.5$ V, for $NaPF_6$ EC:DMC system, $\alpha_{CPE} \rightarrow 1$ indicates that adsorption step rate limited processes are the prevailing in the system.

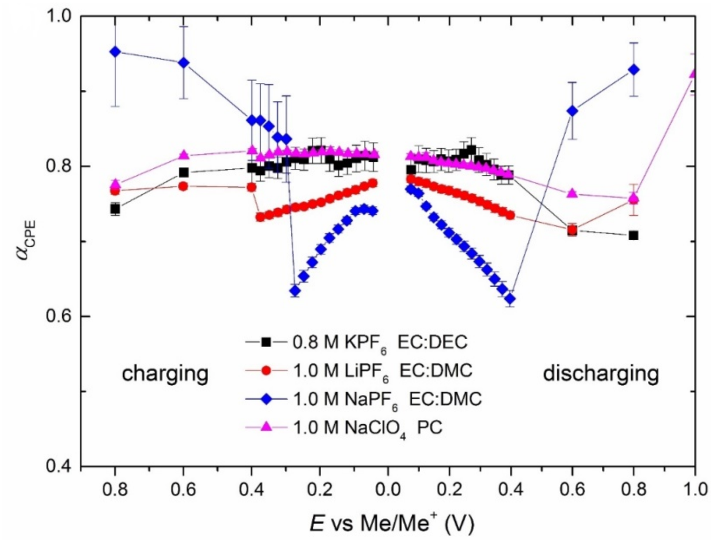

Figure 38. Constant phase element fractional exponent (α_{CPE}) values obtained through EQC fitting of spectra for the studied half cells.

The highest CPE constant (A) values have been calculated for the same system (**Figure 39**). All the other systems show very stable A values, independent of E. As expected, very low A values were obtained for KPF_6 EC:DEC electrolyte based half cells, as the CVs in **Figure 20c** showed lower electrochemical activity than Li- and Na-based counterparts.

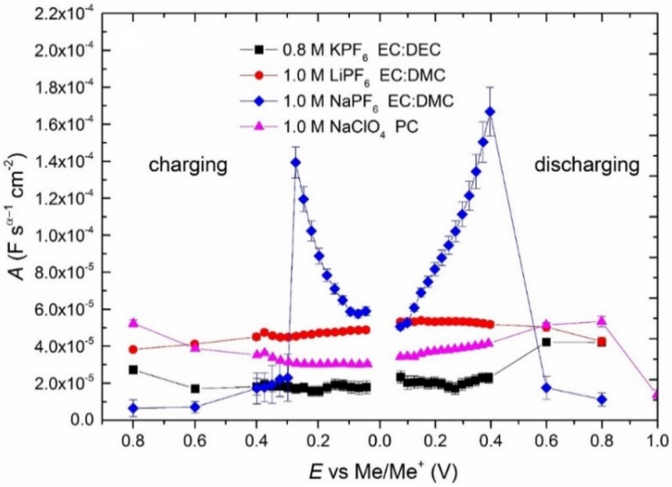

Figure 39. Constant phase element coefficient (A) values obtained through EQC fitting of spectra for the studied half cells.

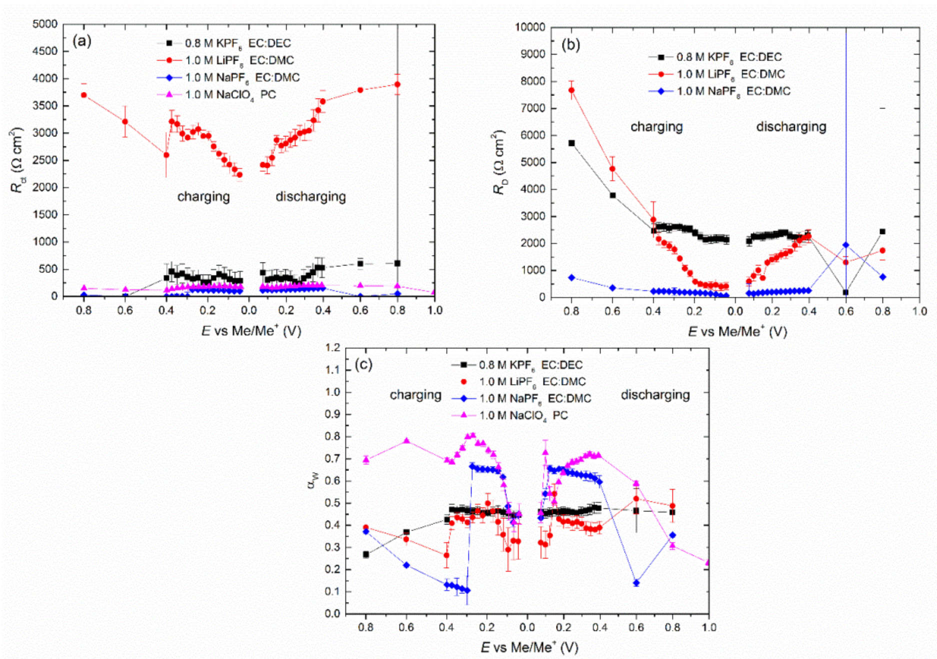

Figure 40. Charge transfer resistance (R_{ct}) (a), diffusion resistance (R_D) (b) and Warburg impedance fractional exponent (α_W) (c) values obtained through EQC fitting of spectra for the studied half cells.

Charge transfer resistance (R_{ct}) values (**Figure 40a**) are very high (2500–3500 Ω cm^2) for 1.0 M $LiPF_6$ EC:DMC (1:1) based system, which can be explained by the formation of thick passivating SEI on GDHC electrode surface. The R_{ct} values for Na^+- and K^+-based half cells, are relatively small (<500 Ω cm^2) compared to Li-based cell because the formation of resistive SEI layer on the GDHC|electrolyte interface is occurring to a smaller extent.

The diffusion resistance (R_D) values (**Figure 40b**) strongly depend on the applied E. The highest R_D values at E < 0.4 V were calculated for KPF_6 EC:DEC, but lowest for $LiPF_6$ EC:DMC and $NaPF_6$ EC:DMC system. Warburg-like diffusion impedance fractional exponent (α_W) values vary in great extent for 1.0 M $NaClO_4$ PC system, where the highest $\alpha_W \geq 0.8$ values have been calculated at E > 0.12 V. Surprisingly, for KPF_6 EC:DEC and $LiPF_6$ EC:DMC based systems $\alpha_W \approx 0.5$, which is a characteristic of semi-infinite diffusion process, have been calculated (**Figure 40c**). The very high R_D and $\alpha_W \geq 0.75$ values for KPF_6 EC:DEC electrolyte based system, calculated from impedance data, are in agreement with the shape of the CVs and GCD data, where very low current densities (very slow faradaic and mass-transfer processes) have been observed. The slower K^+ reduction and K oxidation/re-oxidation kinetics established by CV method (**Figure 20c**) are in agreement with impedance data. Low R_D values for $NaPF_6$ EC:DMC system indicate, that Na^+ diffusion in the electrode is less hindered that with Li^+ and K^+. This is also evidenced by the peaks in Na-based GCD data in **Figure 21b**.

6.5 Results of e*x situ* characterization of sodiated and lithiated electrodes

6.5.1 Raman spectroscopy

Comparison of the collected Raman spectra for the pristine GDHC 1100 composite electrode and the GDHC electrode charged with Li or Na (after the first galvanostatic charge cycle) show that one charge cycle with lithium or sodium has little effect on the structure of the disordered hard carbon material.

The intensity ratio of the D-band (1350 cm^{-1}, sp^3 carbon) and the G-band (1580 cm^{-1}, sp^2 hybridized carbon), (I_D/I_G), which can be used for the first approximation as a measure of the extent of graphite-like structure in the material, shows a small variation in I_D/I_G ratio increase for the material that accumulated Li or Na, which in turn indicates that slight increase in disordering of the GDHC carbon material has taken place. However, I_D/I_G ratio is not considered an accurate measure of disordering since D- and G-peaks usually consist of two separate peaks. A more precise way of comparing relative disordering is by calculating the full width at half maxima (FWHM) of G-peak by fitting Raman spectra with Gaussian and Lorentzian functions [151]. Therefore, FWHMs of the "real" G-peak are also shown in **Figure 41**, albeit the differences are minuscule [III].

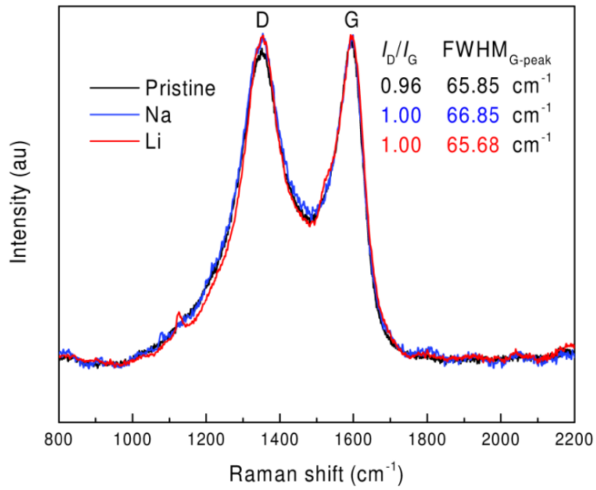

Figure 41. Raman spectra of pristine, sodiated and lithiated GDHC 1100 electrode [III].

6.5.2 LA-ICP-MS study of sodiated electrode

LA-ICP-MS was used to determine whether Na binds chemically to the hard carbon. In addition to the electrochemically cycled electrode (100 cycles within $0.005 < E < 1.5$ V vs Na/Na^+), dry and wetted electrode were analyzed to determine elemental contributions from the pristine electrode and from the electrode that has been in contact with the electrolyte (1 M $NaClO_4$ PC for 7 days), respectively. The sodiated and the wetted electrodes were washed with PC to remove salt residue deposits from the electrolyte.

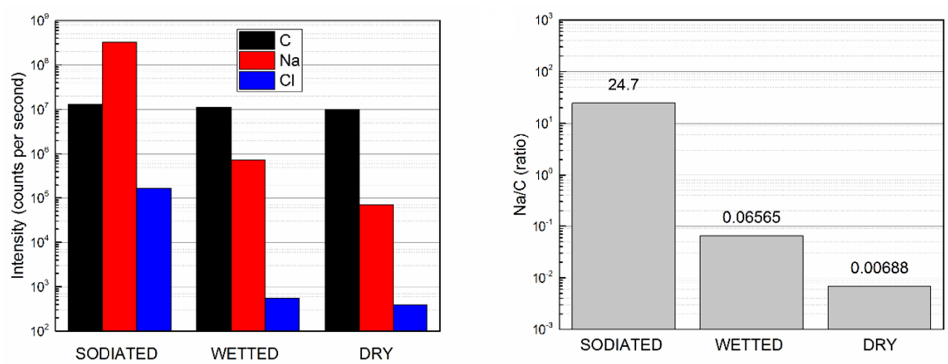

Figure 42. Left: LA-ICP-MS signal intensities for carbon, sodium and chlorine, corrected for baseline signal. Right: Na/C signal intensity ratio [I].

It can be concluded from **Figure 42** that electrochemically sodiated electrode contains far more Na and Cl than the wetted and dry electrode. It must be emphasized that the LA-ICP-MS method is less sensitive toward Cl than Na. Na/C ratio increases 375-fold after cycling and about 10-fold increase in Na can be seen after wetting the dry electrode. Therefore, it can be concluded that electrochemical polarization increases the accumulation of Na^+/Na^0 into the electrode porous structure.

6.5.3 TOF-SIMS investigation of sodiated and lithiated surfaces

Positive ion TOF-SIMS spectra were collected in the range up to 150 m/z. For shortness, the mass-spectra of the pristine, lithiated and sodiated electrodes are omitted, but shown in detail in [III]. The spectra in **Figure 43** show the difference between electrochemically charged electrodes and electrodes wetted with electrolyte (1 M $LiPF_6$ EC:PC (1:1) or 1 M $NaPF_6$ EC:PC (1:1) solution for 3 days). For the electrode charged in lithium-based electrolyte (**Figure 43** above), a number of fragment peaks were observed, mainly assigned to organic fragments, such as m/z = 43 ($C_2H_3O^+$), 59 ($C_2H_3O_2^+$) or $C_3H_7O^+$) and 77 ($C_2H_5O_3^+$) and with complexes with inorganics, for instance m/z = 33 (Li_2F^+) or ($C_2H_2Li^+$), 59 ($Li_3F_2^+$) or ($C_4H_4Li^+$) and 81 ($Li_3CO_3^+$). $C_2H_3O^+$ is considered a major component of the basal SEI [152]. In addition to the decomposition products generated by electrochemically induced oxidation/reduction processes, common contaminants such as m/z = 23 (Na^+) and 39 (K^+) and hydrocarbons were observed in the positive ion spectra.

Compared to Li spectrum, the sodium-based cell (**Figure 43** below) produced far less fragments. The fragments were assigned to inorganic components: m/z = 24 (NaH^+), 62 (Na_2O^+) and organic compounds: 39 ($C_3H_3^+$), 46 ($CH_2O_2^+$) and 69 (CF_3^+). This result proves that the surface film the sodiated electrode was more inorganic in nature and likely less polymerized. According to Aurbach and co-workers [8], of the surface species formed on the negative electrode of Li^+-based cells are less soluble than ones formed in the negative electrode of Na^+-based cells. These results confirm that the passivating layer is different at LIB and NIB hard carbon surface and it might be related to the different nature of Li and Na (or Li^+ and Na^+), such as ionic size, solvation energy of cations, solubility, reactivity etc.

Differences between TOF-SIMS ion spectra after the first galvanostatic cycle for electrodes from Li^+ and Na^+-electrolyte based half cells, respectively (**Figure 43**) indicate that charging accumulates almost 107 times more of Li or Na on the electrode surface. The SEI formation in the Li-based system produces a more complex layer that than the Na-based as indicated by the variety of fragments.

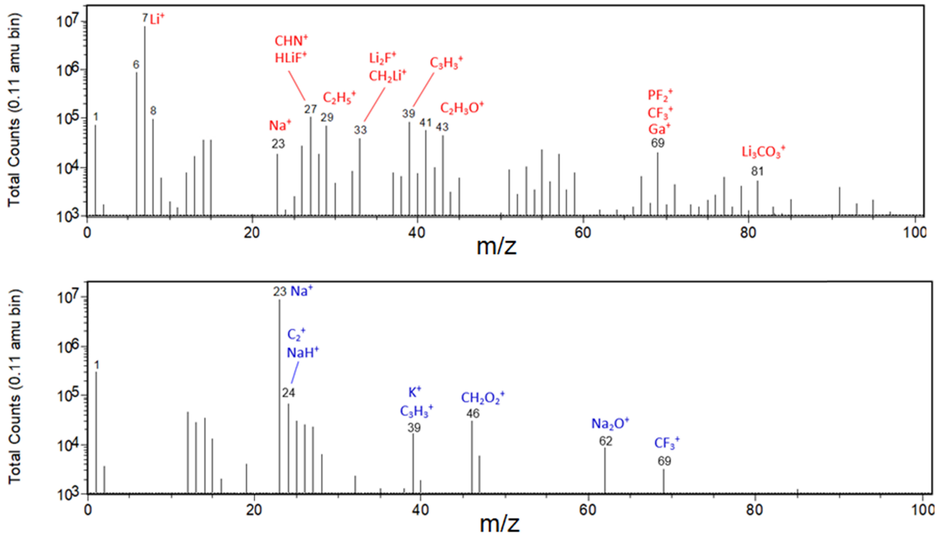

Figure 43. TOF-SIMS ion spectra of electrodes electrochemically charged with Li/Li^+ (above) and Na/Na^+ (below) from which spectra of non-polarized electrodes (wetted in either 1 M $LiPF_6$ EC:PC (1:1) or 1 M $NaPF_6$ EC:PC (1:1) electrolyte for 3 days) have been subtracted (adjusted for $^{12}C^+$ ion intensity) [III].

6.6 *Operando* X-ray synchrotron total scattering data

Operando X-ray total scattering data were obtained to study the structural changes in the hard carbon (GDHC 1100) upon operation in NIB and LIB half cells. Analysis of such a disordered structure is difficult, as the signals tend to be weak and produce broad peaks due to the non-periodic nature of the material. Therefore, only limited information can be obtained from the scattering patterns with traditional crystallographic methods. In order to extract information from weak reflections of X-ray scattering, pair distribution analysis (PDF) of the scattering data in real space was employed.

The PDF obtained from the hard carbon electrode before cycling is shown in **Figure 44**. The PDF clearly illustrates the limited structural coherence in the hard carbon material as no long-range order peaks are seen above 25 Å. However, the sample has very well-defined local range order as seen from the sharp low *r*-range peaks, corresponding to the C–C correlations indicated in the insert structure. The loss of long-range order has been proposed to be caused by termination of carbon fragment sheets by either hydrogen atoms or a functionalized group or by the presence of non-hexagonal rings causing sheet curvature [153].

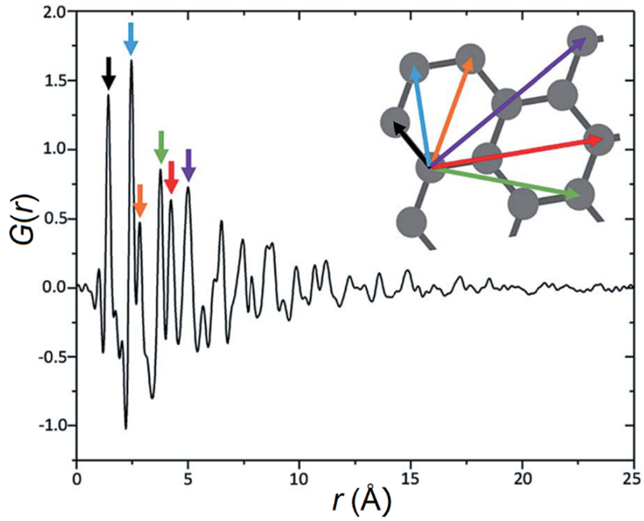

Figure 44. PDF of pristine GDHC 1100 in the full *r*-range revealing absence of long-range order.

The resulting plot of *operando* PDFs upon charge is presented in **Figure 45**. In the range shown in the figure, the PDF is mainly dominated by the C–C correlations in a single graphene sheet, as indicated by the marked distances in **Figure 44**. As the concentration of sodium in the hard carbon material increases during sodiation, denoting charge of the half cell, it is clearly illustrated that the whole graphene layer structure, including the closest C–C bond distance in the benzene ring, becomes more disordered upon sodiation as peak broadening is seen (**Figure 45**, below). Similar broadening effects were observed from *ex situ* measurements of hard carbon samples obtained from different stages of the charge process in a pouch half cell (Fig. S2 ESI in paper IV). Interestingly, the intensity of the peak seen in the experimental PDF at 3.2 Å (indicated by the arrow) increases upon sodiation, which would indicate an increase in the presence of seven-membered rings, and therefore introduction of bond breakage and associated disorder [122], but is likely related to broadening of the surrounding peaks, smearing out the electron density and therefore resulting in intensity increase around the peak center. Finally, as seen in the operando PDFs upon subsequent charge–discharge cycles, the peaks representing the C–C correlated distances never fully reach the features of the fully de-sodiated state found in the initial hard carbon material, as they still contain a significant degree of disorder. In **Figure 45**, this is especially visible at 1.42 Å, where the sharpness of the initial peak is never recovered. Also, the galvanostatic charge-discharge profiles in **Figure 46** reveal that the *operando* capillary cell did not produce a plateau at $E < 0.1$ V, which means the charge storage mechanism in that region could not be studied in this work. Consequently, the irreversible capacity loss and further capacity fading might indicate that the sodium is consumed in electrolyte decomposition reactions, resulting in less sodium being available for insertion upon subsequent charging cycles.

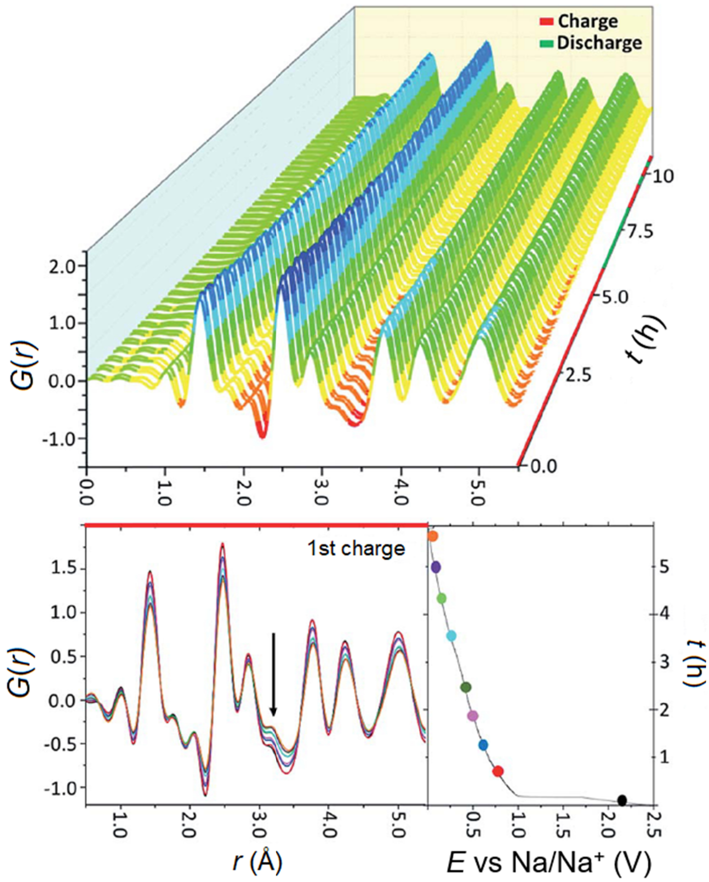

Figure 45. *Operando* study of the dynamic evolution of the graphene structure upon sodiation. (Top) *Operando* PDF data in the r-range representing the graphene correlation structure as a function of electrochemical state (indicated in the bar diagram on the right of the figure). (Below) Selected *operando* PDFs of the first charge cycle relating the electrochemical state-of-charge (SOC) and the changes in real space.

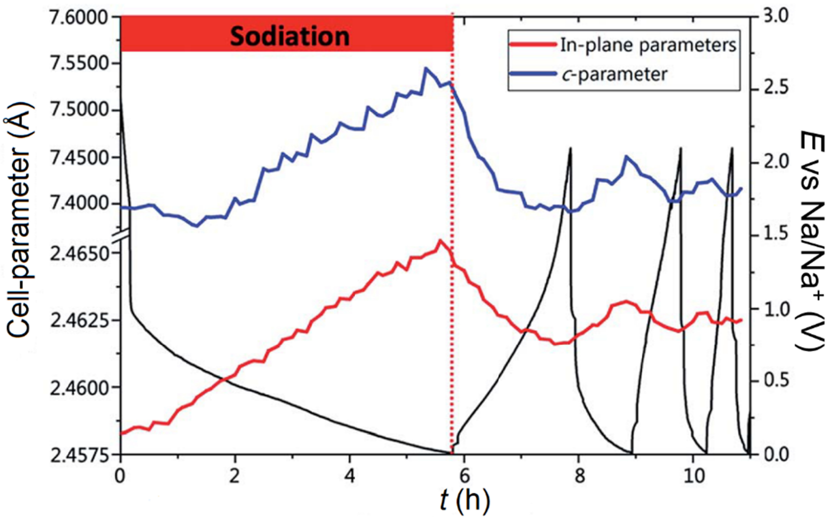

Figure 46. Refinement of cell parameters *a* and *c* of the hard carbon structure upon sodiation as a function of state-of-charge (SOC). The SOC of the half cell is indicated as the black curve with corresponding cell potential on the right y-axis. The red bar diagram indicates when the first sodiation process occurs.

Quantitative analysis of the operando PDFs was done employing the presented extended graphite model, which was refined to the time-resolved data. **Figure 46** shows the refined *a* and *c* parameters as a function of time, representing the SOC. As observed in **Figure 46**, both *a* and *c* increase upon sodiation. The increase in *c*-parameter indicates intercalation, where sodium inserts between nearly aligned graphene sheets causing the interlayer space to expand. Consequently, as discharging is associated with de-intercalation, a decrease in *c*-parameter is also observed. In addition, the expansion of the in-plane graphene cell parameters, corresponding to the C–C bonds in the graphene layers, has previously been observed in lithiated graphite [154], potassium intercalation in graphite [155], and studied using theoretical *ab initio* calculations [156]. The bond-length increase in the graphite intercalated systems was associated with an electron transfer from the *s*-orbitals of the intercalated ion to the antibonding orbitals in the upper π-band of the intercalate layers in the graphite, which is consistent with the C–C bond reduction and resulting elongation found in the graphene sheets. The quality of the fit using the altered graphite model was improved by modelling the PDF independently in two *r*-ranges: the low-*r* range from 1–5 Å and the high-*r* range from 4.5–10 Å, of which the refinement fit is presented in Fig. S4 ESI of paper IV. The refined *a* parameter for the 1–5 Å range (blue) and 4.5–10 Å range (red) is shown in **Figure 47a** along with the parameters obtained from the fit of the entire *r*-range from 1–15 Å (black). Fitting in the local *r*-range gives significantly larger in-plane parameters than when fitting to the longer-range order peaks, indicating that one single model cannot describe the whole structure. The behavior can be understood in terms of curvature of the graphene sheets as also observed by Stratford et al. [52]. Comparing a planar graphene sheet and a curved structure, the resulting distances between carbon atoms at high-r will significantly differ in the two models. In a curved structural model, the result of moving into the high-r region results in carbon atoms being closer together than described by the planar model, which is schematically illustrated in **Figure 47b**. The effect is seen throughout the cycling process of the half cell and appears intrinsic to the hard carbon structure and not affected by sodiation. Additionally, the intrinsic behavior of curved sheets was further supported by HRTEM, in which more isolated graphene sheets were found to exhibit pronounced curvature, whereas less pronounced curvature was observed for multilayered graphene sheets as illustrated in **Figure 16**.

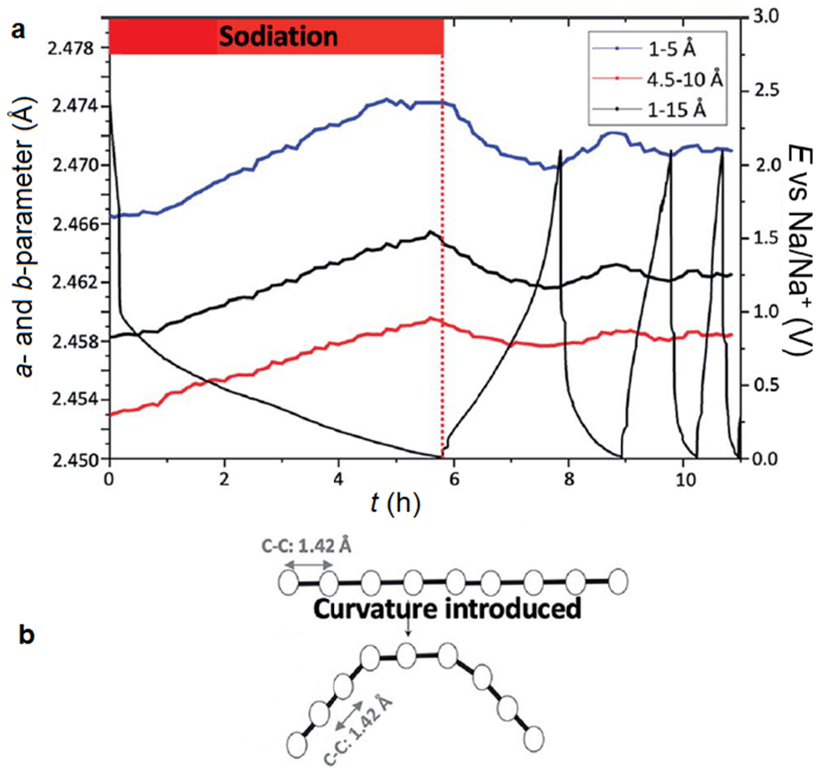

Figure 47. (a) Refinement of cell parameters *a* and *b* of the hard carbon structure upon sodiation in the three *r*-ranges of refinement as a function of SOC. The GCD profile of the half cell is indicated as the black curve with corresponding cell potential on the right of the figure. The red bar diagram indicates when the first sodiation process occurs (b) Schematic illustration of how the effect of curvature influences the *r*-ranges utilized in the refinement.

The atomic displacement parameters (ADPs) describing atomic motion in and between the graphene layers, U_{11}/U_{12} and U_{33}, respectively, are used to quantify the degree of disorder present. The in-plane ADPs (U_{11} and U_{22}) refined in the long-range order regime are less affected by the cycling process; and as seen in the pristine hard carbon PDF (**Figure 44**), the structure is already intrinsically dominated by short-range order in the graphene sheet, whereas long-range order is significantly weaker due to either the presence of curvature or termination of graphene fragments in the material as discussed previously. Therefore, the induced disorder in the structure upon sodiation does not affect the intrinsic long-range structure, as a significant degree of disorder is already present.

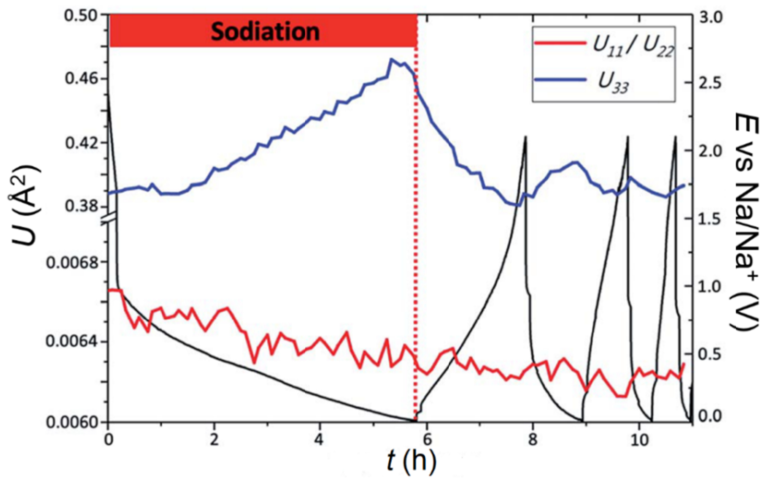

Figure 48. Atomic displacement parameters (ADPs) of hard carbon upon sodiation from high-*r* refinement (4.5–10 Å). The red curve displays in-plane ADPs, U_{11}/U_{22}, whereas the blue curve displays the interlayer ADPs, U_{33}. The GCD profile of the half cell is indicated as the black curve with corresponding cell potential on the right of the figure. The red bar diagram indicates when the first sodiation process occurs.

The ADP describing the interlayer disorder (U_{33}) is well correlated with the SOC of the half cell. The increasing displacement parameter in the high-*r* region upon sodiation suggests either that the electron distribution from the graphene layers becomes delocalized or that the model is not sufficient for describing the disordered structure.

In order to verify whether Na-metal clusters are formed in the sloping region, differential pair distribution function (d-PDF) analysis was conducted. The approach achieved through this implementation isolates correlations arising from the modification of the structure by sodiation. Consequently, the direct subtraction performed between the state with no sodium present (the discharged half cell) and the sodiated state (charged half cell) directly provides peaks, where sodium interactions can be identified as the carbon signal is subtracted from the resulting data. As observed in the d-PDF, no significant sodium–sodium interactions were revealed in the local structure (Fig. S5 ESI in paper IV), illustrated by the absence of the features at 3.7 Å, 7 Å and 9.5 Å, corresponding to sodium metal and cluster formation [59]. This is in good agreement with galvanostatic cycling aspect of the *operando* experiment where no plateaus were formed at E < 0.1 V vs Na/Na^+, which is attributed to Na cluster formation in micropores [61,157].

6.6.1 Lithium insertion into hard carbon

In order to gain more insight into how alkali ion insertion in hard carbon can be described, an *operando* experiment with lithium was performed with identical electrochemical conditions. The insertion mechanism of Li into GDHC 1100 was found to be similar to Na. The PDFs from lithiation of hard carbon display the same peak broadening behavior, indicating induced disorder in the structure as observed for hard carbon sodiation. As identified in the real-space least-squares refinement, similar expansion of the in-plane graphene parameters upon lithiation is observed as revealed upon sodiation (Fig. S8 ESI in paper IV). However, the *c*-parameter did not appear to follow the same rate of increasing behavior as observed upon sodiation. This might be attributed to the smaller size of lithium causing a less hindered insertion and extraction of lithium from the structure with a less pronounced impact on the interlayer spacing. However, as proposed by Liu et al. based on DFT calculations, the very similar Li^+ and Na^+ display different insertion behavior in graphite due to the weaker binding of sodium to the substrate [158]. Therefore, to further elucidate why such differences are present and if the lower rate of interlayer expansion might be related to this behavior, the in-plane response to the ion insertion procedure was investigated by comparing the percentage change of the in-plane cell parameters from the initial pristine model.

The calculation was performed by subtracting the initial value of the in-plane parameter from each subsequent in-plane parameter provided from the refinement, followed by conversion to a percentage change. As illustrated in **Figure 49** (black curve), the insertion of sodium in the hard carbon material results in a change of in-plane cell parameters approximately 60% larger than for lithium insertion. Considering the ionic sizes of sodium and lithium (116 pm and 90 pm, respectively [159]), the 20% larger sodium ion should cause a smaller expansion. However, this insertion model does not consider electron charge transfer to the graphene sheet. The in-plane expansion would therefore be a combination of both size-accommodating interaction and charge transfer causing reduction. Furthermore, the increased expansion of the graphene layer upon sodiation suggests that the ion insertion behavior might not be fully described through the previously mentioned local electron transfer model to the antibonding π-orbitals of the graphene layers.

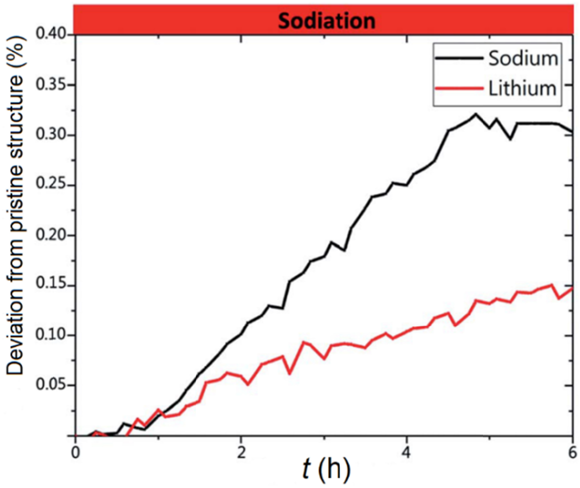

Figure 49. The difference in in-plane behavior upon ion insertion. The figure illustrates the relative change of the in-plane cell parameters upon ion insertion. The black curve displays the sodiation response, whereas the red curve provides the lithiation response. The red bar diagram indicates when the first sodiation process occurs.

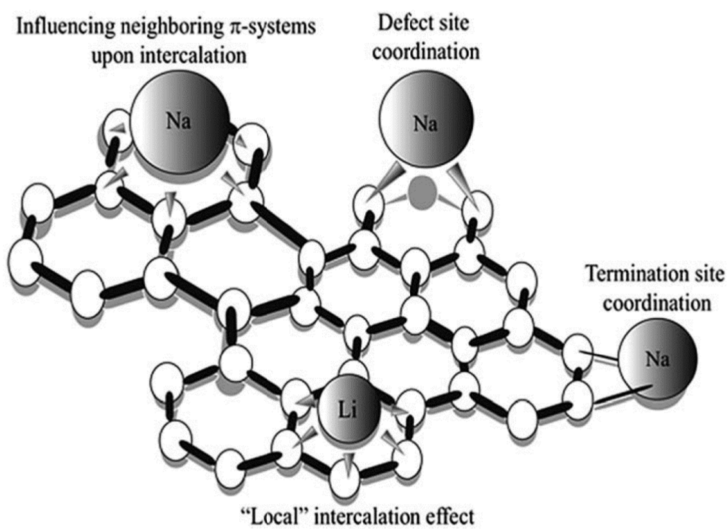

Figure 50. Mechanisms of Li^+ and Na^+ ion insertion and the corresponding structural impact on the graphene layer.

The larger sodium appears to influence the *p*-orbitals of the neighboring conjugated benzene rings to a larger extent as it is inserted into the hard carbon and causes larger interlayer expansion. This means that the electron transfer contribution is more delocalized with sodium, unlike with lithium, which seems to have more localized effects. Consequently, this means that as hard carbon, to some extent, is found to resemble the behavior of ion intercalation in graphite upon both sodiation and lithiation, i.e. C–C bond elongation and interlayer expansion, it is proposed that the mechanism of ion insertion most likely follows an intercalating procedure. In this process, the sodium or lithium ions will intercalate between graphene layers resulting in interlayer expansion, following a charge transfer from the ions to the graphene layer with subsequent charge delocalization, causing a C–C bond length reduction. The structural impact is more pronounced upon intercalation of the larger Na-ion as compared to lithiation, which is suggested to relate to an electron transfer contribution to the neighboring, conjugated hexagonally coordinated carbon rings next to where the sodium is positioned in the structure as illustrated in **Figure 50**. The previously proposed mechanism of metallic sodium and coordination at defect or termination sites are however not directly observed in the given experiment. However, these mechanisms might occur in the hard carbon, but at a later stage in the sodiation process, which in this experiment is limited by the low capacity obtained.

7. SUMMARY

This study mostly focused on electrochemical half cell characterizations of a glucose-derived hard carbon (GDHC) synthesized using hydrothermal carbonization (HTC) and post heat treatment at 1100 ºC (GDHC 1100). The nature of electrochemical processes occurring on the electrode surface were investigated using various Li^+-, Na^+- and K^+ salts in different solvent blends. Cyclic voltammetry (CV), galvanostatic charge-discharge (GCD) and electrochemical impedance spectroscopy (EIS) with equivalent circuit fitting were used for electrochemical characterization. *Ex-situ* characterizations of cycled electrodes were carried out using Raman spectroscopy, laser ablation inductively coupled plasma mass spectrometry (LA-ICP-MS) and time-of-flight secondary ion mass spectrometry (TOF-SIMS). Finally, total *operando* X-ray scattering experiments were conducted along with pair distribution function (PDF) analysis to determine structural changes happening to the GDHC 1100 hard carbon in real time upon sodiation/de-sodiation and lithiation/de-lithiation.

The best galvanostatic cycling results were achieved using 1 M $NaPF_6$ in EC:PC (1:1) electrolyte – 350 mAh g^{-1} (of which 175 mAh g^{-1} plateau) at 50 mA g^{-1}. The same solvent blend with $LiPF_6$ reached even 375 mAh g^{-1}, but the plateau region was limited to 100 mAh g^{-1}. It seems that the use of PC enhances micropore filling that his attributed to the plateau region of galvanostatic profiles, because the plateau was either missing in case of $LiPF_6$ EC:DMC (1:1) or much shorter with $NaPF_6$ EC:DMC (1:1).

EIS study with equivalent circuit fitting in a wide potential range showed that 1 M $LiPF_6$ EC:DMC (1:1) might form a much thicker and more stable solid electrolyte interphase (SEI) than 1 M $NaPF_6$ EC:DMC (1:1), 0.8 M KPF_6 EC:DEC (1:1) or 1 M $NaClO_4$ PC, as its resistance (R_{SEI}) and capacitance (C_{SEI}) were much higher: ~25 Ω cm^2 and 4.5 μF cm^{-2}, respectively. Low R_{SEI} (6 Ω cm^2) and relatively high C_{SEI} value (3 μF cm^{-2}) for 1 M $NaClO_4$ PC may suggest that PC either co-intercalates into the graphitic domains or that $NaClO_4$ PC decomposition products are more soluble than that of $LiPF_6$ EC:DMC.

Ex-situ LA-ICP-MS investigation of sodiated GDHC 1100 showed a 375-fold increase in Na concentration in/on the electrode compared to the electrode that was only soaked in the electrolyte.

I_D/I_G parameter calculated from *ex-situ* Raman data of sodiated and lithiated GDHC electrodes showed only a small increase, which implies only a slight increase of disordering of the hard carbon. However, TOF-SIMS study of sodiated and lithiated electrode surfaces revealed that the decomposition products found on the sodiated electrode are more inorganic than on the lithiated surface. In addition, the mass spectrum of the lithiated surface contained far more fragments than the spectrum of the sodiated surface, which means that the decomposition products in NIBs are much more soluble than in LIBs.

Total *operando* X-ray scattering of NIB and LIB half cells with GDHC 1100 revealed that Na insertion causes in-plane C–C bond elongation that could be caused by increased curvature of the graphene layers. Also, the 20% larger Na ion causes 60% increase in in-plane parameters, which may be the result of delocalized electron transfer contribution to the benzene rings. The fact that in-plane bond elongation occurs in the sloping region supports the "intercalation-adsorption" mechanism.

In an effort to test the GDHCs in a real battery cell, GDHCs were synthesized at 1400–1600 ºC and $Na_3V_2(PO_4)_3$ (NVP) positive electrode material was synthesized using glycine-nitrate process (GNP). Both materials were first separately characterized in respective half cells and then full cell tests were conducted to test the characteristics of battery GDHC||NVP cell.

GDHCs 1400–1600 show higher coulombic efficiencies (80%) and reversible capacities (300 mAh g^{-1}), including plateau region capacities (200 mAh g^{-1}) than GDHC 1100. Reducing conductive additive (Super P) content from 15% to 4% increased 1st cycle coulombic efficiency to 85%. The best results were achieved with GDHC 1400 b (reduced Super P content) – reversible discharge capacity 272 mAh g^{-1} of which plateau 155 mAh g^{-1}.

Various approaches were used to form the NVP precursor. The best results were obtained using the Spray method – 102 mAh g^{-1} at C/20 and with scale up of the synthesis procedure, high energy performance was also achieved – 60 mAh g^{-1} at 20C. Reversible capacity of the GDHC||NVP full cell reached 80 mAh g^{-1} by NVP mass (60 mAh g^{-1} at 3.3V i.e. the plateau region) and a specific energy of 189 Wh kg^{-1} and energy density of 104 Wh dm^{-3} were calculated. After 80 cycles, including rate testing from C/20 to 10C, the cell had retained 65 mAh g^{-1} with 99.7% CE.

These results show that further investigations into the Na storage mechanism in hard carbons is necessary for developing negative electrodes with a high plateau capacity that in turn enable high energy density full cells. Finding ways to reduce irreversible capacity and improve the stability of the SEI will be the key problems to address before fully commercializing this technology.

8. REFERENCES

[1] V. Nelson, K. Starcher, K. Starcher, Wind Energy: Renewable Energy and the Environment, CRC Press, 2018.
[2] G. Notton, M.-L. Nivet, C. Voyant, C. Paoli, C. Darras, F. Motte, A. Fouilloy, Renew. Sustain. Energy Rev. 87 (2018) 96–105.
[3] R. Dell, D.A.J. Rand, Understanding Batteries, Royal Society of Chemistry, Cambridge, 2001.
[4] British Geological Survey – Risk List 2015, British Geological Survey, 2015.
[5] B.L. Ellis, L.F. Nazar, Curr. Opin. Solid State Mater. Sci. 16 (2012) 168–177.
[6] X. Dou, I. Hasa, D. Saurel, C. Vaalma, L. Wu, D. Buchholz, D. Bresser, S. Komaba, S. Passerini, Mater. Today 23 (2019) 87–104.
[7] R. Mogensen, D. Brandell, R. Younesi, ACS Energy Lett. 1 (2016) 1173–1178.
[8] M. Moshkovich, Y. Gofer, D. Aurbach, J. Electrochem. Soc. 148 (2001) E155–E167.
[9] G.W.A. Drummer, Electronic Inventions and Discoveries: Electronics from Its Earliest Beginnings to the Present Day, Fourth Edition, CRC Press, 1997.
[10] V.G. Christensen, How Batteries Work, Lerner Publications, 2016.
[11] G. Pancaldi, Volta: Science and Culture in the Age of Enlightenment, Princeton University Press, 2005.
[12] H.H. Schobert, Energy and Society: An Introduction, CRC Press, 2002.
[13] C. Grimes, O. Varghese, S. Ranjan, Light, Water, Hydrogen: The Solar Generation of Hydrogen by Water Photoelectrolysis, Springer Science & Business Media, 2007.
[14] D. Pavlov, Lead-Acid Batteries: Science and Technology, Elsevier, 2011.
[15] A.E.E. McKenzie, Magnetism and Electricity, Cambridge University Press, Cambridge, UK, 1961.
[16] K. Desmond, Innovators in Battery Technology: Profiles of 95 Influential Electrochemists, McFarland, 2016.
[17] K. Sapru, B. Reichman, A. Reger, S.R. Ovshinsky, Rechargeable Battery and Electrode Used Therein, US4623597A, 1986.
[18] M. Yoshio, R.J. Brodd, A. Kozawa, Lithium-Ion Batteries: Science and Technologies, Springer Science & Business Media, 2010.
[19] P. Jankowski, W. Wieczorek, P. Johansson, J. Mol. Model. 23 (2017) 6.
[20] R. Yazami, Ph. Touzain, J. Power Sources 9 (1983) 365–371.
[21] S. Basu, Ambient Temperature Rechargeable Battery, US4423125A, 1983.
[22] J. Vetter, P. Novak, M.R. Wagner, C. Veit, K.-C. Moller, J.O. Besenhard, M. Winter, M. Wohlfahrt-Mehrens, C. Vogler, A. Hammouche, J. Power Sources 147 (2005) 269–281.
[23] H. Hou, X. Qiu, W. Wei, Y. Zhang, X. Ji, Adv. Energy Mater. 7 (2017) 1602898–1602928.
[24] Yung-Fang Yu Yao, J.T. Kummer, J. Inorg. Nucl. Chem. 29 (1967) 2453–2475.
[25] J.T. Kummer, W. Neill, Battery Having a Molten Alkali Metal Anode and a Molten Sulfur Cathode, US3413150 A, 1968.
[26] X. Lu, J.P. Lemmon, V. Sprenkle, Z. Yang, JOM 62 (2010) 31–36.
[27] N. Yabuuchi, K. Kubota, M. Dahbi, S. Komaba, Chem. Rev. 114 (2014) 11636–11682.
[28] H. Pan, Y.-S. Hu, L. Chen, Energy Environ. Sci. 6 (2013) 2338–2360.

[29] M. Dahbi, N. Yabuuchi, K. Kubota, K. Tokiwa, S. Komaba, Phys. Chem. Chem. Phys. 16 (2014) 15007.
[30] M.D. Slater, D. Kim, E. Lee, C.S. Johnson, Adv. Funct. Mater. 23 (2013) 947–958.
[31] R. Sayers, J. Barker, R. Heap, Compositions Containing Doped Nickelate Compounds, WO2015177544A1, 2015.
[32] S.Y. Lim, H. Kim, R.A. Shakoor, Y. Jung, J.W. Choi, J. Electrochem. Soc. 159 (2012) A1393–A1397.
[33] P. Ge, M. Fouletier, Solid State Ion. 28 (1988) 1172–1175.
[34] M.M. Doeff, Y. Ma, S.J. Visco, L.C.D. Jonghe, J. Electrochem. Soc. 140 (1993) L169–L170.
[35] K. Nobuhara, H. Nakayama, M. Nose, S. Nakanishi, H. Iba, J. Power Sources 243 (2013) 585–587.
[36] B. Jache, P. Adelhelm, Angew. Chem. Int. Ed. 53 (2014) 10169–10173.
[37] H. Kim, J. Hong, G. Yoon, H. Kim, K.-Y. Park, M.-S. Park, W.-S. Yoon, K. Kang, Energy Environ. Sci. 8 (2015) 2963–2969.
[38] M. Winter, J.O. Besenhard, M.E. Spahr, P. Novák, Adv. Mater. 10 (1998) 725–763.
[39] L.P. Wang, Y. Zhao, C. Wei, C. Wong, M. Srinivasan, Z.J. Xu, J. Mater. Chem. A 3 (2015) 14033–14038.
[40] C. Daniel, J.O. Besenhard, eds., Handbook of Battery Materials (2nd Ed), 2nd ed., Wiley-VCH ; John Wiley [distributor], Weinheim, Germany : Chichester, 2012.
[41] M. Noel, V. Suryanarayanan, J. Power Sources 111 (2002) 193–209.
[42] B.N. Loeffler, D. Bresser, S. Passerini, M. Copley, Johns. Matthey Technol. Rev. 59 (2015) 34–44.
[43] S. Komaba, W. Murata, T. Ishikawa, N. Yabuuchi, T. Ozeki, T. Nakayama, A. Ogata, K. Gotoh, K. Fujiwara, Adv. Funct. Mater. 21 (2011) 3859–3867.
[44] I.A.S. Edwards, R. Menendez, H. Marsh, Introduction to Carbon Science, Butterworth-Heinemann, 2013.
[45] D.M. Ruthven, Principles of Adsorption and Adsorption Processes, John Wiley & Sons, 1984.
[46] A. Kano, N. Hojo, M. Fujimoto, Negative-Electrode Active Material for Sodium-Ion Secondary Battery, Method for Manufacturing Said Negative-Electrode Active Material, and Sodium-Ion Secondary Battery, US9755237B2, 2017.
[47] H. Marsh, F.R. Reinoso, Activated Carbon, Elsevier, London, 2006.
[48] D.A. Stevens, J.R. Dahn, J. Electrochem. Soc. 147 (2000) 4428–4431.
[49] E. Buiel, J.R. Dahn, Electrochim. Acta 45 (1999) 121–130.
[50] V. Simone, A. Boulineau, A. de Geyer, D. Rouchon, L. Simonin, S. Martinet, J. Energy Chem. 25 (2016) 761–768.
[51] E.M. Lotfabad, J. Ding, K. Cui, A. Kohandehghan, W.P. Kalisvaart, M. Hazelton, D. Mitlin, ACS Nano 8 (2014) 7115–7129.
[52] J. Ding, H. Wang, Z. Li, A. Kohandehghan, K. Cui, Z. Xu, B. Zahiri, X. Tan, E.M. Lotfabad, B.C. Olsen, D. Mitlin, ACS Nano 7 (2013) 11004–11015.
[53] M. Dahbi, M. Kiso, K. Kubota, T. Horiba, T. Chafik, K. Hida, T. Matsuyama, S. Komaba, J. Mater. Chem. A 5 (2017) 9917–9928.
[54] V.G. Pol, E. Lee, D. Zhou, F. Dogan, J.M. Calderon-Moreno, C.S. Johnson, Electrochim. Acta 127 (2014) 61–67.
[55] A. Beda, P.-L. Taberna, P. Simon, C. Matei Ghimbeu, Carbon 139 (2018) 248–257.

[56] K. Kubota, M. Dahbi, T. Hosaka, S. Kumakura, S. Komaba, Chem. Rec. 18 (2018) 459–479.
[57] D.A. Stevens, J.R. Dahn, J. Electrochem. Soc. 148 (2001) A803–A811.
[58] D.A. Stevens, J.R. Dahn, J. Electrochem. Soc. 147 (2000) 1271–1273.
[59] J.M. Stratford, P.K. Allan, O. Pecher, P.A. Chater, C.P. Grey, Chem. Commun. 52 (2016) 12430–12433.
[60] Y.S. Yun, K.-Y. Park, B. Lee, S.Y. Cho, Y.-U. Park, S.J. Hong, B.H. Kim, H. Gwon, H. Kim, S. Lee, Y.W. Park, H.-J. Jin, K. Kang, Adv. Mater. 27 (2015) 6914–6921.
[61] C. Bommier, T.W. Surta, M. Dolgos, X. Ji, Nano Lett. 15 (2015) 5888–5892.
[62] S. Qiu, L. Xiao, M.L. Sushko, K.S. Han, Y. Shao, M. Yan, X. Liang, L. Mai, J. Feng, Y. Cao, X. Ai, H. Yang, J. Liu, Adv. Energy Mater. 7 (2017) 1700403.
[63] M. Sevilla, A.B. Fuertes, Carbon 47 (2009) 2281–2289.
[64] M. Sevilla, A.B. Fuertes, Chem. – Eur. J. 15 (2009) 4195–4203.
[65] T. Thomberg, T. Tooming, T. Romann, R. Palm, A. Jänes, E. Lust, J. Electrochem. Soc. 160 (2013) A1834–A1841.
[66] M.-M. Titirici, R.J. White, C. Falco, M. Sevilla, Energy Environ. Sci. 5 (2012) 6796–6822.
[67] J. Hwang, K. Matsumoto, R. Hagiwara, ACS Appl. Energy Mater. 2 (2019) 2818–2827.
[68] J. Gopalakrishnan, K.K. Rangan, Chem. Mater. 4 (1992) 745–747.
[69] Z. Jian, L. Zhao, H. Pan, Y.-S. Hu, H. Li, W. Chen, L. Chen, Electrochem. Commun. 14 (2012) 86–89.
[70] X. Cao, A. Pan, B. Yin, G. Fang, Y. Wang, X. Kong, T. Zhu, J. Zhou, G. Cao, S. Liang, Nano Energy 60 (2019) 312–323.
[71] W.-J. Li, C. Han, W. Wang, F. Gebert, S.-L. Chou, H.-K. Liu, X. Zhang, S.-X. Dou, Adv. Energy Mater. 7 (2017) 1700274.
[72] G. Li, Z. Yang, Y. Jiang, C. Jin, W. Huang, X. Ding, Y. Huang, Nano Energy 25 (2016) 211–217.
[73] F. Deganello, A.K. Tyagi, Prog. Cryst. Growth Charact. Mater. 64 (2018) 23–61.
[74] A.E. Danks, S.R. Hall, Z. Schnepp, Mater. Horiz. 3 (2016) 91–112.
[75] S.R. Jain, K.C. Adiga, V.R. Pai Verneker, Combust. Flame 40 (1981) 71–79.
[76] S. Hajarpour, Kh. Gheisari, A. Honarbakhsh Raouf, J. Magn. Magn. Mater. 329 (2013) 165–169.
[77] S. Singh, D. Singh, Ceram. Int. 42 (2016) 15725–15731.
[78] L.A. Chick, L.R. Pederson, G.D. Maupin, J.L. Bates, L.E. Thomas, G.J. Exarhos, Mater. Lett. 10 (1990) 6–12.
[79] M. Vujković, M. Mitrić, S. Mentus, J. Power Sources 288 (2015) 176–186.
[80] T.H.N.G. Amaraweera, A. Wijayasinghe, B.-E. Mellander, M.A.K.L. Dissanayake, Ionics 23 (2017) 3001–3011.
[81] A. Habibi, M. Jalaly, R. Rahmanifard, M. Ghorbanzadeh, Mater. Res. Express 5 (2018) 025506.
[82] D.D. Sloovere, W. Marchal, F. Ulu, T. Vranken, M. Verheijen, M.K.V. Bael, A. Hardy, RSC Adv. 7 (2017) 18745–18754.
[83] R. Zhang, X. Yang, D. Zhang, H. Qiu, Q. Fu, H. Na, Z. Guo, F. Du, G. Chen, Y. Wei, J. Power Sources 285 (2015) 227–234.
[84] C. Ferrara, C. Tealdi, V. Dall'Asta, D. Buchholz, L.G. Chagas, E. Quartarone, V. Berbenni, S. Passerini, Batteries 4 (2018) 8.

[85] M.M. Doeff, T.J. Richardson, J. Hollingsworth, C.-W. Yuan, M. Gonzales, J. Power Sources 112 (2002) 294–297.
[86] T.A. Eriksson, M.M. Doeff, J. Power Sources 119–121 (2003) 145–149.
[87] M.M. Doeff, T.J. Richardson, K.-T. Hwang, J. Power Sources 135 (2004) 240–248.
[88] J.A. Saint, M.M. Doeff, J. Wilcox, Chem. Mater. 20 (2008) 3404–3411.
[89] V. Etacheri, R. Marom, R. Elazari, G. Salitra, D. Aurbach, Energy Environ. Sci. 4 (2011) 3243–3262.
[90] M. Ue, in: Embassy Suites Deerfield Beach Resort, Deerfield, FL, USA, 1998, pp. 169–187.
[91] M.S. Ding, K. Xu, S. Zhang, T.R. Jow, J. Electrochem. Soc. 148 (2001) A299–A304.
[92] D.R. Lide, Handbook of Organic Solvents, 1 edition, CRC Press, Boca Raton, 1995.
[93] J. Barthel, R. Neueder, Electrolyte Data Collection: Tables, Diagrams, Correlations, and Literature Survey, DECHEMA, 1999.
[94] D.R. Lide, CRC Handbook of Chemistry and Physics, 85th Edition, CRC Press, 2004.
[95] A.V. Cresce, S.M. Russell, O. Borodin, J.A. Allen, M.A. Schroeder, M. Dai, J. Peng, M.P. Gobet, S.G. Greenbaum, R.E. Rogers, K. Xu, Phys. Chem. Chem. Phys. 19 (2016) 574–586.
[96] A. Ponrouch, E. Marchante, M. Courty, J.-M. Tarascon, M.R. Palacín, Energy Environ. Sci. 5 (2012) 8572.
[97] Y. Gogotsi, R.M. Penner, ACS Nano 12 (2018) 2081–2083.
[98] A.J. Bard, L.R. Faulkner, Electrochemical Methods: Fundamentals and Applications, Wiley, New York, 2001.
[99] E. Barsoukov, J.R. Macdonald, Impedance Spectroscopy: Theory, Experiment, and Applications, Wiley, John & Sons, Incorporated, 2005.
[100] M.E. Orazem, B. Tribollet, Electrochemical Impedance Spectroscopy, John Wiley & Sons, 2011.
[101] M.D. Murbach, D.T. Schwartz, J. Electrochem. Soc. 165 (2018) A297–A304.
[102] S. Fletcher, J. Electrochem. Soc. 141 (1994) 1823–1826.
[103] T.Q. Nguyen, C. Breitkopf, J. Electrochem. Soc. 165 (2018) E826–E831.
[104] B. Hirschorn, M.E. Orazem, B. Tribollet, V. Vivier, I. Frateur, M. Musiani, J. Electrochem. Soc. 157 (2010) C458–C463.
[105] B.A. Boukamp, Solid State Ion. 20 (1986) 31–44.
[106] A.S. Masadeh, J. Exp. Nanosci. 11 (2016) 951–974.
[107] R.E. Johnsen, P. Norby, J. Appl. Crystallogr. 46 (2013) 1537–1543.
[108] A.S. Christiansen, R.E. Johnsen, P. Norby, C. Frandsen, S. Mørup, S.H. Jensen, K.K. Hansen, P. Holtappels, J. Electrochem. Soc. 162 (2015) A531–A537.
[109] T. Tooming, T. Thomberg, H. Kurig, A. Jänes, E. Lust, J. Power Sources 280 (2015) 667–677.
[110] T. Tooming, T. Thomberg, L. Siinor, K. Tõnurist, A. Jänes, E. Lust, J. Electrochem. Soc. 161 (2014) A222–A227.
[111] W. Xing, J.S. Xue, J.R. Dahn, J. Electrochem. Soc. 143 (1996) 3046–3052.
[112] E. Buiel, A.E. George, J.R. Dahn, J. Electrochem. Soc. 145 (1998) 2252–2257.
[113] E. Irisarri, A. Ponrouch, M.R. Palacin, J. Electrochem. Soc. 162 (2015) A2476–A2482.
[114] R.A. Adams, V.G. Pol, A. Varma, Ind. Eng. Chem. Res. 56 (2017) 7173–7183.

[115] L. Yang, M. Wang, D. Zeng, Precursor Formulation for Battery Active Materials Synthesis, US20120288617A1, 2012.
[116] H. Wang, D. Jiang, Y. Zhang, G. Li, X. Lan, H. Zhong, Z. Zhang, Y. Jiang, Electrochim. Acta 155 (2015) 23–28.
[117] P. Juhás, T. Davis, C.L. Farrow, S.J.L. Billinge, J. Appl. Crystallogr. 46 (2013) 560–566.
[118] A.P. Hammersley, J. Appl. Crystallogr. 49 (2016) 646–652.
[119] V. Petkov, R.G. Difrancesco, S.J.L. Billinge, M. Acharya, H.C. Foley, Philos. Mag. B 79 (1999) 1519–1530.
[120] A.H.R. Palser, Phys. Chem. Chem. Phys. 1 (1999) 4459–4464.
[121] M.B. Dowell, R.A. Howard, Carbon 24 (1986) 311–323.
[122] A.C. Forse, C. Merlet, P.K. Allan, E.K. Humphreys, J.M. Griffin, M. Aslan, M. Zeiger, V. Presser, Y. Gogotsi, C.P. Grey, Chem. Mater. 27 (2015) 6848–6857.
[123] X. Dou, C. Geng, D. Buchholz, S. Passerini, APL Mater. 6 (2018) 047501.
[124] B.E. Conway, Electrochemical Supercapacitors: Scientific Fundamentals and Technological Applications, Springer, New York, 1999.
[125] T. Brousse, D. Bélanger, J.W. Long, J. Electrochem. Soc. 162 (2015) A5185–A5189.
[126] S. Kajiyama, L. Szabova, K. Sodeyama, H. Iinuma, R. Morita, K. Gotoh, Y. Tateyama, M. Okubo, A. Yamada, ACS Nano 10 (2016) 3334–3341.
[127] H. Kumar, E. Detsi, D.P. Abraham, V.B. Shenoy, Chem. Mater. 28 (2016) 8930–8941.
[128] T. Abe, N. Kawabata, Y. Mizutani, M. Inaba, Z. Ogumi, J. Electrochem. Soc. 150 (2003) A257–A261.
[129] G. Pistoia, Lithium Batteries: New Materials, Developments, and Perspectives, Elsevier, 1994.
[130] I. Mochida, C.-H. Ku, S.-H. Yoon, Y. Korai, J. Power Sources 75 (1998) 214–222.
[131] Y. Wen, K. He, Y. Zhu, F. Han, Y. Xu, I. Matsuda, Y. Ishii, J. Cumings, C. Wang, Nat. Commun. 5 (2014) 4033.
[132] K. Omichi, G. Ramos-Sanchez, R. Rao, N. Pierce, G. Chen, P.B. Balbuena, A.R. Harutyunyan, J. Electrochem. Soc. 162 (2015) A2106–A2115.
[133] J. Jamnik, M. Gaberscek, MRS Bull. 34 (2009) 942–948.
[134] S.E. Lee, M.H. Tang, Electrochem. Commun. 100 (2019) 70–73.
[135] B. Guo, W. Diao, T. Yuan, Y. Liu, Q. Yuan, G. Li, J. Yang, J. Mater. Sci. Mater. Electron. (2018) 1–5.
[136] R. Klee, M.J. Aragón, R. Alcántara, J.L. Tirado, P. Lavela, Eur. J. Inorg. Chem. 2016 (2016) 3212–3218.
[137] P. Meister, H. Jia, J. Li, R. Kloepsch, M. Winter, T. Placke, Chem. Mater. 28 (2016) 7203–7217.
[138] J. Kasnatscheew, T. Placke, B. Streipert, S. Rothermel, R. Wagner, P. Meister, I.C. Laskovic, M. Winter, J. Electrochem. Soc. 164 (2017) A2479–A2486.
[139] J.P. Meyers, M. Doyle, R.M. Darling, J. Newman, J. Electrochem. Soc. 147 (2000) 2930–2940.
[140] M. Dollé, F. Orsini, A.S. Gozdz, J.-M. Tarascon, J. Electrochem. Soc. 148 (2001) A851–A857.
[141] K.-H. Ha, S.H. Woo, D. Mok, N.-S. Choi, Y. Park, S.M. Oh, Y. Kim, J. Kim, J. Lee, L.F. Nazar, K.T. Lee, Adv. Energy Mater. 3 (2013) 770–776.

[142] R. Ruffo, R. Fathi, D.J. Kim, Y.H. Jung, C.M. Mari, D.K. Kim, Electrochim. Acta 108 (2013) 575–582.
[143] A. Jänes, L. Permann, M. Arulepp, E. Lust, J. Electroanal. Chem. 569 (2004) 257–269.
[144] A. Laheäär, A. Jänes, E. Lust, Electrochim. Acta 56 (2011) 9048–9055.
[145] S.S. Zhang, K. Xu, T.R. Jow, Electrochim. Acta 51 (2006) 1636–1640.
[146] S. Zhang, M.S. Ding, K. Xu, J. Allen, T.R. Jow, Electrochem. Solid-State Lett. 4 (2001) A206–A208.
[147] S.S. Zhang, K. Xu, T.R. Jow, Electrochem. Solid-State Lett. 5 (2002) A92–A94.
[148] S.S. Zhang, K. Xu, T.R. Jow, Electrochim. Acta 49 (2004) 1057–1061.
[149] A. Laheäär, A. Jänes, E. Lust, Electrochim. Acta 82 (2012) 309–313.
[150] A. Laheäär, A. Jänes, E. Lust, Electrochim. Acta 125 (2014) 482–487.
[151] J. Ribeiro-Soares, M.E. Oliveros, C. Garin, M.V. David, L.G.P. Martins, C.A. Almeida, E.H. Martins-Ferreira, K. Takai, T. Enoki, R. Magalhães-Paniago, A. Malachias, A. Jorio, B.S. Archanjo, C.A. Achete, L.G. Cançado, Carbon 95 (2015) 646–652.
[152] P.B. Balbuena, Y. Wang, Lithium-Ion Batteries: Solid-Electrolyte Interphase, Imperial College Press, 2004.
[153] P.J.F. Harris, Z. Liu, K. Suenaga, J. Phys. Condens. Matter 20 (2008) 362201.
[154] J. Zou, C. Sole, N.E. Drewett, M. Velický, L.J. Hardwick, J. Phys. Chem. Lett. 7 (2016) 4291–4296.
[155] D.E. Nixon, G.S. Parry, J. Phys. C Solid State Phys. 2 (1969) 1732–1741.
[156] C.T. Chan, W.A. Kamitakahara, K.M. Ho, P.C. Eklund, Phys. Rev. Lett. 58 (1987) 1528–1531.
[157] M.Á. Muñoz-Márquez, D. Saurel, J.L. Gómez-Cámer, M. Casas-Cabanas, E. Castillo-Martínez, T. Rojo, Adv. Energy Mater. (2017) 1700463.
[158] Y. Liu, B.V. Merinov, W.A. Goddard, Proc. Natl. Acad. Sci. 113 (2016) 3735–3739.
[159] R.D. Shannon, Acta Crystallogr. A 32 (1976) 751–767.

9. SUMMARY IN ESTONIAN

Glükoosist sünteesitud süsinikelektroodi materjali karakteriseerimine naatrium-ioon akumulaatoris

Antud töös keskenduti glükoosist hüdrotermilisel karboniseerimisel ja kõrgtemperatuursel järeltöötlusel sünteesitud *hard carbon* tüüpi süsinikmaterjali (GDHC) elektrokeemilisele karakteriseerimisele metall-ioon aku poolelementides. Elektroodi pinnal toimuvate elektrokeemiliste protsesside uurimiseks kasutati Li^+, Na^+ ja K^+ soolasid ning erinevaid solvendisegusid. Kasutati järgmisi solvente: etüleenkarbonaat (EC), propüleenkarbonaat (PC), dimetüülkarbonaat (DMC) ja dietüülkarbonaat (DEC). Tsüklilist voltamperomeetriat (CV), konstantse voolu meetodit (GCD) ning elektrokeemilist impedantsspektroskoopiat (EIS) koos ekvivalent skeemi modelleerimisega kasutati poolelementide elektrokeemiliseks karaketeriseerimiseks. Elektrokeemiliselt tsükleeritud elektroodide *ex situ* uurimiseks kasutati Raman spektroskoopiat, laser ablatsioon induktiivsidestatud plasma massi spektromeetriat (LA-ICP-MS) ja lennuaja sekundaarioon massispektromeetriat (TOF-SIMS). Samuti kasutati *operando* röntgen hajumise meetodit koos paari jaotusfunktsiooni analüüsiga, et tuvastada naatriumi ja liitiumiga laadimisel toimuvad struktuursed muudatused GDHC materjalis.

Parimad konstantse vooluga (50 mA g^{-1}) laadimise tulemused saavutati kasutades 1 M $NaPF_6$ EC:PC (1:1) elektrolüüti – mahutavus 350 mAh g^{-1}, millest 175 mAh g^{-1} platool. Sama solventseguga, kuid $LiPF_6$-ga mõõdetud mahutavus oli 375 mAh g^{-1}, kuid samas oli platoomahutavus limiteeritud 100 mAh g^{-1}-ni. Mõõtmistulemustest järeldub, et PC kasutamine parandab adsorptsiooni mikropoorides, mida seostatakse platooalaga konstantse voolu kõveratel, sest platood ei olnud näha $LiPF_6$ EC:DMC (1:1) elektrolüüdi korral ning $NaPF_6$ EC:DMC (1:1) korral on platooala märksa lühem.

EIS katsed laias potentsiaali vahemikus ja ekvivalentskeemiga modelleerimine näitasid, et 1 M $LiPF_6$ EC:DMC (1:1) moodustab paksema ja stabiilsema SEI-kihi kui 1 M $NaPF_6$ EC:DMC (1:1), 0.8 M KPF_6 EC:DEC (1:1) või 1 M $NaClO_4$ PC, sest modelleerimisest saadud R_{SEI} ja C_{SEI} väärtused olid märksa kõrgemad, vastavalt ~25 Ω cm^2 ja 4.5 μF cm^{-2}. Madal R_{SEI} (6 Ω cm^2) ja suhteliselt kõrge C_{SEI} väärtus (3 μF cm^{-2}) 1 M $NaClO_4$ PC korral viitab PC ko-interkaleerumisele grafiitsetesse domeenidesse või sellele, et $NaClO_4$ PC laguproduktid on parema lahustuvusega kui $LiPF_6$ EC:DMC korral.

Ex-situ LA-ICP-MS mõõtmised näitasid 375-kordset Na sisalduse kasvu võrreldes elektrolüüdis leotatud elektroodiga.

Raman spektroskoopia mõõtmistulemustest arvutatud I_D/I_G parameetri väärtuste võrdlus Li ja Na-ga laadimise järel viitas väikestele struktuursetele muudatustele süsinikus. Samas TOF-SIMS pinnauuring Li ja Na-ga laetud elektroodidest näitas, et Na puhul on laguproduktid rohkem anorgaanilist laadi kui Li korral. Samuti sisaldas Li-ga laetud elektroodi massispekter märksa enam fragmente kui Na korral, mis viitab Na laguproduktide paremale lahustuvusele elektrolüüdis.

Operando röntgen hajumise mõõtmised Li ja Na poolelementides näitasid, et Na sisestumine materjali põhjustab grafeeni kihis C–C sideme pikenemist, mis viitab grafeenikihtide kõverdumisele. Na on Li-st 20% suurem, kuid põhjustas grafeenitasandi parameeterite 60%-list kasvu, mis võib olla põhjustatud delokaliseeritud elektroniülekandest ümbruses asuvatele benseeni tuumadele.

Selleks, et uurida GDHC käitumist täiselemendis, tõsteti sünteesi temperatuuri 1400–1600 °C vahemikku ning sünteesiti positiivse elektroodi materjal $Na_3V_2(PO_4)_3$ (NVP) kasutades glütsiin-nitraat leeksünteesi meetodit. Mõlemaid materjale uuriti esmalt poolelementides, mille järel parimatest komplekteeriti täis GDHC||NVP elemendid.

Võrreldes GDHC 1100-ga on GDHC 1400–1600 materjalidel kõrgem kuloniline efektiivsus (80%) ja pöörduvad mahutavused (300 mAh g^{-1}) sh platoomahutavus 200 mAh g^{-1}. Juhtivuslisandi (Super P) vähendamine 15 massiprotsendi pealt 4%-ni tõstis kulonilise efektiivsuse 85%-ni. Parimad tulemused saavutati materjaliga GDHC 1400b (vähendatud Super P) – pöörduv mahutavus 272 mAh g^{-1}, millest platoomahutavus 155 mAh g^{-1}.

NVP sünteesimiseks kasutati mitut erinevat prekursori valmistamise meetodit. Parimad tulemused saavutati kasutades prekursori pihustamise meetodit – 102 mAh g^{-1} voolul C/20 sünteesi koguste suurendamisega saavutati ka kõrge võimsusega materjal – 60 mAh g^{-1} voolul 20C. GDHC||NVP täiselement saavutas 80 mAh g^{-1} NVP massi kohta, millest 60 mAh g^{-1} potentsiaalil 3.3 V ehk platooalas. Erienergiaks arvutati 189 Wh kg^{-1} ja energiatiheduseks 104 Wh dm^{-3}. 80 tsükli järel, mis hõlmas ka mõõtmisi kõrgetel vooludel vahemikus C/20 kuni 10C, oli element säilitanud 65 mAh g^{-1}, kulonilise efektiivsusega 99.7%.

Saadud tulemused näitavad, et edasised Na salvestamise uuringud *hard carbon* tüüpi süsinikesse on väga olulised selleks, et arendada kõrge platoomahutavusega negatiivseid elektroode, mis omakorda võimaldab komplekteerida kõrge energiatihedusega Na-ioon akusid. Pöördumatu mahutavuse vähendamine ja SEI kihi stabiilsuse suurendamine on põhilised väljakutsed, mis vajavad lahendust enne Na-ioon akude täielikku kommertsialiseerimist.

10. ACKNOWLEDGEMENTS

Firstly, I would like to thank my supervisors Prof. Enn Lust and Dr. Alar Jänes. Enn, you have provided a great example of how to approach new challenges – tackle them head-on. The fact that you have shared your knowledge of the energy industry and the politics in academia and elsewhere has given me a broader view of science and problems related to it. I am sincerely grateful that you have entrusted me with taking up a new research discipline in our group. Alar, the publication list might have been a lot shorter if it wasn't for your frequent reminders to sum things up after all, there is always one more experiment that could be conducted. I appreciate your help with supplying the necessary equipment, chemicals and with preparing the manuscripts.

A big thanks to Dr. Rainer Küngas for being a role model, a mentor and for providing opportunities for collaboration with partners abroad. Dr. Ann Laheäär, my first supervisor, who set a great example as a scientist and showed what a wonderful world lies ahead in the scientific community.

I would like to thank Dr. Heisi Kurig, Dr. Rasmus Palm, Ms. Miriam Koppel for conducting gas sorption measurements of the materials I worked with and for their help in interpreting these results; Dr. Tavo Romann for Raman measurements; Mr. Jaan Aruväli for XRD and XRF measurements and for the detailed crystallographic analysis he conducted; Dr. Thomas Thomberg and Mr. Meelis Härmas for synthesizing the HTC precursor and GDHC 1100 material for me; Prof. Kyosti Kontturi from Aalto University for the TEM experiments; Prof. Poul Norby and Ms. Jette Katja Mathiesen from Danish Technical University for an awesome collaboration on *operando* total X-ray scattering experiments; Dr. Päärn Paiste for conducting LA-ICP-MS measurements; Dr. Priit Möller for TOF-SIMS measurements.

Special thanks to Mr. Rait Kanarbik for all the technical support from computers and instruments to clever hacks in the lab; Mrs. Riinu Härmas for helping me with data analysis and scripting; Dr. Ove Oll for challenging my understanding of the fundamentals and providing inspiration for new work; Dr. Vladislav Ivaništšev for helping me appreciate the value of theoretical calculations despite my experimental focus; Dr. Gunnar Nurk for interesting discussions; Dr. Olivier Crosnier for teaching me the basics of battery research during my internship at Institut des Matériaux Jean Rouxel Nantes; Ove Korjus, Martin Maide and Alar Heinsaar for making work fun. I would like to thank all my colleagues for a great company, interesting discussions and good advice.

From the institute of chemistry, I would like to thank Prof. Ivo Leito for setting an example in didactics with his masterful lectures in analytical chemistry that has helped me to become a better teacher and science communicator; Prof. Mati Karelson for motivating lectures on technology transfer, giving a glimpse into the world outside of academia and inspiring to dream bigger and Dr. Lilli Paama for providing funding from the graduate school for my travel costs related to participation at international conferences.

I would not be where I am today without the love and support of my family, especially my wife Eglit, who has stood by my side all these years and continues to support my scientific curiosity and ambitions.

This research was supported by the EU through the European Regional Development Fund (Centers of Excellence, TK141 2014-2020.4.01.15-0011 and TK117 3.2.0101-0030, TeRa project SLOKT12026T, Higher education specialization stipends in smart specialization growth areas 2014-2020.4.02.16-0026, Graduate School of Functional materials and technologies in University of Tartu and NAMUR project 3.2.0304.12-0397). This work was partially supported by Estonian Research Council Institutional Research Grant IUT20−13, ETF9184 and personal research grants PUT55 and PUT1033.

Participation at scientific conferences was supported by national scholarship program Kristjan Jaak, which is funded and managed by Archimedes Foundation in collaboration with the Estonian Ministry of Education and Research.

11. PUBLICATIONS

CURRICULUM VITAE

Name:	Ronald Väli
Date of birth:	February 9, 1989
Citizenship:	Estonian
Contact:	Institute of Chemistry, University of Tartu Ravila 14a, 50411, Tartu, Estonia
E-mail:	ronaldvaeli@gmail.com

Education:

2015−	University of Tartu, Institute of Chemistry, PhD student
2013−2015	University of Tartu – Master's degree in Chemistry
2010−2013	University of Tartu – Bachelor's degree in Chemistry
1996−2008	Tallinn Audentes Private School

Professional employment:

2014−	University of Tartu, Institute of Chemistry, laboratorian
2014	University of Nantes, Institut des Materiaux Jean Rouxel, intern
2012−2014	University of Tartu, Institute of Chemistry, laboratorian

Awards:

2016	National student research contest, 1st prize in natural sciences and technology, MSc level

List of publications:

1. **R. Väli**, J. Aruväli, M. Härmas, A. Jänes, E. Lust, Glycine-nitrate process for synthesis of Na3V2(PO4)3 cathode material and optimization of glucose-derived hard carbon anode material for characterization in full cells, Batteries (2019) under review.
2. J. K. Mathiesen, **R. Väli**, M. Härmas, E. Lust, J. F. von Bülow, K. M. Ø. Jensen, P. Norby, Following the In-plane Disorder of Sodiated Hard Carbon through Operando Total Scattering, J. Mater. Chem. A 7 (2019) 11709.
3. T. Thomberg, **R. Väli**, J. Eskusson, T. Romann, A. Jänes, Potassium Salts Based Non-Aqueous Electrolytes for Electrical Double Layer Capacitors: A Comparison with LiPF6 and NaPF6 Based Electrolytes. J. Electrochem. Soc., 165 (2018) A3862.
4. R. Härmas, R. Palm, M. Härmas, M. Pohl, H. Kurig, I. Tallo, E. Tee, I. Vaas, **R. Väli**, T. Romann, O. Oll, R. Kanarbik, K. Liivand, J. Eskusson, J. Kruusma, T. Thomberg, A. Jänes, P. Miidla, E. Lust, Influence of porosity parameters and electrolyte chemical composition on the power densities of non-aqueous and ionic liquid based supercapacitors, Electrochim. Acta. 283 (2018) 931–948.

5. R. Palm, H. Kurig, T. Romann, U. Joost, R. Kanarbik, **R. Väli**, I. Tallo, T. Thomberg, A. Jänes, E. Lust, Application of Some Carbon Fabrics as Outstanding Supercapacitor Electrode Materials in Acetonitrile Based Electrolyte, J. Electrochem. Soc. 164 (2017) A453–A460.
6. **R. Väli**, A. Jänes, T. Thomberg, E. Lust, Synthesis and characterization of D-glucose derived nanospheric hard carbon negative electrodes for lithium- and sodium-ion batteries, Electrochim. Acta. 253 (2017) 536–544.
7. **R. Väli**, A. Jänes, E. Lust, Alkali-Metal Insertion Processes on Nanospheric Hard Carbon Electrodes: An Electrochemical Impedance Spectroscopy Study, J. Electrochem. Soc. 164 (2017) E3429–E3437.
8. **R. Väli**, A. Jänes, T. Thomberg, E. Lust, D-Glucose Derived Nanospheric Hard Carbon Electrodes for Room-Temperature Sodium-Ion Batteries, J. Electrochem. Soc. 163 (2016) A1619–A1626.
9. **R. Väli**, A. Jänes, E. Lust, Vinylene Carbonate as Co-Solvent for Low-Temperature Mixed Electrolyte Based Supercapacitors. J. Electrochem. Soc., 163 (2016) A851−A857.
10. **R. Väli**, P. Möller, A. Jänes, Synthesis and Characterization of Na3V2(PO4)2F3 Based Cathode Material for Sodium Ion Batteries. ECS Transactions, 39 (2015) 27−36.
11. **R. Väli**, A. Laheäär, A. Jänes, E. Lust, Characteristics of non-aqueous quaternary solvent mixture and Na-salts based supercapacitor electrolytes in a wide temperature range, Electrochim. Acta, 121 (2014) 294−300.

ELULOOKIRJELDUS

Nimi: Ronald Väli
Sünniaeg: 9. veebruar 1989
Kodakondsus: Eesti
Kontakt: Keemia instituut, Tartu Ülikool
Ravila 14a, 50411, Tartu, Eesti
E-post: ronaldvaeli@gmail.com

Hariduskäik:
2015− Tartu Ülikool, keemia instituut, doktorant
2013−2015 Tartu Ülikool – *M.Sc* keemia erialal
2010−2013 Tartu Ülikool – *B.Sc* keemia erialal
1996−2008 Tallinna Audentese Erakool

Teenistuskäik:
2014− Tartu Ülikool, keemia instituut, laborant
2014 Nantes'i Ülikool, Institut des Materiaux Jean Rouxel, praktikant
2012−2014 Tartu Ülikool, keemia instituut, laborant

Auhinnad:
2016 Üliõpilastööde riiklik konkurss, loodusteaduste ja tehnika valdkond, magistri üliõpilaste aste, I preemia

Teaduspublikatsioonid:

12. **R. Väli**, J. Aruväli, M. Härmas, A. Jänes, E. Lust, Glycine-nitrate process for synthesis of Na3V2(PO4)3 cathode material and optimization of glucose-derived hard carbon anode material for characterization in full cells, Batteries (2019) retsenseerimisel.
13. J. K. Mathiesen, **R. Väli**, M. Härmas, E. Lust, J. F. von Bülow, K. M. Ø. Jensen, P. Norby, Following the In-plane Disorder of Sodiated Hard Carbon through Operando Total Scattering, J. Mater. Chem. A 7 (2019) 11709.
14. T. Thomberg, **R. Väli**, J. Eskusson, T. Romann, A. Jänes, Potassium Salts Based Non-Aqueous Electrolytes for Electrical Double Layer Capacitors: A Comparison with LiPF6 and NaPF6 Based Electrolytes. J. Electrochem. Soc., 165 (2018) A3862.
15. R. Härmas, R. Palm, M. Härmas, M. Pohl, H. Kurig, I. Tallo, E. Tee, I. Vaas, **R. Väli**, T. Romann, O. Oll, R. Kanarbik, K. Liivand, J. Eskusson, J. Kruusma, T. Thomberg, A. Jänes, P. Miidla, E. Lust, Influence of porosity parameters and electrolyte chemical composition on the power densities of non-aqueous and ionic liquid based supercapacitors, Electrochim. Acta. 283 (2018) 931–948.

16. R. Palm, H. Kurig, T. Romann, U. Joost, R. Kanarbik, **R. Väli**, I. Tallo, T. Thomberg, A. Jänes, E. Lust, Application of Some Carbon Fabrics as Outstanding Supercapacitor Electrode Materials in Acetonitrile Based Electrolyte, J. Electrochem. Soc. 164 (2017) A453–A460.
17. **R. Väli**, A. Jänes, T. Thomberg, E. Lust, Synthesis and characterization of D-glucose derived nanospheric hard carbon negative electrodes for lithium- and sodium-ion batteries, Electrochim. Acta. 253 (2017) 536–544.
18. **R. Väli**, A. Jänes, E. Lust, Alkali-Metal Insertion Processes on Nanospheric Hard Carbon Electrodes: An Electrochemical Impedance Spectroscopy Study, J. Electrochem. Soc. 164 (2017) E3429–E3437.
19. **R. Väli**, A. Jänes, T. Thomberg, E. Lust, D-Glucose Derived Nanospheric Hard Carbon Electrodes for Room-Temperature Sodium-Ion Batteries, J. Electrochem. Soc. 163 (2016) A1619–A1626.
20. **R. Väli**, A. Jänes, E. Lust, Vinylene Carbonate as Co-Solvent for Low-Temperature Mixed Electrolyte Based Supercapacitors. J. Electrochem. Soc., 163 (2016) A851−A857.
21. **R. Väli**, P. Möller, A. Jänes, Synthesis and Characterization of Na3V2(PO4)2F3 Based Cathode Material for Sodium Ion Batteries. ECS Transactions, 39 (2015) 27−36.
22. **R. Väli**, A. Laheäär, A. Jänes, E. Lust, Characteristics of non-aqueous quaternary solvent mixture and Na-salts based supercapacitor electrolytes in a wide temperature range, Electrochim. Acta, 121 (2014) 294−300.

DISSERTATIONES CHIMICAE UNIVERSITATIS TARTUENSIS

1. **Toomas Tamm.** Quantum-chemical simulation of solvent effects. Tartu, 1993, 110 p.
2. **Peeter Burk.** Theoretical study of gas-phase acid-base equilibria. Tartu, 1994, 96 p.
3. **Victor Lobanov.** Quantitative structure-property relationships in large descriptor spaces. Tartu, 1995, 135 p.
4. **Vahur Mäemets.** The ^{17}O and ^{1}H nuclear magnetic resonance study of H_2O in individual solvents and its charged clusters in aqueous solutions of electrolytes. Tartu, 1997, 140 p.
5. **Andrus Metsala.** Microcanonical rate constant in nonequilibrium distribution of vibrational energy and in restricted intramolecular vibrational energy redistribution on the basis of slater's theory of unimolecular reactions. Tartu, 1997, 150 p.
6. **Uko Maran.** Quantum-mechanical study of potential energy surfaces in different environments. Tartu, 1997, 137 p.
7. **Alar Jänes.** Adsorption of organic compounds on antimony, bismuth and cadmium electrodes. Tartu, 1998, 219 p.
8. **Kaido Tammeveski.** Oxygen electroreduction on thin platinum films and the electrochemical detection of superoxide anion. Tartu, 1998, 139 p.
9. **Ivo Leito.** Studies of Brønsted acid-base equilibria in water and non-aqueous media. Tartu, 1998, 101 p.
10. **Jaan Leis.** Conformational dynamics and equilibria in amides. Tartu, 1998, 131 p.
11. **Toonika Rinken.** The modelling of amperometric biosensors based on oxidoreductases. Tartu, 2000, 108 p.
12. **Dmitri Panov.** Partially solvated Grignard reagents. Tartu, 2000, 64 p.
13. **Kaja Orupõld.** Treatment and analysis of phenolic wastewater with microorganisms. Tartu, 2000, 123 p.
14. **Jüri Ivask.** Ion Chromatographic determination of major anions and cations in polar ice core. Tartu, 2000, 85 p.
15. **Lauri Vares.** Stereoselective Synthesis of Tetrahydrofuran and Tetrahydropyran Derivatives by Use of Asymmetric Horner-Wadsworth-Emmons and Ring Closure Reactions. Tartu, 2000, 184 p.
16. **Martin Lepiku.** Kinetic aspects of dopamine D_2 receptor interactions with specific ligands. Tartu, 2000, 81 p.
17. **Katrin Sak.** Some aspects of ligand specificity of P2Y receptors. Tartu, 2000, 106 p.
18. **Vello Pällin.** The role of solvation in the formation of iotsitch complexes. Tartu, 2001, 95 p.
19. **Katrin Kollist.** Interactions between polycyclic aromatic compounds and humic substances. Tartu, 2001, 93 p.

20. **Ivar Koppel.** Quantum chemical study of acidity of strong and superstrong Brønsted acids. Tartu, 2001, 104 p.
21. **Viljar Pihl.** The study of the substituent and solvent effects on the acidity of OH and CH acids. Tartu, 2001, 132 p.
22. **Natalia Palm.** Specification of the minimum, sufficient and significant set of descriptors for general description of solvent effects. Tartu, 2001, 134 p.
23. **Sulev Sild.** QSPR/QSAR approaches for complex molecular systems. Tartu, 2001, 134 p.
24. **Ruslan Petrukhin.** Industrial applications of the quantitative structure-property relationships. Tartu, 2001, 162 p.
25. **Boris V. Rogovoy.** Synthesis of (benzotriazolyl)carboximidamides and their application in relations with *N*- and *S*-nucleophyles. Tartu, 2002, 84 p.
26. **Koit Herodes.** Solvent effects on UV-vis absorption spectra of some solvatochromic substances in binary solvent mixtures: the preferential solvation model. Tartu, 2002, 102 p.
27. **Anti Perkson.** Synthesis and characterisation of nanostructured carbon. Tartu, 2002, 152 p.
28. **Ivari Kaljurand.** Self-consistent acidity scales of neutral and cationic Brønsted acids in acetonitrile and tetrahydrofuran. Tartu, 2003, 108 p.
29. **Karmen Lust.** Adsorption of anions on bismuth single crystal electrodes. Tartu, 2003, 128 p.
30. **Mare Piirsalu.** Substituent, temperature and solvent effects on the alkaline hydrolysis of substituted phenyl and alkyl esters of benzoic acid. Tartu, 2003, 156 p.
31. **Meeri Sassian.** Reactions of partially solvated Grignard reagents. Tartu, 2003, 78 p.
32. **Tarmo Tamm.** Quantum chemical modelling of polypyrrole. Tartu, 2003. 100 p.
33. **Erik Teinemaa.** The environmental fate of the particulate matter and organic pollutants from an oil shale power plant. Tartu, 2003. 102 p.
34. **Jaana Tammiku-Taul.** Quantum chemical study of the properties of Grignard reagents. Tartu, 2003. 120 p.
35. **Andre Lomaka.** Biomedical applications of predictive computational chemistry. Tartu, 2003. 132 p.
36. **Kostyantyn Kirichenko.** Benzotriazole – Mediated Carbon–Carbon Bond Formation. Tartu, 2003. 132 p.
37. **Gunnar Nurk.** Adsorption kinetics of some organic compounds on bismuth single crystal electrodes. Tartu, 2003, 170 p.
38. **Mati Arulepp.** Electrochemical characteristics of porous carbon materials and electrical double layer capacitors. Tartu, 2003, 196 p.
39. **Dan Cornel Fara.** QSPR modeling of complexation and distribution of organic compounds. Tartu, 2004, 126 p.
40. **Riina Mahlapuu.** Signalling of galanin and amyloid precursor protein through adenylate cyclase. Tartu, 2004, 124 p.

41. **Mihkel Kerikmäe.** Some luminescent materials for dosimetric applications and physical research. Tartu, 2004, 143 p.
42. **Jaanus Kruusma.** Determination of some important trace metal ions in human blood. Tartu, 2004, 115 p.
43. **Urmas Johanson.** Investigations of the electrochemical properties of polypyrrole modified electrodes. Tartu, 2004, 91 p.
44. **Kaido Sillar.** Computational study of the acid sites in zeolite ZSM-5. Tartu, 2004, 80 p.
45. **Aldo Oras.** Kinetic aspects of dATPαS interaction with P2Y_1 receptor. Tartu, 2004, 75 p.
46. **Erik Mölder.** Measurement of the oxygen mass transfer through the air-water interface. Tartu, 2005, 73 p.
47. **Thomas Thomberg.** The kinetics of electroreduction of peroxodisulfate anion on cadmium (0001) single crystal electrode. Tartu, 2005, 95 p.
48. **Olavi Loog.** Aspects of condensations of carbonyl compounds and their imine analogues. Tartu, 2005, 83 p.
49. **Siim Salmar.** Effect of ultrasound on ester hydrolysis in aqueous ethanol. Tartu, 2006, 73 p.
50. **Ain Uustare.** Modulation of signal transduction of heptahelical receptors by other receptors and G proteins. Tartu, 2006, 121 p.
51. **Sergei Yurchenko.** Determination of some carcinogenic contaminants in food. Tartu, 2006, 143 p.
52. **Kaido Tämm.** QSPR modeling of some properties of organic compounds. Tartu, 2006, 67 p.
53. **Olga Tšubrik.** New methods in the synthesis of multisubstituted hydrazines. Tartu. 2006, 183 p.
54. **Lilli Sooväli.** Spectrophotometric measurements and their uncertainty in chemical analysis and dissociation constant measurements. Tartu, 2006, 125 p.
55. **Eve Koort.** Uncertainty estimation of potentiometrically measured ph and pK_a values. Tartu, 2006, 139 p.
56. **Sergei Kopanchuk.** Regulation of ligand binding to melanocortin receptor subtypes. Tartu, 2006, 119 p.
57. **Silvar Kallip.** Surface structure of some bismuth and antimony single crystal electrodes. Tartu, 2006, 107 p.
58. **Kristjan Saal.** Surface silanization and its application in biomolecule coupling. Tartu, 2006, 77 p.
59. **Tanel Tätte.** High viscosity $Sn(OBu)_4$ oligomeric concentrates and their applications in technology. Tartu, 2006, 91 p.
60. **Dimitar Atanasov Dobchev**. Robust QSAR methods for the prediction of properties from molecular structure. Tartu, 2006, 118 p.
61. **Hannes Hagu**. Impact of ultrasound on hydrophobic interactions in solutions. Tartu, 2007, 81 p.
62. **Rutha Jäger.** Electroreduction of peroxodisulfate anion on bismuth electrodes. Tartu, 2007, 142 p.

63. **Kaido Viht.** Immobilizable bisubstrate-analogue inhibitors of basophilic protein kinases: development and application in biosensors. Tartu, 2007, 88 p.
64. **Eva-Ingrid Rõõm.** Acid-base equilibria in nonpolar media. Tartu, 2007, 156 p.
65. **Sven Tamp.** DFT study of the cesium cation containing complexes relevant to the cesium cation binding by the humic acids. Tartu, 2007, 102 p.
66. **Jaak Nerut.** Electroreduction of hexacyanoferrate(III) anion on Cadmium (0001) single crystal electrode. Tartu, 2007, 180 p.
67. **Lauri Jalukse.** Measurement uncertainty estimation in amperometric dissolved oxygen concentration measurement. Tartu, 2007, 112 p.
68. **Aime Lust.** Charge state of dopants and ordered clusters formation in CaF_2:Mn and CaF_2:Eu luminophors. Tartu, 2007, 100 p.
69. **Iiris Kahn**. Quantitative Structure-Activity Relationships of environmentally relevant properties. Tartu, 2007, 98 p.
70. **Mari Reinik.** Nitrates, nitrites, N-nitrosamines and polycyclic aromatic hydrocarbons in food: analytical methods, occurrence and dietary intake. Tartu, 2007, 172 p.
71. **Heili Kasuk.** Thermodynamic parameters and adsorption kinetics of organic compounds forming the compact adsorption layer at Bi single crystal electrodes. Tartu, 2007, 212 p.
72. **Erki Enkvist.** Synthesis of adenosine-peptide conjugates for biological applications. Tartu, 2007, 114 p.
73. **Svetoslav Hristov Slavov**. Biomedical applications of the QSAR approach. Tartu, 2007, 146 p.
74. **Eneli Härk.** Electroreduction of complex cations on electrochemically polished Bi(*hkl*) single crystal electrodes. Tartu, 2008, 158 p.
75. **Priit Möller.** Electrochemical characteristics of some cathodes for medium temperature solid oxide fuel cells, synthesized by solid state reaction technique. Tartu, 2008, 90 p.
76. **Signe Viggor.** Impact of biochemical parameters of genetically different pseudomonads at the degradation of phenolic compounds. Tartu, 2008, 122 p.
77. **Ave Sarapuu.** Electrochemical reduction of oxygen on quinone-modified carbon electrodes and on thin films of platinum and gold. Tartu, 2008, 134 p.
78. **Agnes Kütt.** Studies of acid-base equilibria in non-aqueous media. Tartu, 2008, 198 p.
79. **Rouvim Kadis.** Evaluation of measurement uncertainty in analytical chemistry: related concepts and some points of misinterpretation. Tartu, 2008, 118 p.
80. **Valter Reedo.** Elaboration of IVB group metal oxide structures and their possible applications. Tartu, 2008, 98 p.
81. **Aleksei Kuznetsov.** Allosteric effects in reactions catalyzed by the cAMP-dependent protein kinase catalytic subunit. Tartu, 2009, 133 p.

82. **Aleksei Bredihhin.** Use of mono- and polyanions in the synthesis of multisubstituted hydrazine derivatives. Tartu, 2009, 105 p.
83. **Anu Ploom.** Quantitative structure-reactivity analysis in organosilicon chemistry. Tartu, 2009, 99 p.
84. **Argo Vonk.** Determination of adenosine A_{2A}- and dopamine D_1 receptor-specific modulation of adenylate cyclase activity in rat striatum. Tartu, 2009, 129 p.
85. **Indrek Kivi.** Synthesis and electrochemical characterization of porous cathode materials for intermediate temperature solid oxide fuel cells. Tartu, 2009, 177 p.
86. **Jaanus Eskusson.** Synthesis and characterisation of diamond-like carbon thin films prepared by pulsed laser deposition method. Tartu, 2009, 117 p.
87. **Marko Lätt.** Carbide derived microporous carbon and electrical double layer capacitors. Tartu, 2009, 107 p.
88. **Vladimir Stepanov.** Slow conformational changes in dopamine transporter interaction with its ligands. Tartu, 2009, 103 p.
89. **Aleksander Trummal.** Computational Study of Structural and Solvent Effects on Acidities of Some Brønsted Acids. Tartu, 2009, 103 p.
90. **Eerold Vellemäe.** Applications of mischmetal in organic synthesis. Tartu, 2009, 93 p.
91. **Sven Parkel.** Ligand binding to 5-HT_{1A} receptors and its regulation by Mg^{2+} and Mn^{2+}. Tartu, 2010, 99 p.
92. **Signe Vahur.** Expanding the possibilities of ATR-FT-IR spectroscopy in determination of inorganic pigments. Tartu, 2010, 184 p.
93. **Tavo Romann**. Preparation and surface modification of bismuth thin film, porous, and microelectrodes. Tartu, 2010, 155 p.
94. **Nadežda Aleksejeva.** Electrocatalytic reduction of oxygen on carbon nanotube-based nanocomposite materials. Tartu, 2010, 147 p.
95. **Marko Kullapere.** Electrochemical properties of glassy carbon, nickel and gold electrodes modified with aryl groups. Tartu, 2010, 233 p.
96. **Liis Siinor.** Adsorption kinetics of ions at Bi single crystal planes from aqueous electrolyte solutions and room-temperature ionic liquids. Tartu, 2010, 101 p.
97. **Angela Vaasa.** Development of fluorescence-based kinetic and binding assays for characterization of protein kinases and their inhibitors. Tartu 2010, 101 p.
98. **Indrek Tulp.** Multivariate analysis of chemical and biological properties. Tartu 2010, 105 p.
99. **Aare Selberg.** Evaluation of environmental quality in Northern Estonia by the analysis of leachate. Tartu 2010, 117 p.
100. **Darja Lavõgina.** Development of protein kinase inhibitors based on adenosine analogue-oligoarginine conjugates. Tartu 2010, 248 p.
101. **Laura Herm.** Biochemistry of dopamine D_2 receptors and its association with motivated behaviour. Tartu 2010, 156 p.

102. **Terje Raudsepp.** Influence of dopant anions on the electrochemical properties of polypyrrole films. Tartu 2010, 112 p.
103. **Margus Marandi.** Electroformation of Polypyrrole Films: *In-situ* AFM and STM Study. Tartu 2011, 116 p.
104. **Kairi Kivirand.** Diamine oxidase-based biosensors: construction and working principles. Tartu, 2011, 140 p.
105. **Anneli Kruve.** Matrix effects in liquid-chromatography electrospray mass-spectrometry. Tartu, 2011, 156 p.
106. **Gary Urb.** Assessment of environmental impact of oil shale fly ash from PF and CFB combustion. Tartu, 2011, 108 p.
107. **Nikita Oskolkov.** A novel strategy for peptide-mediated cellular delivery and induction of endosomal escape. Tartu, 2011, 106 p.
108. **Dana Martin.** The QSPR/QSAR approach for the prediction of properties of fullerene derivatives. Tartu, 2011, 98 p.
109. **Säde Viirlaid.** Novel glutathione analogues and their antioxidant activity. Tartu, 2011, 106 p.
110. **Ülis Sõukand.** Simultaneous adsorption of Cd^{2+}, Ni^{2+}, and Pb^{2+} on peat. Tartu, 2011, 124 p.
111. **Lauri Lipping.** The acidity of strong and superstrong Brønsted acids, an outreach for the "limits of growth": a quantum chemical study. Tartu, 2011, 124 p.
112. **Heisi Kurig.** Electrical double-layer capacitors based on ionic liquids as electrolytes. Tartu, 2011, 146 p.
113. **Marje Kasari.** Bisubstrate luminescent probes, optical sensors and affinity adsorbents for measurement of active protein kinases in biological samples. Tartu, 2012, 126 p.
114. **Kalev Takkis.** Virtual screening of chemical databases for bioactive molecules. Tartu, 2012, 122 p.
115. **Ksenija Kisseljova**. Synthesis of aza-β^3-amino acid containing peptides and kinetic study of their phosphorylation by protein kinase A. Tartu, 2012, 104 p.
116. **Riin Rebane.** Advanced method development strategy for derivatization LC/ESI/MS. Tartu, 2012, 184 p.
117. **Vladislav Ivaništšev.** Double layer structure and adsorption kinetics of ions at metal electrodes in room temperature ionic liquids. Tartu, 2012, 128 p.
118. **Irja Helm.** High accuracy gravimetric Winkler method for determination of dissolved oxygen. Tartu, 2012, 139 p.
119. **Karin Kipper.** Fluoroalcohols as Components of LC-ESI-MS Eluents: Usage and Applications. Tartu, 2012, 164 p.
120. **Arno Ratas.** Energy storage and transfer in dosimetric luminescent materials. Tartu, 2012, 163 p.
121. **Reet Reinart-Okugbeni**. Assay systems for characterisation of subtype-selective binding and functional activity of ligands on dopamine receptors. Tartu, 2012, 159 p.

122. **Lauri Sikk.** Computational study of the Sonogashira cross-coupling reaction. Tartu, 2012, 81 p.
123. **Karita Raudkivi.** Neurochemical studies on inter-individual differences in affect-related behaviour of the laboratory rat. Tartu, 2012, 161 p.
124. **Indrek Saar.** Design of GalR2 subtype specific ligands: their role in depression-like behavior and feeding regulation. Tartu, 2013, 126 p.
125. **Ann Laheäär.** Electrochemical characterization of alkali metal salt based non-aqueous electrolytes for supercapacitors. Tartu, 2013, 127 p.
126. **Kerli Tõnurist.** Influence of electrospun separator materials properties on electrochemical performance of electrical double-layer capacitors. Tartu, 2013, 147 p.
127. **Kaija Põhako-Esko.** Novel organic and inorganic ionogels: preparation and characterization. Tartu, 2013, 124 p.
128. **Ivar Kruusenberg.** Electroreduction of oxygen on carbon nanomaterial-based catalysts. Tartu, 2013, 191 p.
129. **Sander Piiskop.** Kinetic effects of ultrasound in aqueous acetonitrile solutions. Tartu, 2013, 95 p.
130. **Ilona Faustova**. Regulatory role of L-type pyruvate kinase N-terminal domain. Tartu, 2013, 109 p.
131. **Kadi Tamm.** Synthesis and characterization of the micro-mesoporous anode materials and testing of the medium temperature solid oxide fuel cell single cells. Tartu, 2013, 138 p.
132. **Iva Bozhidarova Stoyanova-Slavova.** Validation of QSAR/QSPR for regulatory purposes. Tartu, 2013, 109 p.
133. **Vitali Grozovski**. Adsorption of organic molecules at single crystal electrodes studied by *in situ* STM method. Tartu, 2014, 146 p.
134. **Santa Veikšina**. Development of assay systems for characterisation of ligand binding properties to melanocortin 4 receptors. Tartu, 2014, 151 p.
135. **Jüri Liiv.** PVDF (polyvinylidene difluoride) as material for active element of twisting-ball displays. Tartu, 2014, 111 p.
136. **Kersti Vaarmets.** Electrochemical and physical characterization of pristine and activated molybdenum carbide-derived carbon electrodes for the oxygen electroreduction reaction. Tartu, 2014, 131 p.
137. **Lauri Tõntson**. Regulation of G-protein subtypes by receptors, guanine nucleotides and Mn^{2+}. Tartu, 2014, 105 p.
138. **Aiko Adamson.** Properties of amine-boranes and phosphorus analogues in the gas phase. Tartu, 2014, 78 p.
139. **Elo Kibena**. Electrochemical grafting of glassy carbon, gold, highly oriented pyrolytic graphite and chemical vapour deposition-grown graphene electrodes by diazonium reduction method. Tartu, 2014, 184 p.
140. **Teemu Näykki.** Novel Tools for Water Quality Monitoring – From Field to Laboratory. Tartu, 2014, 202 p.
141. **Karl Kaupmees.** Acidity and basicity in non-aqueous media: importance of solvent properties and purity. Tartu, 2014, 128 p.

142. **Oleg Lebedev**. Hydrazine polyanions: different strategies in the synthesis of heterocycles. Tartu, 2015, 118 p.
143. **Geven Piir.** Environmental risk assessment of chemicals using QSAR methods. Tartu, 2015, 123 p.
144. **Olga Mazina.** Development and application of the biosensor assay for measurements of cyclic adenosine monophosphate in studies of G protein-coupled receptor signalinga. Tartu, 2015, 116 p.
145. **Sandip Ashokrao Kadam.** Anion receptors: synthesis and accurate binding measurements. Tartu, 2015, 116 p.
146. **Indrek Tallo.** Synthesis and characterization of new micro-mesoporous carbide derived carbon materials for high energy and power density electrical double layer capacitors. Tartu, 2015, 148 p.
147. **Heiki Erikson.** Electrochemical reduction of oxygen on nanostructured palladium and gold catalysts. Tartu, 2015, 204 p.
148. **Erik Anderson.** *In situ* Scanning Tunnelling Microscopy studies of the interfacial structure between Bi(111) electrode and a room temperature ionic liquid. Tartu, 2015, 118 p.
149. **Girinath G. Pillai.** Computational Modelling of Diverse Chemical, Biochemical and Biomedical Properties. Tartu, 2015, 140 p.
150. **Piret Pikma.** Interfacial structure and adsorption of organic compounds at Cd(0001) and Sb(111) electrodes from ionic liquid and aqueous electrolytes: an *in situ* STM study. Tartu, 2015, 126 p.
151. **Ganesh babu Manoharan.** Combining chemical and genetic approaches for photoluminescence assays of protein kinases. Tartu, 2016, 126 p.
152. **Carolin Siimenson**. Electrochemical characterization of halide ion adsorption from liquid mixtures at Bi(111) and pyrolytic graphite electrode surface. Tartu, 2016, 110 p.
153. **Asko Laaniste.** Comparison and optimisation of novel mass spectrometry ionisation sources. Tartu, 2016, 156 p.
154. **Hanno Evard.** Estimating limit of detection for mass spectrometric analysis methods. Tartu, 2016, 224 p.
155. **Kadri Ligi.** Characterization and application of protein kinase-responsive organic probes with triplet-singlet energy transfer. Tartu, 2016, 122 p.
156. **Margarita Kagan.** Biosensing penicillins' residues in milk flows. Tartu, 2016, 130 p.
157. **Marie Kriisa.** Development of protein kinase-responsive photoluminescent probes and cellular regulators of protein phosphorylation. Tartu, 2016, 106 p.
158. **Mihkel Vestli.** Ultrasonic spray pyrolysis deposited electrolyte layers for intermediate temperature solid oxide fuel cells. Tartu, 2016, 156 p.
159. **Silver Sepp**. Influence of porosity of the carbide-derived carbon on the properties of the composite electrocatalysts and characteristics of polymer electrolyte fuel cells. Tartu, 2016, 137 p.
160. **Kristjan Haav**. Quantitative relative equilibrium constant measurements in supramolecular chemistry. Tartu, 2017, 158 p.

161. **Anu Teearu**. Development of MALDI-FT-ICR-MS methodology for the analysis of resinous materials. Tartu, 2017, 205 p.
162. **Taavi Ivan**. Bifunctional inhibitors and photoluminescent probes for studies on protein complexes. Tartu, 2017, 140 p.
163. **Maarja-Liisa Oldekop**. Characterization of amino acid derivatization reagents for LC-MS analysis. Tartu, 2017, 147 p.
164. **Kristel Jukk**. Electrochemical reduction of oxygen on platinum- and palladium-based nanocatalysts. Tartu, 2017, 250 p.
165. **Siim Kukk**. Kinetic aspects of interaction between dopamine transporter and *N*-substituted nortropane derivatives. Tartu, 2017, 107 p.
166. **Birgit Viira**. Design and modelling in early drug development in targeting HIV-1 reverse transcriptase and Malaria. Tartu, 2017, 172 p.
167. **Rait Kivi**. Allostery in cAMP dependent protein kinase catalytic subunit. Tartu, 2017, 115 p.
168. **Agnes Heering**. Experimental realization and applications of the unified acidity scale. Tartu, 2017, 123 p.
169. **Delia Juronen**. Biosensing system for the rapid multiplex detection of mastitis-causing pathogens in milk. Tartu, 2018, 85 p.
170. **Hedi Rahnel.** ARC-inhibitors: from reliable biochemical assays to regulators of physiology of cells. Tartu, 2018, 176 p.
171. **Anton Ruzanov.** Computational investigation of the electrical double layer at metal–aqueous solution and metal–ionic liquid interfaces. Tartu, 2018, 129 p.
172. **Katrin Kestav.** Crystal Structure-Guided Development of Bisubstrate-Analogue Inhibitors of Mitotic Protein Kinase Haspin. Tartu, 2018, 166 p.
173. **Mihkel Ilisson.** Synthesis of novel heterocyclic hydrazine derivatives and their conjugates. Tartu, 2018, 101 p.
174. **Anni Allikalt.** Development of assay systems for studying ligand binding to dopamine receptors. Tartu, 2018, 160 p.
175. **Ove Oll.** Electrical double layer structure and energy storage characteristics of ionic liquid based capacitors. Tartu, 2018, 187 p.
176. **Rasmus Palm.** Carbon materials for energy storage applications. Tartu, 2018, 114 p.
177. **Jörgen Metsik.** Preparation and stability of poly(3,4-ethylenedioxythiophene) thin films for transparent electrode applications. Tartu, 2018, 111 p.
178. **Sofja Tšepelevitš.** Experimental studies and modeling of solute-solvent interactions. Tartu, 2018, 109 p.
179. **Märt Lõkov.** Basicity of some nitrogen, phosphorus and carbon bases in acetonitrile. Tartu, 2018, 104 p.
180. **Anton Mastitski**. Preparation of α-aza-amino acid precursors and related compounds by novel methods of reductive one-pot alkylation and direct alkylation. Tartu, 2018, 155 p.
181. **Jürgen Vahter**. Development of bisubstrate inhibitors for protein kinase CK2. Tartu, 2019, 186 p.

182. **Piia Liigand.** Expanding and improving methodology and applications of ionization efficiency measurements. Tartu, 2019, 189 p.
183. **Sigrid Selberg.** Synthesis and properties of lipophilic phosphazene-based indicator molecules. Tartu, 2019, 74 p.
184. **Jaanus Liigand.** Standard substance free quantification for LC/ESI/MS analysis based on the predicted ionization efficiencies. Tartu, 2019, 254 p.
185. **Marek Mooste.** Surface and electrochemical characterisation of aryl film and nanocomposite material modified carbon and metal-based electrodes. Tartu, 2019, 304 p.
186. **Mare Oja.** Experimental investigation and modelling of pH profiles for effective membrane permeability of drug substances. Tartu, 2019, 306 p.
187. **Sajid Hussain.** Electrochemical reduction of oxygen on supported Pt catalysts. Tartu, 2019, 220 p.